SYNTHESIS AND CHARACTERIZATION OF COMPLEX PEROVSKITE SOLID SOLUTIONS

by

Hamel Tailor
B. Sc., Simon Fraser University, 2004

THESIS SUBMITTED IN PARTIAL FULFILLMENT OF
THE REQUIREMENTS FOR THE DEGREE OF

DOCTOR OF PHILOSOPHY

In the Department
of
Chemistry

SIMON FRASER UNIVERSITY

Spring 2010

APPROVAL

Name: **Hamel Tailor**

Degree: **Doctor of Philosophy**

Title of Thesis: **Synthesis and Characterization of Complex Perovskite Solid Solutions**

Examining Committee:

Chair: _____

David Vocadlo (Assistant Professor)

_____

Zuo-Guang Ye (Professor)
Senior Supervisor

_____

Byron Gates (Assistant Professor)
Committee Member

_____

Daniel Leznoff (Professor)
Committee Member

_____

Gary Leach (Associate Professor)
Internal Examiner

_____

Guozhong Cao (Professor)
External Examiner

Department of Materials Science and Engineering

University of Washington

Date Defended/Approved: _____April 12, 2010_____

Declaration of
Partial Copyright Licence

ABSTRACT

Materials based on the solid solution of (1-*x*)$Pb(Mg_{1/3}Nb_{2/3})O_3$-*x*$PbTiO_3$ ((1-*x*)PMN-*x*PT) show some of the best piezoelectric and ferroelectric properties. Although the ferro-/piezoelectric properties are very good, there are drawbacks to this system such as difficulty in preparing pure phase ceramics and low operating temperature range resulting from the low Curie temperatures (< 130 °C) exhibited by the compositions that show the best piezoelectric properties (*x* = 0.28-0.35).

The (1-x)PMN-xPT ceramics with *x* = 0.28 - 0.32 were prepared in pure phase using a novel chemical solution method. The ceramics display better piezoelectric properties compared to those prepared by conventional solid state method. To optimize the ceramic properties, the effect of high temperature poling was investigated, and it was found that poling at high temperature degrades the piezoelectric properties due to a electric field induced phase transition.

The same solution method was used to fabricate ceramics of (1-x)PMN-xPT with *x* = 0.07 and 0.10 which exhibit their maximum of permittivity near room temperature. A sintering temperature of 1100 °C/4hrs was required in order to obtain high density, reduce dielectric losses and increase the dielectric permittivity in order to optimize capacitive performance.

The solid solution between $Pb(Mg_{1/3}Nb_{2/3})O_3$ (PMN) and $Bi(Zn_{1/2}Ti_{1/2})O_3$ (BZT) was investigated for its structure and dielectric behaviour. The addition of BZT to PMN does not change the structure significantly and it remains cubic to the solubility limit of 0.725PMN-0.275BZT. The dielectric properties exhibit an increase in frequency and temperature dispersion with increasing BZT content, indicating an increase in relaxor behaviour.

The $Pb(Mg_{1/3}Nb_{2/3})O_3$-$PbTiO_3$ -$Bi(Zn_{1/2}Ti_{1/2})O_3$ solid solution has been prepared in order to explore its structure, dielectric, ferroelectric and piezoelectric properties as a function of composition for use in high T_C piezoelectric applications. The structure and properties were mapped as a function of composition to establish the ternary phase diagrams of this system for its structure, dielectric and piezo-/ferroelectric properties.

This thesis is dedicated to my parents, Anila and Navin Tailor,

for giving me the inspiration, love and strength to pursue my goals and dreams.

.

ACKNOWLEDGEMENTS

It is an honour for me to thank my senior supervisor, Dr. Zuo-Guang Ye. His encouragement, guidance and support from the initial to final stages of my graduate studies has helped me to develop the skills and perseverance to not only to take on the problems that come about in the lab, but to take on the many challenges in life that will come my way.

I would like to thank my supervisory committee members, Dr. Daniel Leznoff and Dr. Byron Gates, for their valuable suggestions and advice during the course of this work.

I extend my thanks to Dr. Guozhong Cao and Dr. Gary Leach for agreeing to be the external and internal examiners of this thesis.

I would like to express my gratitude to the members of Dr. Ye's research group, both past and present. In particular, it is my pleasure to thank Ms. Amanda Gronotte for her friendship and help in editing this thesis. I would like to thank Mr. Michael Leung for his contributing work which was used in completing the ternary phase diagrams presented in Chapter 6. I am also grateful to Dr. Keshwaree Babooram-Narain, Dr. Xifa Long, Dr. Yong Hong Bing, Dr. Chao Lei, Dr. Weimin Zhu, Dr. Haiyan Guo and Dr. Alexei Bokov for their guidance and mentorship during my studies. I would like to thank Mr. Allen Wei, Ms. Yujuan Xie, Ms. Ling Chen, Ms. Jenny Wong, Ms. Reagan Belan and the late Mr. Huichun Yu for their comradery, company and valuable friendship which made my time in the lab so enjoyable.

I would like to thank the members of the Chemistry Department at Simon Fraser University for their support.

The financial supports from Simon Fraser University, the Chemistry Department, the Natural Sciences and Engineering Research Council of Canada, and the U. S. Office of Naval Research are greatly appreciated.

Finally, I owe my deepest gratefulness to my sister, Meera Tailor and my loving family, your patience, understanding, and unconditional love has given me the strength to make this accomplishment possible.

TABLE OF CONTENTS

LIST OF FIGURES

LIST OF TABLES

LIST OF ABBREVIATIONS

AFE	antiferroelectric
β	Karlausch Williams Watts shape parameter
BT	$BaTiO_3$
BZT	$Bi(Zn_{1/2}Ti_{1/2})O_3$
CR	conventional relaxor
d_{33}	piezoelectric coefficient
E_a	activation energy
E_C	coercive field
EG	Ethylene glycol
ε'	real part of permittivity
ε''	imaginary part of permittivity
ε'_{max}	maximum dielectric constant
ε'_{RT}	room temperature dielectric constant
FE	ferroelectric
f_a	antiresonance frequency
f_r	resonance frequency
k_P	planar electromechanical coupling factor
KWW	Karlausch Williams Watts
MPB	morphotropic phase boundary
Me	Metal
P_r	remnant polarization
PNR	polar nanoregion
P_s	spontaneous polarization
PMN-PT	$Pb(Mg_{1/3}Nb_{2/3})O_3$-$PbTiO_3$
PMN-PT-BZT	$Pb(Mg_{1/3}Nb_{2/3})O_3$-$PbTiO_3$ -$Bi(Zn_{1/2}Ti_{1/2})O_3$
PZN-PT	$Pb(Zn_{1/3}Nb_{2/3})O_3$-$PbTiO_3$
PT	$PbTiO_3$

PZT	$Pb(Zr,Ti)O_3$
R	rhombohedral
T	tetragonal
τ	relaxation time
$tan\delta$	dielectric loss
T_C	Curie temperature
T_f	Vogel-Fulcher Freezing Temperature
TGA/DTA	Thermogravimetric Analysis/Differential Thermal Analysis
T_{max}	maximum permittivity temperature
T_{MPB}	Morphotropic phase transition temperature
XRD	X-ray diffraction
UR	universal Relaxor

CHAPTER 1:

General Introduction

This thesis work describes the development of new materials and fabrication techniques of complex perovskite ceramics with high performance and high Curie temperatures for a wide range of applications, such as high density capacitors, electromechanical transducers, sensors and actuators.

This chapter will present the necessary concepts and background information, which lay out the foundation of this work. It includes discussion on the perovskite structure, piezoelectricity, ferroelectricity, relaxor ferroelectricity, time dependent dielectric response and a brief overview of the current status and developments in materials based on complex perovskites, leading to the motivation and objectives of our work.

1.1 Perovskite Structure

Materials of the perovskite structure posseses an ABO_3 formula unit where the A-site is occupied by a large 12 coordinate cation and the B-ion is occupied by a small, octahedrally coordinated cation. Figure 1.1 shows the perovskite structure which consists of a primitive cubic unit cell of *A* cations with oxygen anions sitting at each of the 6 face centres. The 6 oxide anions create an octahedral site in which the *B* cation is coordinated.

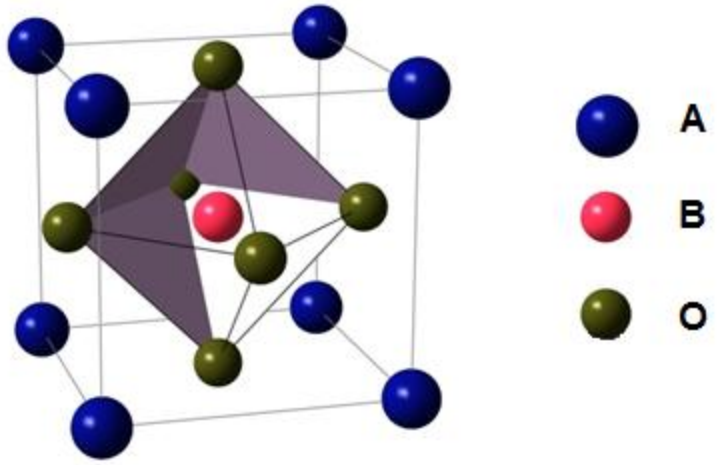

Figure 1.1: Cubic prototype perovskite ABO_3 unit cell The *A*-cations on the cube corners, the oxygen ions on the face centres and the *B*-cation at the centre of the octahedral site.

To maintain stoichiometry and charge balance, the combination of cations must satisfy the condition that the sum of the valence of all the *A* and *B* cations equal +6 in order to balance the negative charge of the 3 O^{2-} oxide anions in the formula unit. This allows for the formation of complex perovskites where two or more ions occupy crystallographically equivalent sites.

The perovskite structure has received much attention in the field of physics and materials science because a large number of materials based on this and related structures show interesting functional properties for technological applications [1-7]. The wide range of properties coupled with the flexibility of the perovskite structure to accommodate a wide range of cation combinations provides an excellent frame for developing new material systems and investigating the relationship between the crystal chemistry and physical properties.

1.2 Ferroelectricity

A ferroelectric material is one that exhibits a spontaneous electric polarization (P_s), over some range of temperature, that can be reoriented with the application of an appropriate external electric field [1]. Ferroelectric materials are characterized by a hysteresis loop (Fig. 1.2), which displays the variation of polarization (P) as a function of applied electric field (E) [8].

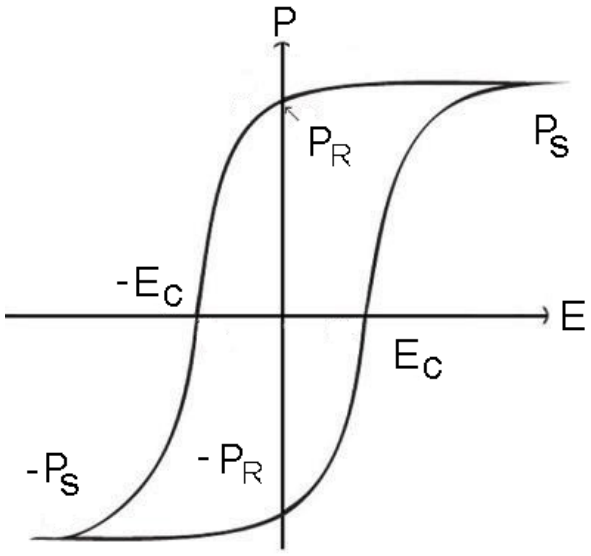

Figure 1.2: A typical Polarization-Electric Field (*P*-*E*) hysteresis loop produced by ferroelectric materials, showing the remnant polarization P_R, coercive field E_C and saturation polarization, P_S.

The occurrence of ferroelectricity in perovskites depends on bond type and polarizability between the ions, however, the formation of the structure is most sensitive to the size and valence of the *A* and *B* cations and is generally described with respect to ionic radii. The tolerance factor (t) is used to predict the formation of the perovskite structure [9, 10]:

$$t = \frac{r_A + r_O}{\sqrt{2}(r_B + r_O)} \quad , \tag{1.7}$$

where r_A, r_B, and r_O are the ionic radii of the *A*, *B*, and oxygen ions, respectively. It has been determined that the form of the perovskite structure falls between t = 0.88 and t =1.09 with the A cation having a coordination number of 12, and B cation a coordination number of 6 [11, 12].

In perovskites, the transition from the cubic (point group m3m) non-polar paraelectric phase (Fig 1.3 (a)) to the ferroelectric phase is associated with a structural phase transition to a lower symmetry (e.g. tetragonal phase, point group 4mm, Fig 1.3 (b)). The change in structure enlarges the size of the octahedra which causes the *B*-site cation to become displaced off centre with respect to oxygen anions. The off centre balance of charges creates a dipole moment within the unit cell, leading to the spontaneous polarization.

The high temperature non-polar cubic phase is characterized by a single well potential in the free energy versus polarization curve, with the minimum at P = 0 (Fig 1.4 (c)). Because of the enlargement of the oxygen octahedron in the low symmetry ferroelectric phase, there is a local free energy maximum for the *B*-site cation to sit at the octahedron centre, creating a double well potential for two stable polarization states [13].

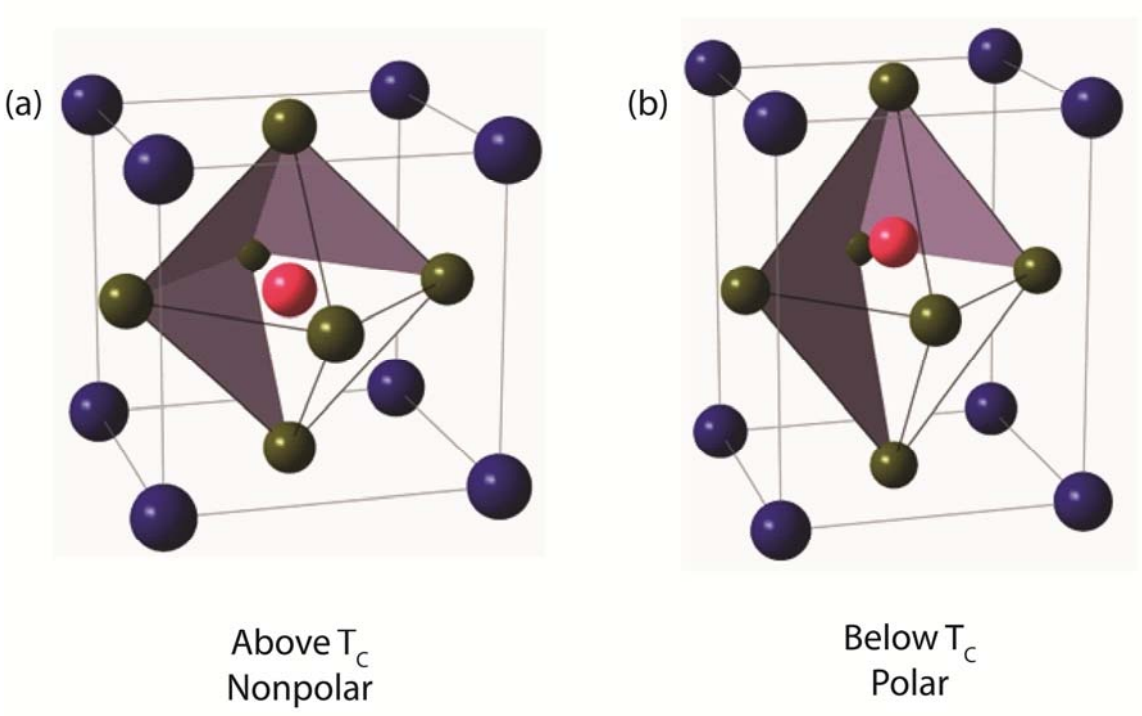

Figure 1.3: (a) Non-polar cubic prototype perovskite ABO_3 crystal structure above T_C. (b) A tetragonally distorted perovskite unit cell showing the off-centre displacement of the B-site cation creating a spontaneous polarization (P_S) in the material which can be switched by an electric field of opposite polarity.

At the phase transition between the non polar cubic phase of single well potential and the polar ferroelectric phase of double well potential, the potential curve becomes flattened (Fig 1.4(b)), causing anomalies in the temperature dependences of the dielectric, elastic, thermal, and optical properties around the phase transition temperature. A prototypical example is the divergence of the real part of the dielectric permittivity (ε') observed near the T_C (Fig. 1.4(d)), resulting from an extremely polarizable state due to a flattened free energy potential curve. This sharp increase in permittivity upon cooling is indicative of a paraelectric to ferroelectric phase transition. It follows the Curie-Weiss Law [14]:

$$\varepsilon' = \frac{C}{(T - T_{CW})} \quad , \tag{1.3}$$

where ε' is the real part of permittivity, C is the Curie constant, and T_{CW} is the Curie-Weiss temperature .

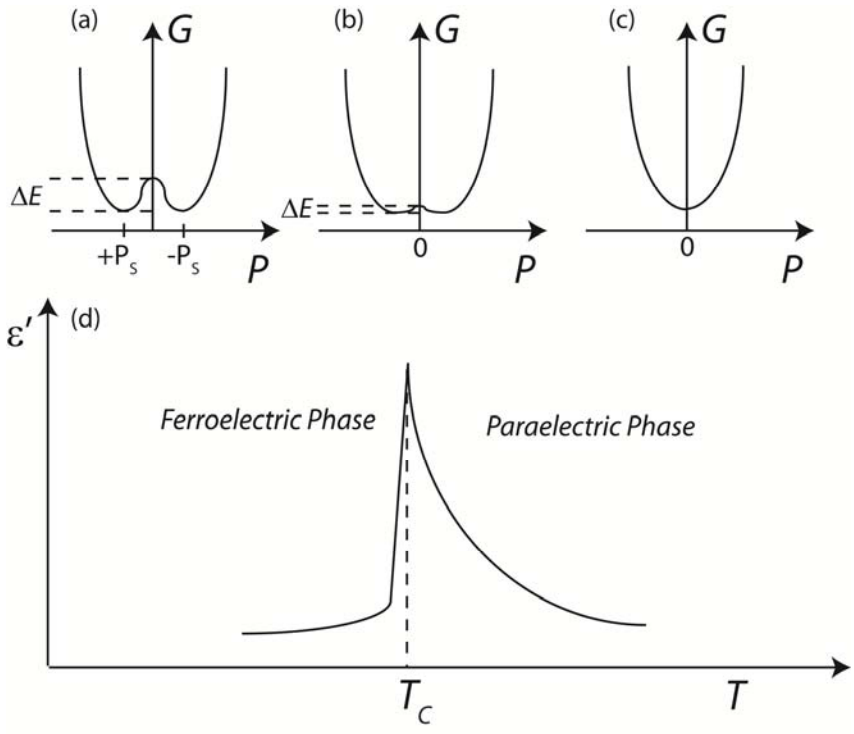

Figure 1.4: Two dimensional representation of the free energy versus polarization curve for a ferroelectric material (a) below T_C, (b) at T_C and (c) above T_C. (d) The resulting anomaly in permittivity at T_C. The two minima in the ferroelectric phase (a) represent the two possible polarization states, $+P_S$ and $-P_S$ Adapted from Ref [13].

When a ferroelectric material is cooled below its T_C, the polarization is not uniformly aligned throughout the entire crystal. Instead, areas of uniform polarization called ferroelectric domains form so that the macroscopic polarization of the crystal is zero. The formation of domains occurs in order to minimize the electrostatic energy of

depolarizing fields and to reduce the elastic energy formed by the mechanical constraints the material is confined to as it is cooled through the paraelectric to ferroelectric transition [14].

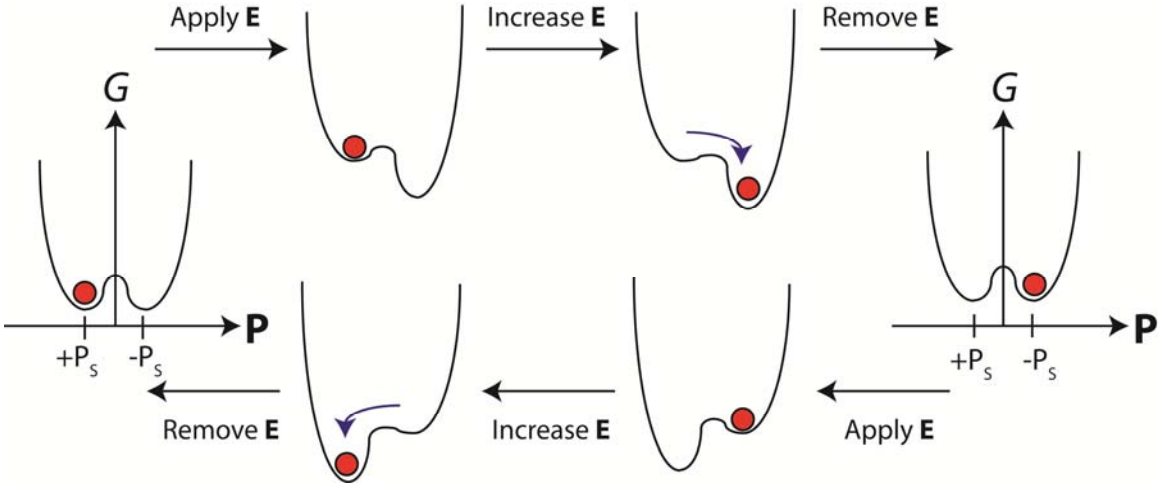

Figure 1.5: Two dimensional representation of the free energy versus polarization curve for a ferroelectric material undergoing polarization switching with the application of an electric field.

Figure 1.5 shows the free energy diagram for polarization switching in perovskite ferroelectrics with a double well potential. When an electric field is applied along the crystal, the domains where *P* is not in the same direction as the field will be in a higher energy state than those with *P* in the same direction as the electric field. As the electric field becomes increased to a value greater than the coercive field (E_C), all the domains will switch their polarization to align with that of the electric field in order to minimize energy. Upon increasing the electric field, the polarization will no longer increase, reaching the value of saturated polarization. When the field is removed, most of the domains will have their polarization remain in the same direction as the applied field, resulting in a remnant polarization, i.e. poled state. When the field is applied in the

opposite direction, the polarization will also switch in the opposite direction, giving rise to a the characteristic ferroelectric polarization versus electric field hysteresis loop, shown in Fig 1.2 The ability to pole single crystals and ceramics is a necessity for piezoelectricity (see Sec. 1.3) to manifest itself in single crystals and ceramics.

One of the best known perovskite ferroelectric materials is $PbTiO_3$ (PT) which has a T_C of 490 °C [15]. This material undergoes a paraelectric to ferroelectric phase transition from a cubic to tetragonal symmetry and is the most common end member in the solid solutions of the most widely studied and used ferroelectric materials such as $Pb(Zr_{1-x}Ti_x)O_3$ (PZT) and $(1-x)Pb(Mg_{1/3}Nb_{2/3})O_3$- $xPbTiO_3$ [7, 11, 16-18].

1.3 Piezoelectricity

Piezoelectricity was discovered by Pierre and Jacques Curie who found that certain materials such as quartz, tourmaline and zinc blende, possessed the ability to generate an electric potential in response to an applied mechanical stress [19]. The symmetry requirement for a material to exhibit piezoelectricity is the absence of an inversion centre in the unit cell of the structure. This implies that all ferroelectric materials are piezoelectric by virtue of their polar structure, which necessarily implies the absence of centro-symmetry in the crystal structure. Although the prefix "piezo" implies the application of pressure for the effect to occur, the property is also reversible giving rise to the converse piezoelectric effect [14]. In the converse effect, the application of an electrical potential across a piezoelectric material results in a mechanical strain in the material.

The direct and converse piezoelectric effects can be described by the following equations [14, 20]:

$$D_i = d_{ijk} X_{jk} \quad \text{(Direct effect)} \quad , \tag{1.1}$$

$$x_{ij} = d_{kij} E_k \quad \text{(Converse effect)} \quad , \tag{1.2}$$

where X_{ij} is the stress applied to a piezoelectric material, and D_i is the charge density developed on the surface of the material, E_k is the electric field applied in the k direction, and x_{ij} is the strain developed in the piezoelectric material, and d_{ijk} and d_{kij} are piezoelectric charge coefficients with units of pC/N and pm/V, respectively. Both d_{ijk} and d_{kij} are third-rank tensors, however, these piezoelectric coefficients for the direct and converse effects are thermodynamically identical.

Because the direct and converse piezoelectric coefficients are equivalent (d_{ijk} = d_{kij}), Equations 1.1 and 1.2 can be simplified and may be expressed in the reduced notation form [[21, 22]]:

$$D_i = d_{im} X_m \quad , \tag{1.3}$$

$$x_m = d_{mi} E_i \quad , \tag{1.4}$$

where values of i = 1, 2, or 3 and values of m = 1, 2, 3 are linear components and 4, 5, or 6 are shear components of the strain.

The electromechanical coupling factor, k, is used to measure the efficiency of a piezoelectric material in terms of electromechanical transduction. It expresses the

efficiency of a piezoelectric material to convert mechanical stress to electrical energy or vice versa, between electric potential and mechanical displacement:

$$k = \sqrt{(\text{generated mechanical energy/supplied electrical energy})} \quad (1.5)$$

$$k = \sqrt{(\text{generated electrical energy/supplied mechanical energy})} \quad (1.6)$$

A unity value of k would represent complete energy conversion with no energy dissipation as heat, which is most desired. Like the piezoelectric coefficient, the electromechanical coupling factor is dependent on the geometry and dimensions of the sample from which the property is measured, e.g. k_{33} or k_{31}, in which the subscripts refer to the polar direction and measurement direction, respectively. For ceramic disks, a special index, p is used since ceramics are typically thin circular disks with the polarization perpendicular to the plane of the ceramic. The planar coupling factor (k_p) is a measure of radial coupling between an electric field applied in the poled direction and the mechanical vibrations produced along the radial directions.

Figure 1.6 shows the mechanism by which polarization changes in a perovskite material exhibiting the piezoelectric effect. The compression or elongation of the unit cell creates a change in the polarization which in turn creates a difference in potential across the two surfaces.

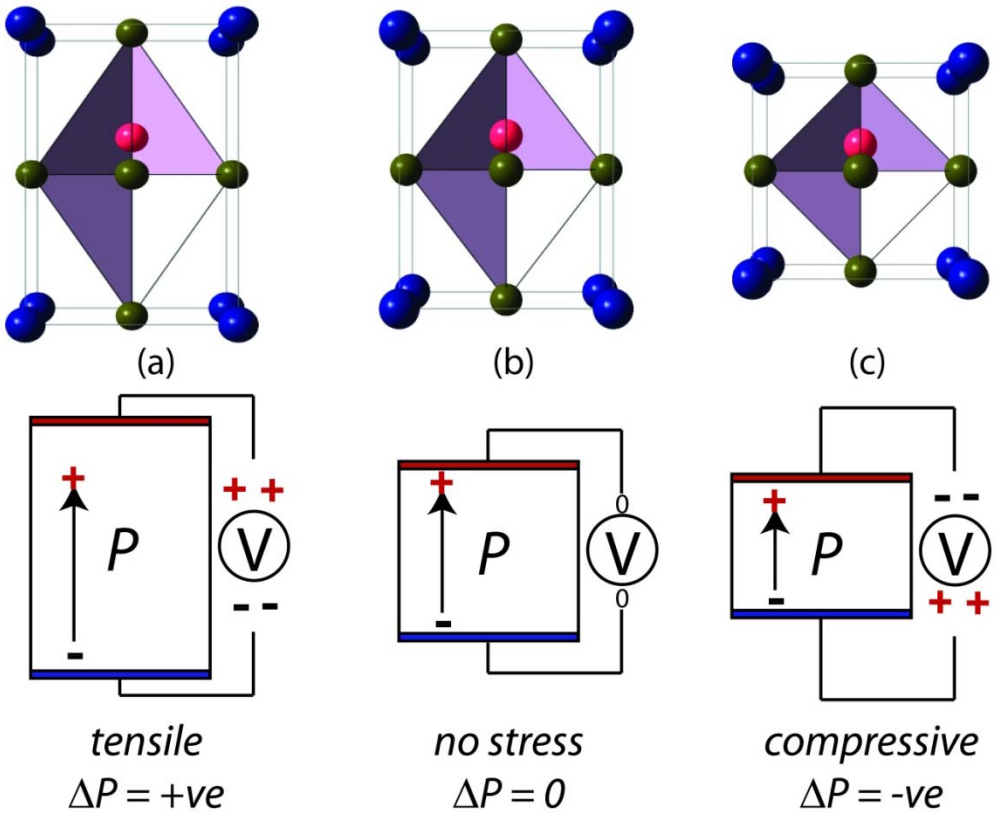

Figure 1.6: Mechanism of the piezoelectric effect. Top: ABO_3 perovskite structure in response to an external electric field or stress. Bottom: Magnitude of polarization (*P*) with response to an external electric field or stress. Centre: Room temperature structure and *P* under no external field or stress. Left: Elongated structure and increased *P* under external field of same polarity as *P*. Right: Compressed structure and decreased *P* under external field of opposite polarity as *P*.

Since the polarization is coupled to the strain in piezoelectrics, the change of ferroelectric polarization is accompanied by a change of strain in the sample. Whether the strain is compressive or tensile depends on the direction of the applied electric field in relation to the polarization. With the field applied anti-parallel to the polarization, the strain will be compressive until the coercive field is reached, at which point the polarization switches, causing the strain to changes from negative (compressive) to positive (tensile). From the bipolar curves it is possible to obtain the coercive field from

the point at which the strain changes from positive to negative with increasing field. This coercive field is the minimum field required for poling and it also limits the bipolar operating range in which a piezoelectric material can be used without switching the polarization.

The ability to switch polarization is very important in ferroelectric piezoelectrics because when a ferroelectric material is cooled below T_C, the random orientation of the domains is equally probable in any direction, thereby cancelling out the macroscopic polarization and creating a net centro-symmetric structure. This is especially important in polycrystalline piezoelectric ceramics in which the random grain orientations also add to the effect of cancelling out any induced charge that may develop in the material. Therefore, any random grain ceramic must be ferroelectric in order to be piezoelectric because only poled ceramics will possess the necessary symmetry requirements to show the piezoelectric property.

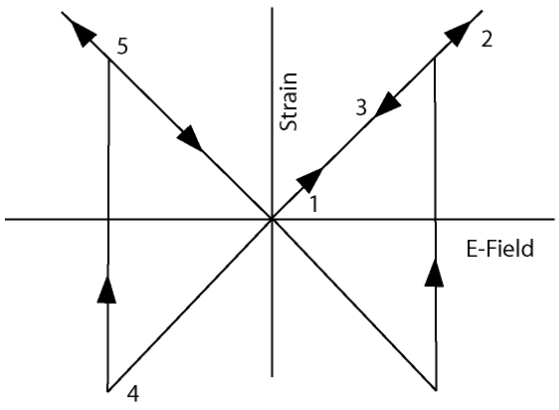

(1 to 2): Electric field is applied in the direction of polarization and the material strains with increasing field.
(2 to 3): Field decreases and strain follows the same line as 1 to 2.
(3 to 4): Field changes in sign and material begins to strain in opposite direction.
(4 to 5): Field switches polarization of domains so they are now aligned with the field causing the direction of strain to change sign

Figure 1.7: Mechanism of the bipolar piezoelectric effect in ferroelectrics as a result of domain switching.

1.4 Relaxor Ferroelectrics

Relaxor ferroelectrics, such as $Pb(Mg_{1/3}Nb_{2/3})O_3$ (PMN) have received much attention in the field of materials science and physics for their interesting nanostructural and dielectric properties (for several reviews see Refs. [23-25]). Three characteristics make relaxors different from normal ferroelectrics, such as $PbTiO_3$.

1. Relaxor materials exhibit a relatively broad maximum of permittivity compared to normal ferroelectrics which show a sharp peak in their ε' vs. T plots. (Fig 1.8). Furthermore, unlike normal ferroelectrics in which there is no frequency dependence of the T_C, the temperature of maximum permittivity (T_{max}) in relaxors is frequency dependent and increases with increasing measurement frequency.
2. In normal ferroelectrics the increase in permittivity arises from an increase in lattice polarization as it approaches the ferroelectric phase transition and associated change in symmetry. The high permittivity in relaxors arises from local polarizations and nano-sized domains which nucleate and grow below a certain temperature, called the Burns temperature (T_B) which is higher than that of T_{max}.
3. No macroscopic ferroelectric phase transition takes place upon cooling below the temperature of maximum of permittivity. No macroscopic polarization or birefringence develops spontaneously, however, it is possible to induce a macroscopic polar phase by applying an electric field at a temperature lower than the depolarization temperature (T_d), which is the highest temperature at which a macroscopically polar state can be induced with an electric field. The

induced macroscopic polarization vanishes upon heating with zero electric field at T_d.

The physical properties of relaxor materials are believed to be closely linked to the crystal chemistry and resulting nanostructure. Many lead-based relaxors are complex perovskites with the $Pb(B'_yB''_{1-y})O_3$ formula with the B' and B'' atoms disordered and distributed randomly along crystallographically equivalent octahedral sites [25, 26]. The earliest model to describe this behaviour was proposed by Smolenski et al. They proposed that the chemical inhomogeneity created from the disordered arrangement of the B' and B" sites creates different local T_C's and spreads out the phase transition over a range of temperatures, where T_{max} represents the mean Curie temperature [27, 27].

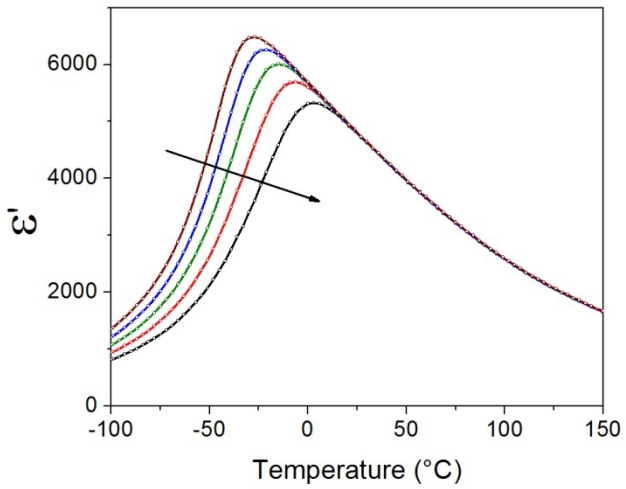

Figure 1.8: Real part of the permittivity, ε' as a function of frequency and temperature for a relaxor ferroelectric showing a broad and diffuse peak. The temperature of maximum ε' exhibits dispersion and increases with increasing frequency . The arrow indicates increasing measurement frequency.

A superparaelectric model for the relaxor ferroelectrics was proposed by Cross through an analogy with the superparamagnetic state [26]. This model suggests that at high temperature, micro polar regions are being dynamically disordered by thermal activation among different polarization states. The height of this activation energy barrier between domain states is directly proportional to the volume of the polar region. Upon cooling those regions with activation energy less than kT, (k being the Boltzmann constant), result in freezing into a preferential orientation which is related to the ferroelastic state to form a polar microdomain.

Vielhand and Cross extended the superparaelectric model to describe the dispersion of T_{max} in terms of the AC measurement frequency, (ω) by the Vogel-Fulcher (*VF*) relationship [28],

$$\omega = \omega_o \exp\left[\frac{-E_a}{T_{max}-T_f}\right], \tag{1.7}$$

where ω_o, E_a and T_f are the fitting parameters.

The Vogel-Fulcher relationship was known to be characteristic of structural and magnetic spin glasses, which show freezing in the mechanical properties and magnetic moments, respectively. The *VF* relationship might signify the same characteristic relaxation process for the characteristic relaxation time ($\tau = 1/\omega$) of the corresponding relaxation process:

$$\tau = \tau_o \exp\left[\frac{-E_\tau}{T-T_f}\right], \tag{1.8}$$

where τ_o, and E_b are the parameters and T_f is the freezing temperature at which the characteristic relaxation time becomes infinite [23, 29-31]. The divergence of τ implies the polarization dynamics slow down with decreasing temperature to the point that they no longer reorient and contribute to the polarization at any frequency. In dipole glasses, this freezing is due to the interactions between the dipoles when, at some temperature the forces between the dipoles becomes the thermal activation. This differs from the freezing of the dipole dynamics at 0 K temperature as dictated by Arrhenius law for independent dipoles.

The mechanism for the relaxor behaviour is proposed to originate from frustration between different interactions between unit cells. The direction of spontaneous displacement of a certain ion from a high symmetry position in ferroelectrics is dictated by the balance of elastic and dipole-dipole forces. These forces are subsequently determined by the composition of the unit cells surrounding the ion. For example, complex perovskites in which different cations are arranged in order on equivalent sites usually exhibit antiferroelectric (AFE) ordering, whereas in disordered perovskites no type of ordering is observed. The degree of ordering is related to the relative differences in valence, ionic radius and also by stoichiometry. For example, if there is a large difference in cationic radii, AFE ordering will be favoured in order to minimize elastic strain in the structure. However, in those complex perovskites where long range ordering is not observed, only ferroelectric or relaxor properties are displayed. The complex perovskite PMN exhibits typical relaxor properties. The mechanism by which relaxor behaviour appears is believed to originate from the heterogeneous distribution of Mg^{2+} and Nb^{5+} ions. The uneven distribution is due to the 2:1 stoichiometry between the two

different ions, which inhibits long range ferroelectric order. Instead of macroscopic domains, polar nano-sized regions (PNR) form in the regions rich in one type of ion. As the temperature is decreased the size and number of these PNRs rises, creating an increase in the permittivity as a function of temperature, $\varepsilon(T)$. As the temperature is further decreased, the dynamics of the PNRs begin to slow due to interactions between them so they cannot contribute to the permittivity, creating a local maximum in the permittivity at T_{max}.

The previous microscopic model was further extended by Bokov and Ye, who proposed a soft polar nanoregion model [32, 33]. This model used the same reasoning that the local direction of spontaneous displacement of an ion from a high symmetry position is determined by the composition of the unit cells surrounding the ion.

For example, extending the case of B' and B'' ions, an ion surrounded by its same type would favour ferroelectric ordering. Conversely, ions that have a majority of ions of the other type would favour antiferroelectric ordering. In a chemically disordered configuration areas rich in one type of ion would have interactions so strong that their individual polarizations become fixed so that they can only be reoriented with an external electric field. These cells are called "fixed" cells. However, in the case where there is an intermediate concentration of each type of neighbour, there will be frustration between ferroelectric and antiferroelectric ordering, and the cell will be free to fluctuate with thermal activation. The moments of these "free" cells can flip from one potential well to another, while the moments of the neighbouring cells remain unchanged. A planar representation of the compositional and dipole arrangement is shown in Figure 1.9.

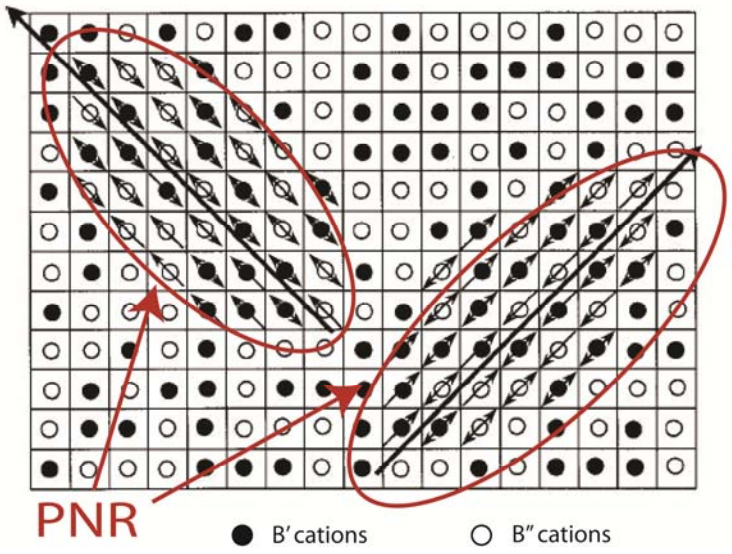

Figure 1.9: Schematic representation of the soft polar nanoregion model proposed by Bokov and Ye for compositionally disordered A(B'B")O_3 perovskites. For clarity, A and O ions are not shown. Small arrows indicate spontaneous moments of "fixed" cells, double sided arrows indicate the moments of "free" cells and large arrows indicate the polarization of the entire PNR (Adapted from Ref. [32]).

In this model the authors take into account the possibility of thermally activated reorientations within the PNR, which allow for direction as well as the magnitude of the polarization to change with time. This would imply two polarization mechanisms which are intimately linked: one is associated with the reorientation of the dipole moments of the PNR's, which is referred to as the conventional relaxor (CR) contribution, and the other of which is associated with the time dependent magnitude of polarization, called the universal relaxor (UR) contribution [34].

The permittivity in the temperature range above T_{max} for PMN and many other relaxors was successfully modeled by a single shape parameter, δ, using a quadratic law:

$$\frac{\varepsilon_A}{\varepsilon'} = 1 + \frac{(T - T_A)^2}{2\delta^2} \qquad (1.9)$$

where T_A ($< T_{max}$) is the parameter defining the temperature and position of the peak and ε_A is the extrapolated value of ε at $T = T_A$ [35]. The parameter δ can be considered as a convenient measure for describing the degree of diffuseness of the permittivity peak in relaxors. It was found that this law could be fitted to a large number of relaxors with varying degrees of diffuseness.

1.5 Solid Solutions and the Morphotropic Phase Boundary

A solid solution is the complete dissolution of one end member into the other to form a single phase allowing for continuous variability. In perovskites this is usually accomplished by substituting different cations into the *A* and *B* crystallographic sites.

An example would be the reaction to produce a solid solution between the two end members $A'B'O_3$ and $A''B''O_3$:

$$(1\text{-}x)A'B'O_3 + xA''B''O_3 \rightarrow (A'_{1-x}\, A_x\, '')(B_{1-x}'B''_x)O_3,$$

The solid solution compositions can be made by directly reacting the end members themselves or by reacting the constituent oxides in appropriate amounts in order to form the final composition desired. By this means, extensive variety of physical properties can be continuously changed by chemical substitution of the *A* and *B* cations. For example the substitution of Ti^{4+} for the $(Mg_{1/3}Nb_{2/3})^{4+}$ complex cation in PMN results in long range polar order, inducing a transition from relaxor to normal

ferroelectric state [36, 37]. In the case of *A* site substitution, the change of Pb^{2+} for Ba^{2+} results in $BaTiO_3$ with a 300°C increase in the ferroelectric phase transition temperature along with an increase in tetragonality in the structure. The increase in phase transition temperature is due to the existence of the stereochemically active $6s^2$ lone pair on the Pb^{2+} ion which enhances polarization and tetragonal distortion in the structure.

For many years, solid solutions based on the $(1-x)PbZrO_3$-$xPbTiO_3$ (PZT) system have been regarded as the best high performance piezoelectric perovskite materials and are the basis for almost all commercial transducer devices [7, 12, 19, 38, 39]. The characteristics that make this material so useful in a wide variety of applications are its relatively high T_C and large d_{33} (~500 pC/N) in modified PZT ceramics. One of the characteristics that make this system special is that the low temperature phase diagram is divided vertically into two regions of different symmetry, rhombohedral for the Zr-rich composition and tetragonal for the Ti-rich side, as shown in Figure 1.10 [40]. The term morphotropic phase boundary (MPB) was proposed by Jaffe et al. to describe the boundary between the two phases. The highest piezoelectric response (~ 350 pC/N) in this system was found near the boundary between these two phases ($x = 0.47$) [41].

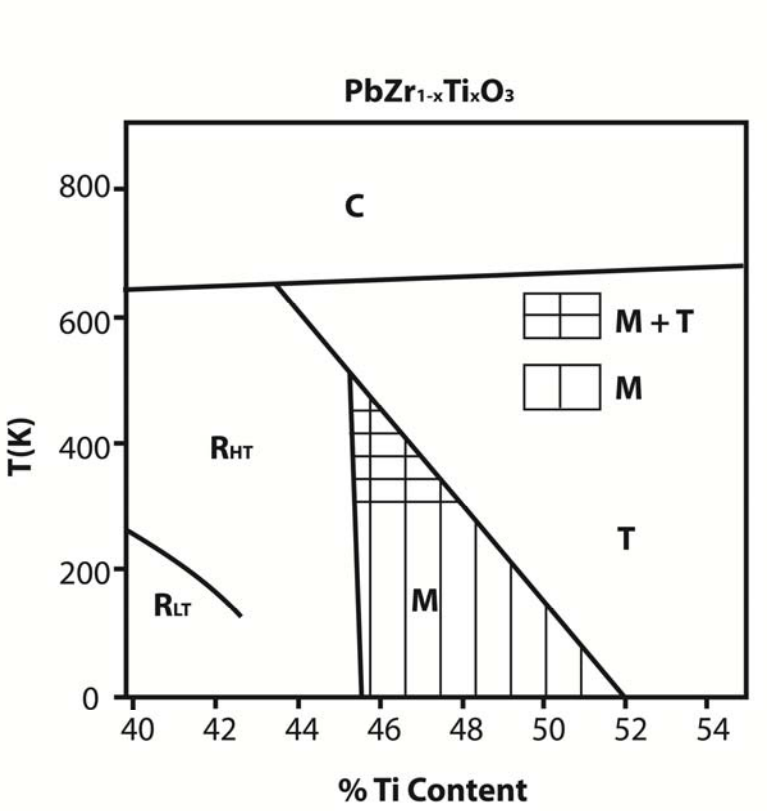

Figure 1.10: Temperature versus composition phase diagram of the (1-*x*)$PbZrO_3$-*x*$PbTiO_3$ solid solution system around the MPB. M denotes monoclinic phase, R, rhomohedral, and T for tetragonal (Adapted from Ref. [40]).

Later work showed that there was coexistence of two phases, as well as the presence of a new monoclinic phase, which bridges the R and T phases. It was then proposed that the excellent physical properties of PZT were associated with the MPB, in particular the coexistence of different phases, which would allow for more polarization states thereby facilitating more complete poling of ceramics [41]. Further studies on <001> textured PZT ceramics exhibited that ceramics with rhombohedral symmetry (*P* along <111>) showed a great enhancement in the piezoelectric response [42]. One would normally guess that the electric field or stress would have to be applied along the polar <111> direction to display the greatest piezoelectric response. The fact that the

experimental findings did not hold this to be true brought about new interest into understanding the crystallographic dependence of the piezoelectric properties. This would most easily be facilitated through single crystal studies, however, obtaining PZT crystals is very difficult due to difficulties in obtaining adequately large crystals with desired composition. However, other perovskite solid solution systems based on rhombohedral and tetragonal end members can be produced in the form of single crystals with adequate quality and compositions near their MPB's [39, 43-45]. Studies on single crystals of (1-*x*)$Pb(Zn_{1/3}Nb_{2/3})O_3$-*x*$PbTiO_3$ ((1-*x*)PZN-*x*PT) and (1-*x*)$Pb(Mg_{1/3}Nb_{2/3})O_3$-*x*$PbTiO_3$ ((1-*x*)PMN-PT) have shed more light on how the MPB affects the piezoelectric properties. The relationship between piezoelectric properties, crystal composition and orientation were studied in PZN-PT by Park and Shrout [7, 46]. Figure 1.11 presents the piezoelectric coefficient, (d_{33}) as a function of composition and crystal orientation. Although <111> is the polar direction for rhombohedral crystals, the maximum d_{33} value of 2500 pC/N is found in PZN-PT and PMN-PT crystals along the [001] direction. In fact, the d_{33} of <111> oriented PZN-PT single crystals was found to be 80 pC/N regardless of composition [7].

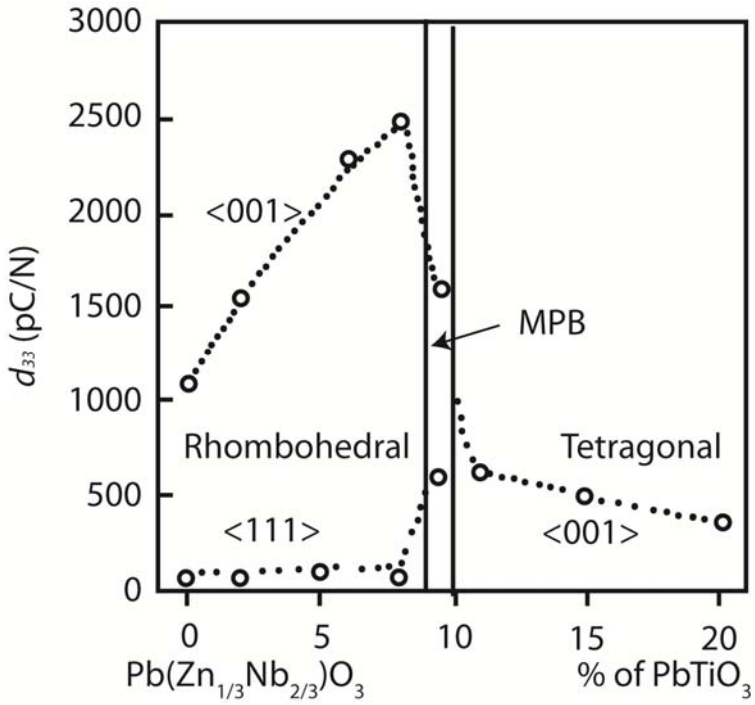

Figure 1.11: Piezoelectric coefficient, (d_{33}) as a function of composition and crystal orientation around the MPB of PZN-PT (Adapted from Ref. [39]).

The origin of the large piezoelectric properties for the PZN-PT and PMN-PT single crystals was due to an electric field induced transformation towards a tetragonal phase [7]. It was proposed that the high piezoelectric response near the MPB in single crystals occurred via a rotation of the polarization vector from the <111> direction to the <001> direction. Theoretical calculations by first principles showed that the energy difference between rhombohedral and tetragonal phases in compositions near the morphotropic phase boundary have sufficiently close energies, so the transformation from R to T would be more energetically favourable than other pathways in order to facilitate the ultrahigh strain [6].

These results point out the significance of the MPB and related effects which are believed to be responsible for the excellent properties. The low potential energy barriers lead to large discontinuities in the dielectric, elastic, piezo-/ferroelectric properties near the MPB. This is analogous to the anomalies that occur upon cooling through the para-/ferroelectric phase transition and it points out the significance of having an MPB in order to maximize the materials properties [47].

1.6 The (1-x)$Pb(Mg_{1/3}Nb_{2/3})O_3$ - x$PbTiO_3$ Solid Solution System

Compositions of (1-*x*)PMN-*x*PT with $x < 0.20$ show typical relaxor behaviour in their dielectric properties with a broad and high maximum of dielectric constant, ε_{max}, as high as 30 000 near room temperature. To put this value into perspective, current multilayer ceramic capacitors are based on $BaTiO_3$, which has a room temperature dielectric constant of ~1000, and water, which is considered a highly polar molecule, has a dielectric constant ~70 at room temperature. In particular those compositions with *x* between 0.05 and 0.10 exhibit their maxima of permittivity near room temperature. Since the dielectric constant is a measure of how well a material stores charge as a capacitor, the extremely high value makes materials in this composition range excellent candidates for use in high charge density capacitors.

As mentioned above, some of the best piezoelectric properties are found for the PMN-PT system in the form of single crystals. Table 1.1 shows some of the properties of the leading piezoelectric materials.

Table 1.1: Electromechanical properties of leading ceramic and single crystal materials based on the perovskite structure (adapted from Ref. [39]). Type II refers to modified PZT for use in applications that require high electromechanical activity. Type III refers to modified PZT for use in applications that require low loss at high electric field driving conditions.

Material	PZT Type II Ceramics	PZT Type III Ceramics	PZN-0.045PT Crystals	PMN-0.33PT Crystals
Dielectric Constant (RT)	2050	100	5000	8000
Dielectric Loss	0.018	0.003	0.01	0.01
T_C (°C)	340	300	155	166
Electromechanical Coupling coefficient (k_{33})	0.73	0.64	0.92	0.94
Piezoelectric coefficient (d_{33}, pC/N)	400	225	2200	2200

Figure 1.12 shows the phase diagram for the PMN-PT system in the vicinity of the MPB. Although the PMN-PT solid solution exhibits some of the best piezoelectric performance, one of its biggest drawbacks is the low T_C and an even lower rhombohedral to tetragonal transition temperature (T_{RT}). This low value limits the operating temperature range due to thermal depoling. In order to prevent the piezoelectric materials from depoling, the practical operating range of piezoelectric materials is limited to 2/3 of the lowest phase transition temperature. High temperature stability of properties is necessary for applications, such as in high temperature actuators used in fuel injection systems and inkjet printing. In addition, the low depolarization temperature produces complications in device production, because once poled, the ferroelectric material cannot be heated above the T_C.

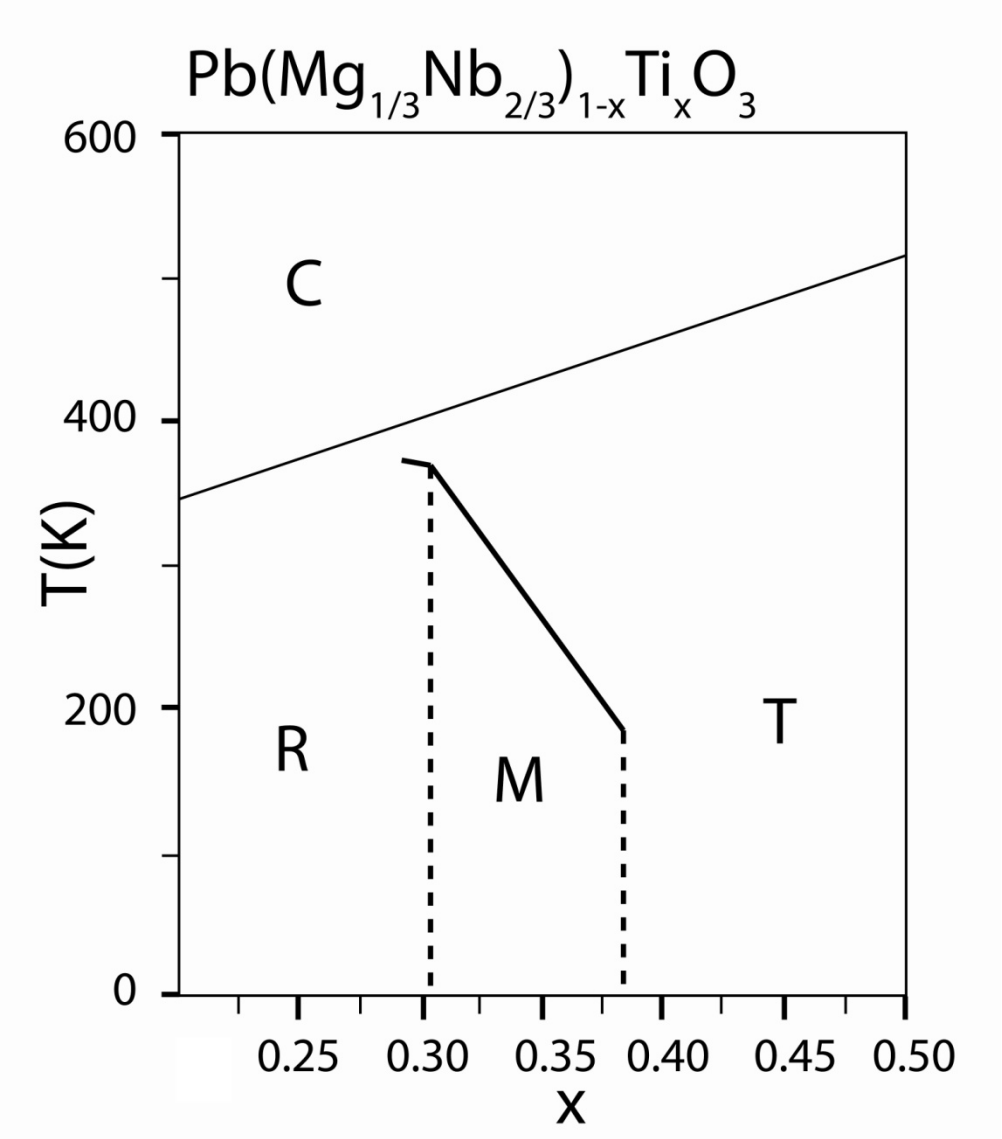

Figure 1.12: Temperature versus composition phase diagram of the (1-*x*)Pb($Mg_{1/3}Nb_{2/3}$)O_3-*x*$PbTiO_3$ solid solution system (adapted from Ref. [48]**). C stands for the cubic phase, R for the rhombohedral phase, T for the tetragonal and M for the monoclinic.**

Fabrication of single crystals is a very slow and expensive process due to long growth times and precious metal crucibles required for growth. Furthermore, single crystals of solid solutions such as PMN-PT generally suffer from composition segregation, which creates compositional gradients, resulting in inhomogeneous

properties across the crystal. As we have mentioned before, since the properties are so intimately linked to chemical composition, this is a severe drawback of the single crystals when used in electromechanical devices on a large scale. Even though polycrystalline materials provide an alternative to single crystals, ceramics of the PMN-PT system are difficult to produce in pure phase from conventional solid state reaction from the component oxides, due to the formation of an undesired $PbNb_2O_7$-type pyrochlore phase. Instead, a two-step method is required in which a *B*-site precursor of $MgNb_2O_6$ of columbite type structure is synthesized in the first step, which is then mixed with the remaining oxides to form the perovskite PMN-PT powders which can then be sintered into ceramics [49]. Therefore, it is necessary to develop new soft chemical process for the synthesis of PMN-PT ceramics, which may potentially exhibit improved dielectric and piezoelectric performance.

Recently Bokov and Ye reported a field induced shift of the morphotropic phase boundary in PMN-PT single crystals [50]. It was found that the piezoelectric properties and phase components were extremely sensitive to poling field, and "over-poling" the single crystals with too large a field was detrimental to the piezoelectric properties. However, the effects of poling on the PMN-PT ceramics have not been thoroughly investigated. Therefore, it is necessary to understand the compositional and temperature dependence of the poling conditions in order to optimized the piezoelectric response of the PMN-PT system in the range of compositions near the MPB.

1.6 $Bi(Zn_{1/2}Ti_{1/2})O_3$ and related Solid Solution Systems

$Bi(Zn_{1/2}Ti_{1/2})O_3$ (BZT), like many other $Bi(Me)O_3$ compounds, cannot be synthesized by the conventional solid state technique under ambient pressure due to the Bismuth ion being too small to form a stable perovskite structure. The first work on BZT as reported by Suchomel and Davies who partially stabilized the compound in a solid solution with lead titanate to form the $(1-x)Bi(Zn_{1/2}Ti_{1/2})O_3$-$xPbTiO_3$ (BZT-PT) system [51-53]. It was discovered that unlike many end members, BZT increased the phase transition temperature and the tetragonality (*c*/*a* ratio of lattice parameters) of the solid solution compared to PT itself. The only other end members to date causing the same behaviour are $BiFeO_3$, $Bi(Zn_{1/2}W_{1/2})O_3$ and $CdTiO_3$ [16, 53, 54]. It was proposed by Stein et al., that in the case of $Bi(M'M'')O_3$ compounds, it is necessary to have the B sites fully populated by highly charged and small, ferroelectrically active cations, such as Zn^{2+}, Ti^{4+}, Nb^{5+} and W^{6+} in order to allow for long range polar order. Later, Suchomel et. al reported the first synthesis of the pure BZT compound using high pressure (6 GPa) and its structure was investigated by means of X-ray diffraction [51]. It was found that the room temperature structure could be fitted with a P4mm unit cell, which is similar but more tetragonally distorted than PT. Based on these data, spontaneous polarization of 150 μC/cm² was predicted [51] which is similar to the value calculated by density functional theory (DFT) of 138 μC/cm, the latter being 57% larger than PT itself [55]. First principles calculations and investigations on other similar Bi^{3+} based solid solutions later revealed that the high degree of tetragonality is due to the $Bi^{3+}$and-B cation repulsive interactions [55]. The reports on the high T_C in the form of solid solutions reaching 700 °C and the high polarization of BZT and has sparked much interest in the

system for potential use in frequency multipliers as second harmonic generation materials and as high T_C ferroelectric materials for use in high temperature piezoelectric applications. However, no experimental measurements on the ferroelectricity or piezoelectricity on BZT related solid solutions have been reported to date.

1.7 Objectives of This Work and Organization of the Thesis

The recent push for new high performance piezoelectric materials to replace PMN-PT and PZT has opened up a large field for research in the area of solid-state ferroelectrics. In particular, much focus has been placed on developing new solid solutions to overcome the limitations of the PMN-PT and PZT systems. Although a great deal of investigation has progressed, focus must be kept on studying new material systems with better properties and performance to overcome the drawbacks of the currently used PMN-PT single crystals and ceramics in modern technologies. Therefore, the objective of this work is to: (i) develop new synthetic methods to improve the performance of the PMN-PT ceramics, (ii) to study the effect of high temperature poling and (iii) investigate new solid solution systems of PMN-BZT and its relaxor ferroelectric behaviour (iv) systematically study the new ternary PMN-PT-BZT ternary system to explore the structure and properties.

In this work, we strive to improve the properties of PMN-PT ceramics by two approaches. In the first approach, we develop a solution chemical method to produce high quality PMN-PT in order to improve the dielectric, piezoelectric and ferroelectric performance of the ceramics. In the second approach we investigate a new solid solution system by stabilizing BZT into the host PMN in order to investigate its effect on the

structure, dielectric properties and polar order of the host compound. We then extend this approach by creating yet another new solid solution system, PMN-PT-BZT and establishing the ferroelectric phase diagram, which maps out the phase symmetry, transition temperatures and limit of solubility for the perovskite phase. This thesis contains the following parts of original work:

1.7.1 Preparation of PMN-PT Ceramics Made Via a Solution Chemical Route and Characterization of their Properties.

As mentioned earlier in the above section, PMN-PT has been recognized as one of the highest performing piezo-/ferroelectric materials in the form of single crystals and ceramics. However, in order to produce high-quality and high-density ceramics a two step columbite method is usually required. This method requires preparation of a $MgNb_2O_6$ precursor phase, calcination (heating) of the reagent powders to form the solid solution powder, and finally sintering of cold pressed pellets at high temperature to produce the ceramics.

With a focus on developing a new synthetic methods for the preparation of piezoceramics, the first parts of our work (**Chapters 3 and 4**) involves the preparation of the ceramics of PMN-PT by a solution chemical method using ethylene glycol as the solvent. This soft chemical method is developed in order to produce a stable solution precursor that is pyrolyzed to form an inorganic precursor powder. From the mechanism of soft chemical reactions, it is expected that the higher degree of chemical mixing by using a solution route, combined with the high surface area will produce high density

ceramics in one sintering step without the need of initially calcining precursors or PMN-PT powders.

Chapter 3 describes the studies of the MPB compositions of (1-*x*)PMN-*x*PT ceramics with x = 0.28, 0.30 and 0.32. These compositions were chosen because they are situated just on the rhombohedral/monoclinic border of the MPB region, according to the PMN-PT phase diagram shown in Figure 1.12. Because of their proximity to the MPB, these compositions show the best piezoelectric properties in the form of single crystals and ceramics. It is my belief that by developing new solution chemical routes to produce high quality ceramics it is possible to further optimize the properties of these materials. In this chapter, the development of the solution chemical method is described which allows the fabrication of a stable precursor solution, pure perovskite phase and high density ceramics. The ferro/-piezoelectric properties and phase transitions are investigated by means of impedance spectroscopy, electric field versus strain measurements and charge versus force measurements and the effect of sintering temperature on the properties is also addressed. The effects of high-temperature poling were investigated so as to optimize the performance of these materials for potential transducer applications to reveal the over-poling effect in these compositions

Chapter 4 discusses PMN-PT ceramics, $x = 0.07, 0.10$ and investigates the effect of sintering temperature and stoichiometry on the formation of the perovskite phase as well as the density of the ceramics. The effect stoichiometry on phase purity was investigated by means of X-ray diffraction (XRD) measurements on sintered ceramics. The dielectric properties were investigated by means of impedance spectroscopy and variable temperature polarization versus electric field measurements.

1.7.2 Synthesis and Dielectric Characterization of a New Solid Solution System: PMN-BZT

Bismuth-based perovskite compounds have received much attention due to their ability to form extensive solid solutions with other lead based compounds [11, 16, 17, 56, 57]. In particular, much attention has been focused on solid solutions between end members of rhombohedral and tetragonal symmetry in order to facilitate the formation of morphotropic phase boundaries which may exhibit enhanced properties, as described in Section 1.5. Since BZT cannot be synthesized by conventional solid state reactions, a new solid solution between BZT and PMN was prepared in order to stabilize the BZT end member in the complex perovskite structure. The limit of solubility for the perovskite phase was studied and the relaxor ferroelectric properties investigated in detail. **Chapter 5** describes this part of the work on the synthesis and dielectric characterization of the PMN-BZT solid solution system. The structure was investigated by means of X-ray diffraction and the dielectric properties were investigated by broadband dielectric spectroscopy.

1.7.3 Structure and Properties Ferroelectric Phase Diagram of the ternary PMN-PT-BZT Solid Solution System

In order to address the shortcomings of the PMN-PT system and to develop new high temperature piezoelectric materials, chemical modification of the binary system is believed to be a viable solution. According to this approach and based on studies of the PMN-PT and BZT-PT binary systems our investigations naturally led to a new ternary

solid solution system via the addition of the highly polar BZT end member in the PMN-PT system. Since the solid solution of PT-BZT showed very high phase transition temperatures, the addition of BZT to PMN-PT is expected to address the issue of the relatively low ferroelectric phase transition temperatures of the PMN-PT system. The ceramics of the ternary system were prepared by solid state reactions. Several pseudo-binary lines were studied by means of XRD, dielectric spectroscopy, piezoelectric and ferroelectric measurements in order to systematically to investigate the phase stability and symmetry of the perovskite phase and the phase transition behaviour. All the data from the pseudo-binary lines are combined to establish a ternary phase diagram which illustrates the structure/symmetry of the phases, the physical properties, such as phase transition temperature, dielectric constant and piezoelectric coefficient as a function of composition. The establishment of the ternary phase diagrams has allowed the mapping of the structure and property relations to provide useful guidance to developing compositions of interest within this system which may be suitable for applications such as high temperature and high power electromechanical transducers.

References

[1] A. Asamitsu, Y. Moritomo, Y. Tomioka, T. Arima and Y. Tokura.. A structural phase-transition induced by an external magnetic-field. *Nature* vol 373, pp. 407-409 (1995).

[2] S. Cheong and M. Mostovoy. Multiferroics: A magnetic twist for ferroelectricity. *Nature Materials,* vol 6, pp. 13-20 (2007).

[3] Y. Moritomo, A. Asamitsu, H. Kuwahara and Y. Tokura.. Giant magnetoresistance of manganese oxides with a layered perovskite structure. *Nature,* vol 380, pp. 141-144 (1996).

[4] Y. Maeno, H. Hashimoto, K. Yoshida, S. Nishizaki, T. Fujita, J. G. Bednorz and F. Lichtenberg.. Superconductivity in a layered perovskite without copper. *Nature,* vol *372(6506),* pp. 532-534 (1994).

[5] Z-. G. Ye, "High Performance Single Crystals of Complex Perovskite Solid Solutions," *Materials Research Bulletin Society,* vol. 34, pp. 277-282, (2009).

[6] H. X. Fu and R. E. Cohen, "Polarization rotation mechanism for ultrahigh electromechanical response in single-crystal piezoelectrics," *Nature,* vol. 403, pp. 281-283, (2000).

[7] S. E. Park and T. R. Shrout, "Ultrahigh strain and piezoelectric behavior in relaxor based ferroelectric single crystals," *Journal of Applied Physics,* vol. 82, pp. 1804-1811, (1997).

[8] C. B. Sawyer and C. H. Tower.. Rochelle salt as a dielectric. *Physical Revie,* vol 35, pp. 0269-0273 (1930).

[9] H. J. Goldschmidt and J. R. Rait. Silicates of the perovskite type of structure. *Nature,* vol 152, pp. 356-356 (1943).

[10] R. D. Shannon. Revised effective ionic-radii and systematic studies of interatomic distances in halides and chalcogenides. *Acta Crystallographica,* pp. 751-767. (1976)

[11] R. E. Eitel, C. A. Randall, T. R. Shrout, P. W. Rehrig, W. Hackenberger and S. E. Park, "New high temperature morphotropic phase boundary piezoelectrics based on $Bi(Me)O_3$-$PbTiO_3$ ceramics," *Japanese Journal of Applied Physics,* vol. 40, pp. 5999-6002, (2001).

[12] Y. Xu, *Ferroelectric Materials and their Applications.* Amsterdam: North-Holland, (1991),

[13] R. Zeks. Blinc B, *Soft Modes in Ferroelectrics and Antiferroelectrics.* Amsterdam: North Holland, (1974),

[14] D. Damjanovic, Ferroelectric, dielectric and piezoelectric properties of ferroelectric thin films and ceramics. *Reports on Progress in Physics,*vol 61*,* pp. 1267-1324 (1998).

[15] R. E. Cohen, Origin of ferroelectricity in perovskite oxides. *Nature,* vol. *358,* pp. 136-138 (1992).

[16] C. J. Stringer, T. R. Shrout, C. A. Randall and I. M. Reaney, "Classification of transition temperature behavior in ferroelectric $PbTiO_3$-$Bi(Me'Me")O_3$ solid solutions," *Journal of Applied Physics,* vol. 99, (2006).

[17] I. Grinberg, M. R. Suchomel, P. K. Davies and A. M. Rappe, "Predicting morphotropic phase boundary locations and transition temperatures in Pb- and Bi-based perovskite solid solutions from crystal chemical data and first-principles calculations," *Journal of Applied Physics,* vol. 98, (2005).

[18] C. Lei, A. A. Bokov and Z-. G. Ye, "Ferroelectric to relaxor crossover and dielectric phase diagram in the $BaTiO_3$-$BaSnO_3$ system," *Journal of Applied Physics,* vol. 101, pp. 084105, (2007).

[19] G. H. Haertling, Ferroelectric ceramics: History and technology. *Journal of the American Ceramic Society* vol. *82(4),* pp. 797-818 (1999).

[20] M. E. Lines and A. M. Glass, *Feroelectric Materials and their Applications.* Oxford, U.K.: Clarendon Press, (1977),

[21] J. F. Nye, *Physical Properties of Crystals.* Oxford, UK: Oxford University Press, (1985).

[22] R. Tinder, *Tensor Properties of Solids : Phenomenological Development of the Tensor Properties of Crystals.* San Rafael: Morgan & Claypool Publishers, (2008)

[23] A. A. Bokov and Z-. G. Ye, "Recent progress in relaxor ferroelectrics with perovskite structure," *Journal of Materials Science,* vol. 41, pp. 31-52, (2006).

[24] G. A. Samara and E. L. Venturini, Ferroelectric/relaxor crossover in compositionally disordered perovskites. *Phase Transitions.* vol. 79*,* pp. 21-40 (2006).

[25] Z-. G. Ye, Relaxor ferroelectric complex perovskites: Structure, properties and phase transitions. *Key Eng Materials*, vol 155 pp. 81-82 (1998).

[26] L. E. Cross, Relaxor ferroelectrics. *Ferroelectrics* vol. 76, pp. 241-267 (1987).

[27] G. A. Smolensky, "Proc. 2nd Int. Meeting Ferroelectricity, Kyoto, 1969," *Journal of the Physical Society of Japan,* vol. 28, pp. 26 (1970).

[28] D. Viehland, S. J. Jang, L. E. Cross and M. Wuttig, "Freezing of the Polarization Fluctuations in Lead Magnesium Niobate Relaxors," *Journal of Applied Physics,* vol. 68, pp. 2916-2921, (1990).

[29] Z-. G. Ye and A. A. Bokov, "Dielectric and structural properties of relaxor ferroelectrics," *Ferroelectrics,* vol. 302, pp. 473-477, (2004).

[30] A. A. Bokov and Z-. G. Ye, "Low-frequency dielectric spectroscopy of the relaxor ferroelectric $Pb(Mg_{1/3}Nb_{2/3})O_3$-$xPbTiO_3$," *Physical Review B,* vol. 65, pp 144112: 1-10, (2002).

[31] A. A. Bokov and Z-. G. Ye, "Freezing of dipole dynamics in relaxor ferroelectric $Pb(Mg_{1/3}Nb_{2/3})O_3$-$xPbTiO_3$ as evidenced by dielectric spectroscopy," *Journal of Physics-Condensed Matter,* vol. 12, pp. L541-L548, (2000).

[32] A. A. Bokov and Z-. G. Ye, "Universal relaxor polarization in $Pb(Mg_{1/3}Nb_{2/3})O_3$ and related materials," *Physical Review B,* vol. 66, 064103: 1-9 (2002).

[33] A. A. Bokov and Z-. G. Ye, "Dielectric dispersion and critical behavior in relaxor ferroelectric $Pb(Mg_{1/3}Nb_{2/3})O_3$-$xPbTiO_3$," *Applied Physical Letters.,* vol. 77, pp. 1888-1890, (2000).

[34] A. A. Bokov and Z-.G Ye, Double freezing of dielectric response in relaxor $Pb(Mg_{1/3}Nb_{2/3})O_3$ crystals. *Physical Review B,* vol 74, pp. 132102: 1-9 (2006).

[35] A. A. Bokov, Y. H. Bing, W. Chen, Z-. G. Ye, S. A. Bogatina, I. P. Raevski, S. I. Raevskaya and E. V. Sahkar, "Empirical scaling of the dielectric permittivity peak in relaxor ferroelectrics," *Physical Review B,* vol. 68, pp. 0521020:1-4, (2003).

[36] Z-. G. Ye, Y. Bing, J. Gao, A. A. Bokov, P. Stephens, B. Noheda and G. Shirane, "Development of ferroelectric order in relaxor $Pb(Mg_{1/3}Nb_{2/3})O_3$-$xPbTiO_3$ ($0 <= x <= 0.15$)," *Physical Review B,* vol. 67, pp. 104104:1-8, (2003).

[37] O. Bidault, E. Husson and P. Gaucher, "Study of the electric field-induced low temperature phase in $Pb(Mg_{1/3}Nb_{2/3})O_3$: Titanium influence," *Journal of Physique III France,* vol. 7, pp. 1163-1172, (1997).

[38] B. Jaffe, W. R. Cook and H. Jaffe, *Piezoelectric Ceramics,*. London and New York: Academic Press, (1971).

[39] S. E. E. Park and W. Hackenberger, "High performance single crystal piezoelectrics: applications and issues," *Current Opinion in Solid State and Materials Science,* vol. 6, pp. 11-18,(2002).

[40] B. Noheda, J. A. Gonzalo, A. C. Caballero, C. Moure, D. E. Cox and G. Shirane, "New features of the morphotropic phase boundary in the $Pb(Zr_{1-x}Ti_x)O_3$ system" *Ferroelectrics* vol 237, pp. 541-548 (2000).

[41] R. Guo, L. E. Cross, S. E. Park, B. Noheda, D. E. Cox and G. Shirane, "Origin of the high piezoelectric response in $PbZr_{1-x}Ti_xO_3$". *Physical Review Letters,* vol. 84*,* pp. 5423-5426 (2000).

[42] X. H. Du, J. H. Zheng, U. Belegundu and K. Uchino. "Crystal orientation dependence of piezoelectric properties of lead zirconate titanate near the morphotropic phase boundary." *Applied Physics Letters,* vol. 72*,* pp. 2421-2423 (1998).

[43] M. Dong and Z-. G. Ye, "High-temperature solution growth and characterization of the piezo-/ferroelectric $(1-x)Pb(Mg_{1/3}Nb_{2/3})O_3$-$xPbTiO_3$ [PMNT] single crystals," *Journal of Crystal Growth,* vol. 209, pp. 81-90 (2000).

[44] D. Zekria and A. M. Glazer, "Automatic determination of the morphotropic phase boundary in lead magnesium niobate titanate $Pb(Mg_{1/3}Nb_{2/3})_{1-x}Ti_xO_3$ within a single crystal using birefringence imaging," *Journal of Applied Crystallography,* vol. 37, pp. 143-149 (2004).

[45] Y. H. Bing and Z-. G. Ye, "Effects of chemical compositions on the growth of relaxor ferroelectric $Pb(Sc_{1/2}Nb_{1/2})_{(1-x)}Ti_xO_3$ single crystals," *Journal of Crystal Growth,* vol. 250, pp. 118-125 (2003).

[46] B. Noheda, D. E. Cox, G. Shirane, S. E. Park, L. E. Cross and Z. Zhong, "Polarization rotation via a monoclinic phase in the piezoelectric 92% $PbZn_{1/3}Nb_{2/3}O_3$-8% $PbTiO_3$," *Physical Review Letters,* vol. 86, pp. 3891-3894 (2001).

[47] J. Kelly, M. Leonard, C. Tantigate and A. Safari, "Effect of composition on the electromechanical properties of $(1-x)Pb(Mg_{1/3}Nb_{2/3})O_3$-$xPbTiO_3$ ceramics," *Journal of the American Ceramic Society,* vol. 80, pp. 957-964 (1997).

[48] B. Noheda, D. E. Cox, G. Shirane, J. Gao and Z-. G. Ye, "Phase diagram of the ferroelectric relaxor $(1-x)Pb(Mg_{1/3}Nb_{2/3})O_3$-$xPbTiO_3$," *Physical Review B,* vol. 66, 054104:1-10 (2002).

[49] S. L. Swartz and T. R. Shrout, "Fabrication of Perovskite Lead Magnesium Niobate," *Materials Research Bulletin,* vol. 17, pp. 1245-1250 (1982).

[50] A. A. Bokov and Z-. G. Ye, "Field-induced shift of morphotropic phase boundary and effect of overpoling in (1-x)$Pb(Mg_{1/3}Nb_{2/3})O_3$-x$PbTiO_3$ piezocrystals," *Applied Physics Letters,* vol. 92, pp 082901:1-3 (2008).

[51] M. R. Suchomel, A. M. Fogg, M. Allix, H. J. Niu, J. B. Claridge and M. J. Rosseinsky, "Bi_2ZnTiO_6: A lead-free closed-shell polar perovskite with a calculated ionic polarization of 150 μC/cm²," *Chemistry of Materials,* vol. 18, pp. 4987-4989 (2006).

[52] M. R. Suchomel and P. K. Davies, "Enhanced tetragonality in (x)$PbTiO_3$ (1-x)$Bi(Zn_{1/2}Ti_{1/2})O_3$ and related solid solution systems," *Applied Physics Letters,* vol. 86, pp. 262905:1-4 (2005).

[53] D. M. Stein, M. R. Suchomel and P. K. Davies, "Enhanced tetragonality in (x)PbTiO3-(1-x)Bi(B'B")O_3 systems: $Bi(Zn_{3/4}W_{1/4})O_3$," *Applied Physics Letters,* vol. 89,pp 132907: 1-3 (2006).

[54] D. Y. Suarez-Sandoval and P. K. Davies, "Structure and phase stability of the $CdTiO_3$-$PbTiO_3$ system." *Applied Physics Letters,* vol. 82, pp. 3215-3217, (2003).

[55] I. Grinberg and A. M. Rappe., "First principles calculations, crystal chemistry and properties of ferroelectric perovskites" *Phase Transitions* vol.80, pp. 351-368 (2007).

[56] M. R. Suchomel and P. K. Davies, "Predicting the position of the morphotropic phase boundary in high temperature $PbTiO_3$-$Bi(Me)O_3$ based dielectric ceramics," *Journal of Applied Physics,* vol. 96, pp. 4405-4410 (2004).

[57] R. E. Eitel, C. A. Randall, T. R. Shrout and S. E. Park., "Preparation and characterization of high temperature perovskite ferroelectrics in the solid-solution (1-x)$BiScO_3$-x$PbTiO_3$." *Japanese Journal of Applied Physics,* vol. 41, pp. 2099-2104 (2002).

CHAPTER 2:
Materials Characterization: Principles and Techniques

2.1 Introduction

In this chapter, we present the basic principles for the various experimental techniques used to investigate the structure and properties of the materials studied in this work. These techniques include thermal and structural analyses, and characterization of physical properties of the materials by dielectric, piezoelectric and ferroelectric measurements.

2.2 Structural Characterization by Powder X-ray Diffraction (XRD)

Powder X-ray diffraction (XRD) is a technique that was used to characterize the phase components, structure, phase symmetry and lattice parameters of the materials prepared in this work. X-rays are generated by using a cathode ray tube in which electrons are accelerated towards a Cu target that will be the source of the X-ray radiation. When the cathode ray strikes the target, penetrating electrons eject other electrons out of core atomic orbitals, specifically from the inner most (*K*) shell. An electron from a higher energy (*L*) orbital relaxes to fill the lower energy orbital while emitting its excess energy in the form of an intense X-ray beam (Fig.2.1). Since the energies of the shells are well defined, each transition produces a monochromatic wavelength of radiation [1].

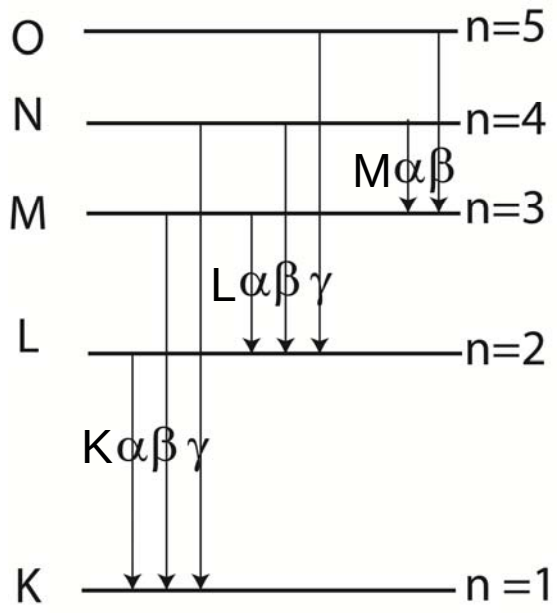

Figure 2.1: Electronic transitions which create characteristic X-ray.

Two instruments were used to collect X-ray diffraction patterns. A Rigaku Rapid-Axis X-ray diffractometer using Cu K_α (λ=1.5418 Å, 46 kV, 42 mA) radiation, utilizing a triple axis goniometer and an image plate detector. The image plate allows for 2 dimensional collection of diffraction data in real time and was useful in characterizing the phase purity of the ceramics prepared. The second instrument was a Bruker D8 Discover Diffractometer using Cu K_α (λ=1.5418 Å) wavelength X-rays (40 kV, 40 mA). This instrument uses Bragg Brentano Geometry with a scintillation detector for data collection and was used to collect diffraction data to be used to calculate lattice parameters of the compounds studied. Figure 2.2 illustrates how X-rays interact with the planes in the crystal lattice of the sample. This interaction can also be expressed by the Bragg law [2]:

$$2d_{hkl}\sin\theta = \lambda \quad , \tag{2.1}$$

where d_{hkl} is the interplanar spacing between the crystal planes (*hkl*), θ is the Bragg angle at which diffraction from these crystallographic planes are observed, and λ is the wavelength of the X-rays. The diffracted X-rays are detected and a plot of intensity as a function of the 2θ angle can be produced. This XRD pattern provides very useful information such as the *d*-spacing of the lattice planes, which is directly related to the unit cell parameters of the material, and the symmetry of the phase(s) present [2].

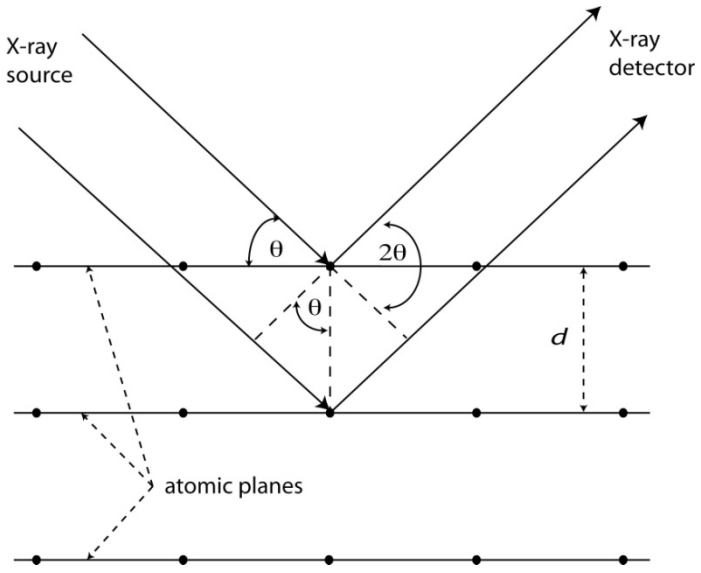

Figure 2.2: Bragg diffraction from a set of lattice planes with a spacing *d*.

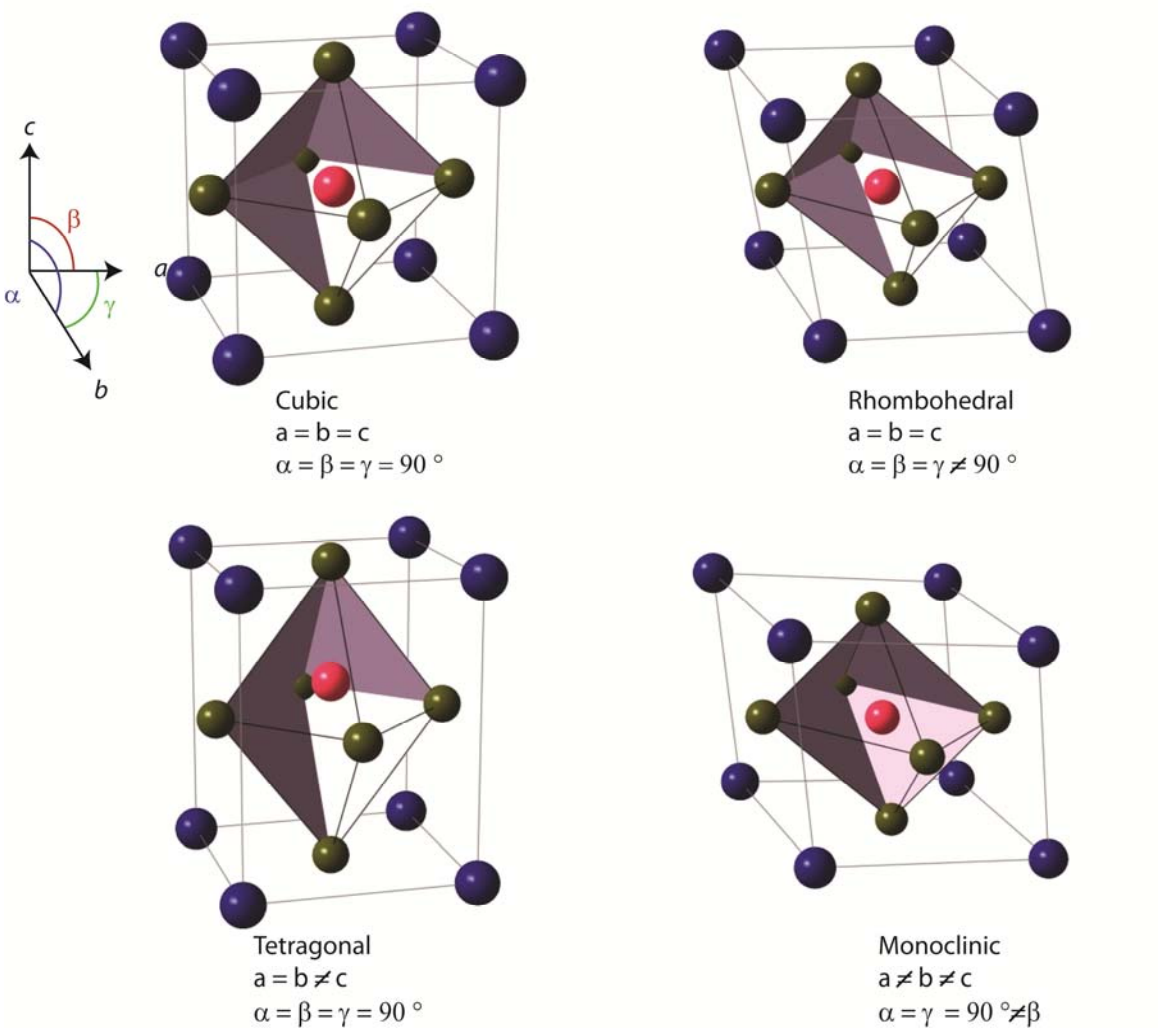

Figure 2.3: Illustration of various unit cell types with corresponding lattice parameters for a perovskite, ABO_3, structure.

A unit cell is characterized by three lattice parameters (*a, b, c)* which represent the lengths of the unit cell and three more parameters (α, β, and γ) which describe the angles between the axes (Fig. 2.3). Since lattice parameters are sensitive to phase symmetry as well as their composition, X-ray diffraction analysis is a powerful tool in characterizing phase, purity phase components and phase transitions as well as chemical composition of solid solutions (see below).

As a crystal undergoes a structural phase transition, the lattice parameters change along with *d*-spacings. Depending on the type of structure adopted by the material, the relationship between *d*-spacing and lattice parameters varies. The *d*-spacings for a material with a crystal structure of orthogonal axes, i.e. cubic, tetragonal or orthorhombic, can be expressed as follows[2]:

$$\frac{1}{d_{hkl}^2} = \frac{h^2}{a^2} + \frac{k^2}{b^2} + \frac{l^2}{c^2} \quad , \tag{2.2}$$

where *h*, *k*, and *l* are the Miller indices.

X-ray diffraction patterns can be used to monitor chemical reactions and structural properties such as phase purity and change of symmetry (phase transition). For example, if a crystal structure changes from cubic to tetragonal, the interaxial angles do not change ($\alpha = \beta = \gamma = 90°$), but the lengths of the unit cell are no longer equal ($a = b \neq c$). These will affect the *d*-spacings within the lattice, which in turn will result in the splitting or merging of peaks as shown in Figure 2.4. These characteristic XRD patterns can be used to identify the symmetry and phase components of the materials. Furthermore, in a solid solution the lattice parameters will contract or expand depending on the relative concentration of the end members present. Thus, lattice parameters provide a valuable piece of information for correctly verifying compositions of solid solutions, in the same way as phase transition temperatures do in composition versus temperature phase diagrams.

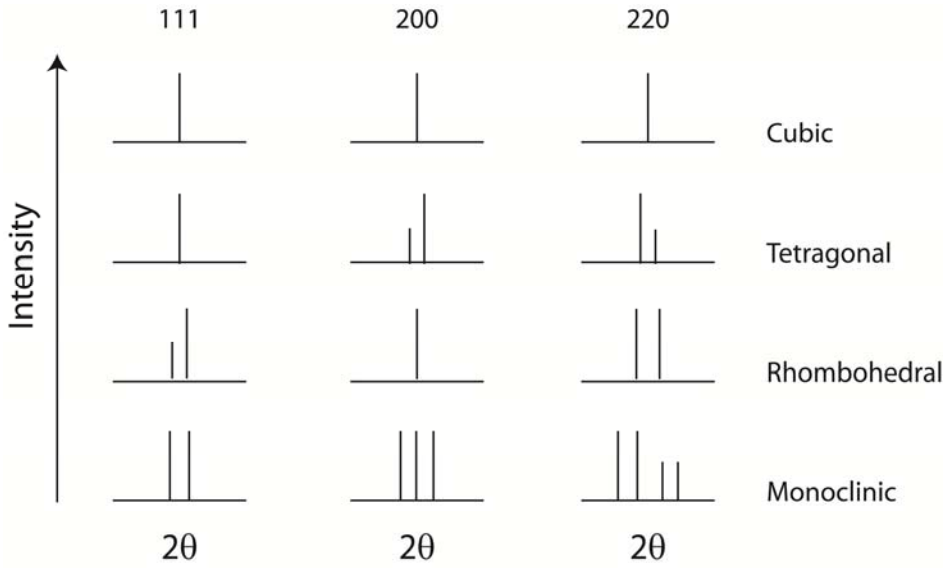

Figure 2.4: Characteristic X-ray diffraction patterns for various symmetries showing the corresponding splitting with respect to the cubic (111), (200) and (220) reflections.

2.3 Thermogravimetric / Differential Thermal Analyses

Thermogravimetric/differential analysis (TGA/DTA) is a characterization technique that is performed on samples to determine changes in weight in relation to change in temperature [9]. Such analysis relies on a high degree of precision in three measurements: weight, temperature, and temperature change. TGA/DTA is commonly employed in research and testing to determine characteristics of materials such as polymers, to determine degradation temperatures, absorbed moisture content of materials, the level of inorganic and organic components in materials, decomposition points of explosives, and solvent residues. TGA/DTA will be used in Chapter 3 in order to study the thermal decomposition of a solution precursor in order to study the phase formation of the powders made by this method.

TGA/DTA is carried out by raising the temperature of the sample and reference gradually and measuring weight and temperature difference between the sample and the reference [11]. Figure 2.5 shows a schematic diagram of a TGA/DTA instrument. The sample and reference pan are heated and the temperature difference is measured by a thermocouples which are embedded into the bottom of the two pan holders. To the sample pan is also attached a laser which shoots a light beam onto a photo-diode array. As the sample and reference are heated, changes in weight are recorded by measuring the relative deflection of the beam in relation to the diodes. Since TGA/DTA enables both the weight loss and the temperature difference to be recorded simultaneously, the nature of the thermal events associated with the weight loss can be obtained. For example, a large endothermic temperature change in the DTA accompanied by a large weight loss in the TGA graph would indicate an evaporation process, while a large weight loss accompanied by an exothermic peak would indicate combustion or decomposition instead.

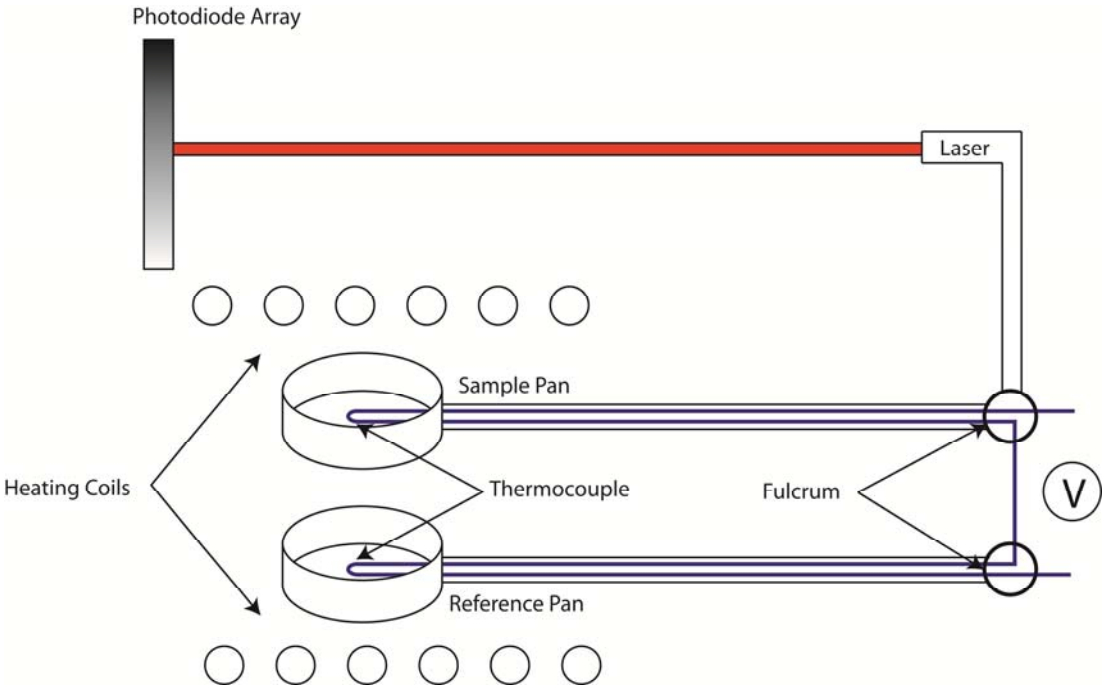

Figure 2.5: Schematic Illustration of TGA/DTA components. Weight changes in the sample are measured by monitoring the relative deflection of the laser beam on the photodiode. DTA temperature differences are measured by the thermocouples embedded into the bottom of the sample and reference pans.

2.4 Dielectric Spectroscopy

Dielectric characterization allows for the determination of the values of permittivity, and dielectric loss. Their variations as a function of temperature can reveal phase transition temperatures. Dielectric properties of the ceramics as a function of frequency and temperature were measured using two instruments depending on the temperature ranges being measured.

Two dielectric spectroscopy setups were used to collect dielectric property data in this thesis. For measurements taken between the range of -160 °C to 350 °C, the temperature dependence of the dielectric permittivity of the ceramics was measured at

various frequencies on a Novocontrol Alpha high resolution broadband dielectric analyzer. For high temperature measurements (20 °C to 700 °C) a computer controlled tube furnace was used to heat the samples and a Solartron 1260 impedance analyzer was used in conjunction with a Solartron 1296 dielectric interface to measure the frequency dependence of the dielectric properties at various temperatures.

The dielectric constant is a measure of the relative capacitance of a cell containing a dielectric compared to the same cell containing a vacuum. The empty cell charge displacement, (D) can be given by the following equation [3]:

$$D = \varepsilon_0 E \quad , \tag{2.2}$$

where E is the electric field and ε_o is the permittivity of free space, 8.854×10^{-12} F/m

If a dielectric material is placed in the same cell, an extra element of charge density will be created from the polarization (P) of the material, which will depend on the material's susceptibility (χ) to an electric field.

$$D = \varepsilon_0 E + P \quad , \tag{2.3}$$

$$D = \varepsilon_0 E + \chi E \quad , \tag{2.4}$$

The permittivity of free space and the material's susceptibility, (χ) can be combined into a single value called the permittivity of a material, ε, which describes the total charge density created in the presence of an external electric field.

$$D = \varepsilon E \quad , \tag{2.5}$$

The relative real permittivity, or dielectric constant (ε'), is determined based on the following equation:

$$C = \varepsilon' \varepsilon_o \left(\frac{A}{d} \right) \quad , \tag{2.6}$$

where C is the capacitance of the dielectric material between two parallel electrodes, ε_o is the permittivity of free space, A is the area of one of the plates of the parallel electrodes, and d is the distance between them. The dielectric constant is a measure of the ratio of charge density (D) generated across a capacitor cell containing a dielectric to that of the same empty cell.

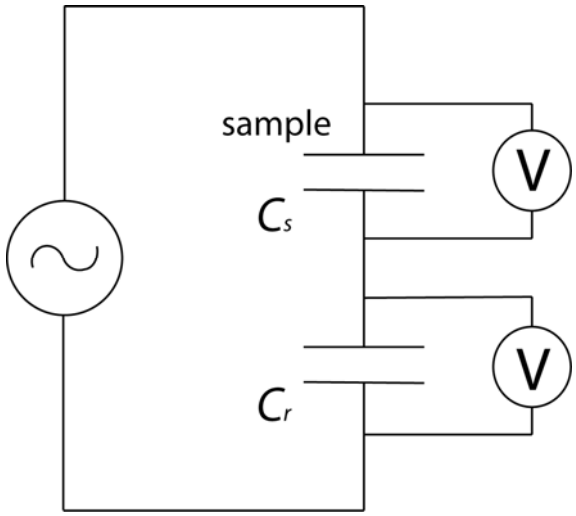

Figure 2.6: Schematic diagram of the circuit used in the dielectric permittivity measurements.

Figure 2.6 shows a schematic of the circuit used to measure dielectric properties. In this circuit, the voltage is applied by a signal generator across the pair of electrodes on the surfaces of a sample capacitor (C_s, with thickness d) and a reference capacitor (C_r). The voltage (V_r) across the reference capacitor is measured, and because the two capacitors are connected in series, the charge (Q_r) on the reference capacitor must be the same as the charge (Q_s) over the sample capacitor ($Q_r = Q_s$). This means that the charge on the sample can be found by:

$$Q = C_r \times V_r \quad , \tag{2.7}$$

The voltage (V_s) is also measured across the sample, allowing for the capacitance of this material to be determined by using the following equation:

$$C_s = \frac{Q}{V_s} \quad , \tag{2.8}$$

Once the capacitance of the sample (C_s) is obtained, the dielectric permittivity can be determined using Equation 2.3.

Equation 2.9 describes the charge density generated for a material with capacitance C_S in response to an AC voltage with frequency ω. Taking the derivative with respect to frequency will give us the frequency dependence of the current with respect to time.

$$Q = C_s V_o \sin(\omega t) \quad , \tag{2.9}$$

$$I = \omega C_s V_o \cos(\omega t) \quad , \tag{2.10}$$

$$I = \omega C_s V_o \sin(90 - \omega t) , \tag{2.11}$$

This shows that the current generated from an ideal capacitor will lead the voltage by a phase shift of 90°. However, in real material systems, the capacitive charge may not follow the voltage exactly due to the time required for polarization to take place and dielectric relaxation occurs. Dielectric relaxation is the frequency or time dependence of the dielectric properties being measured. This is usually caused by a delay in polarization with respect to an electric field. This happens in the case where the electric field is changing at a rate faster than the attempt time for the polarization to occur in a dielectric material. For example when the electric field frequency increases,

1. it becomes impossible for dipolar polarization to follow the electric field in the microwave region around 10^{10} Hz;

2. In the infrared or far-infrared region around 10^{13} Hz, ionic polarization loses its response to the electric field;
3. Electronic polarization loses its response in the ultraviolet region around 10^{15} Hz.
4. In the wavelength region below ultraviolet, permittivity approaches the constant ε_0 in every substance, where ε_0 is the permittivity of the free space. Because permittivity indicates the strength of the relation between an electric field and polarization, if a polarization process loses its response, permittivity decreases (Fig. 2.8)

The existence of dielectric loss, which may be caused by leakage current or relaxation, also needs to be considered when writing the expression for permittivity. Total current (I) with respect to frequency can be described as:

$$I(\omega) = i\omega D(\omega) + \sigma / \omega \quad , \tag{2.12}$$

where σ is the conductivity, and $i\omega D(\omega)$ is the contribution from capacitance. The capacitive current can be separated into two contributions, one that follows the applied voltage due to relaxation, and the other that is a purely capacitive contribution at 90° out of phase, or in quadrature:

$$I(\omega) = \{i\omega\varepsilon_0[1 + \chi'(\omega) - \chi'(\omega)]\}E \quad , \tag{2.13}$$

$$I(\omega) = \{\varepsilon_0\omega\chi''(\omega) + i\varepsilon_0\omega[1 + \chi'(\omega)]\}E \quad , \tag{2.14}$$

where ω is frequency and χ' and χ'' are the out-of-phase and in-phase contributions to the capacitance due to relaxation, respectively. Equation 2.14 indicates that the charge resulting from a real capacitor is frequency dependent and comes from three contributions. The out-of-phase, real contribution will correspond to the charge density

from pure capacitance. The contributions from conductivity and imaginary susceptibility represent the charge density, which does not contribute to the capacitance. Therefore, the dielectric permittivity, must be expressed in complex form as a function of frequency (ω) [3]:

$$\varepsilon^*(\omega) = \varepsilon'(\omega) - i\varepsilon''(\omega) \quad , \tag{2.15}$$

where ε' is the real part of the dielectric permittivity, termed the dielectric constant, $i = \sqrt{-1}$, and ε'' is the imaginary part of the dielectric permittivity, which contains the contributions from in phase components to the permittivity. The dielectric loss is related to the imaginary part of the permittivity, however, it is most often described by the tangent of the dielectric loss angle ($tan\delta$):

$$\tan\delta = \frac{\varepsilon''}{\varepsilon'} \quad , \tag{2.16}$$

where δ is the angle between the imaginary component and the real component of the permittivity, as illustrated in Figure 2.7. In this work the dielectric loss ($tan\delta$) and permittivity (ε') are measured as a function of temperature at various frequencies. The time lag between electrical field and polarization implies an irreversible degradation of free energy. Thus the dielectric loss (or dissipation) factor is a measure of the polarization efficiency at a given frequency, so that the higher the loss, the lower the efficiency.

Figure 2.8 presents a schematic example of a dielectric spectrum showing the decrease in real permittivity with increasing frequency and corresponding imaginary peak. The maximum of the loss peak corresponds to the relaxation time, which is the average attempt time for the dipoles to switch polarization. As the period of the measurement

frequency decreases to less than the relaxation time, the dipoles can no longer react to the electric field and no longer contribute to the permittivity.

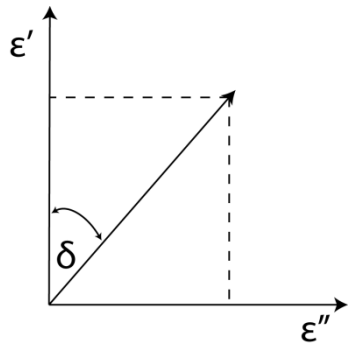

Figure 2.7: Illustration of the definition of the dielectric loss angle (δ) in terms of the imaginary and real components of the permittivity.

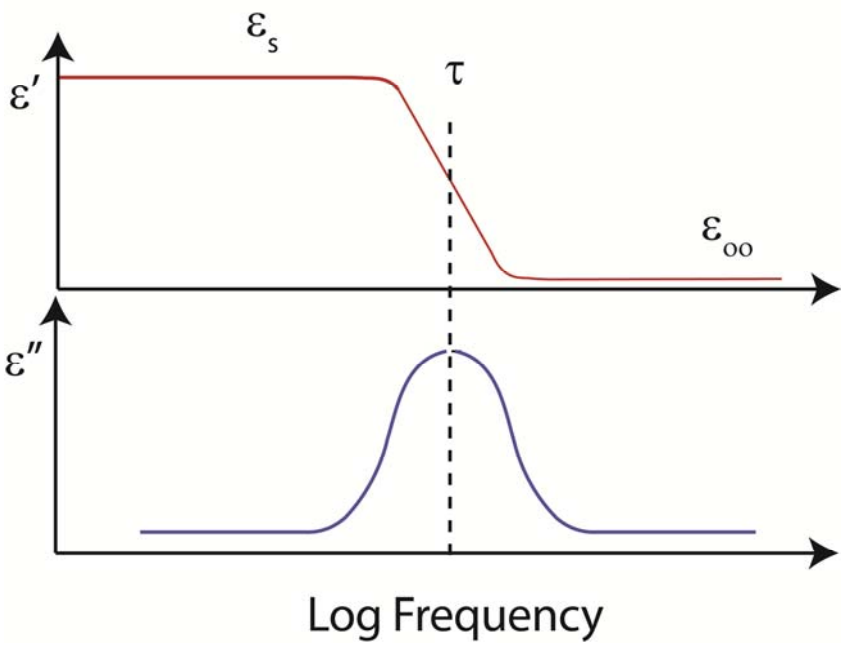

Figure 2.8: Diagram of a dielectric spectrum showing relaxation behaviour. Top: the change in dielectric constant; Bottom: the corresponding imaginary peak (Bottom).

2.5 Ferroelectric Hysteresis Measurements

The ferroelectric properties of the ceramics prepared in this work are characterized using an RT66A Standard Ferroelectric Testing System (Radiant Technologies), which performs measurements of polarization as a function of an electric field. Polarization (P) may be defined as:

$$P = \frac{Q}{A} \quad , \tag{2.17}$$

where Q is the charge developed on the electrodes of the ferroelectric capacitor and A is the area of the electrodes. A Sawyer-Tower circuit allows for the determination of a material's polarization as a function of electric field [4], which gives rise to a ferroelectric hysteresis loop shown in Figure 1.1 in Chapter 1.

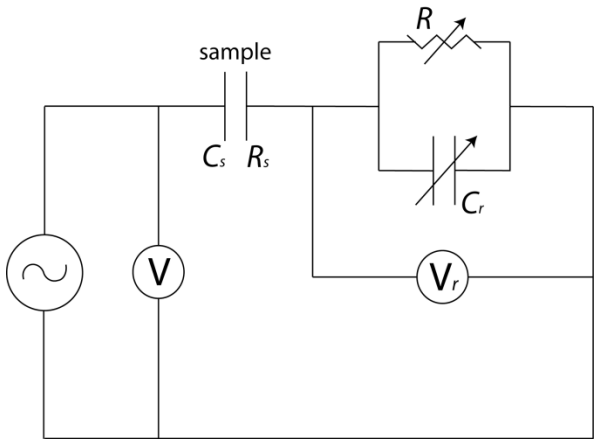

Figure 2.9: A modified Sawyer-Tower circuit for the measurement of ferroelectric hysteresis loops (adapted from Ref. [7]), where C_s, R_s, C_r, R, V, and V_r stand for the capacitance of the sample, the resistance of the sample, the capacitance of the reference, the resistor, the step voltage, and the voltage across the reference capacitor, respectively.

Figure 2.9 shows a schematic of a modified Sawyer-Tower circuit. In this circuit, a step voltage (V) is applied across the two electrodes on the surfaces of a sample capacitor (C_s, with thickness d). Since the thickness is known, the electric field can be calculated by dividing the voltage by the thickness ($E=V/d$) across the sample. The field applied is the quantity plotted on the horizontal x-axis. The sample is then connected in series with a parallel RC circuit, which compensates for any phase shift due to conductivity or dielectric loss in the sample. The voltage (V_r) across the reference capacitor (C_r) is measured, and because the two capacitors are connected in series, the charge on the reference capacitor must be the same as the charge over the sample capacitor. The charge on the ferroelectric sample can then be found by using Equation 2.4, as discussed previously. Once the charge on the sample is known, the polarization can be determined using Equation 2.17 above.

2.6 Piezoelectric Property Measurements

2.6.1 Quasistatic Piezoelectric measurements

The piezoelectric coefficient (d_{33}) of the ceramics studied in this work was measured by a quasi-static method using a Piezo-d_{33}/d_{31} Meter (ZJ-6B). The piezoelectric coefficient is defined by the following equation [5, 6]:

$$d_{33} = \left(\frac{D_3}{\sigma_3} \right)_E \quad , \tag{2.19}$$

where D_3 is the charge density (C/m^2) and σ_3 is the mechanical stress (N/m^2) at constant electric field (E). Figure 2.10 shows a schematic diagram for the d_{33} measurement using the Piezo-Meter.

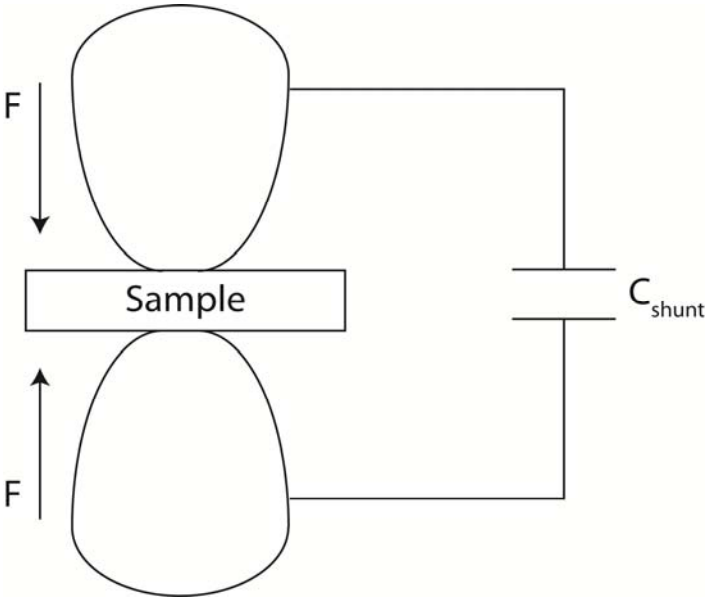

Figure 2.10: A schematic diagram for the d_{33} measurement by a quasi-static method.

When a force (F) is applied on an area (A) of a sample by the upper and lower probes, a piezoelectric charge (Q) is produced due to the piezoelectric effect on the contact area (A), therefore Equation 2.11 can be simplified at follows:

$$d_{33} = \frac{(Q/A)}{(F/A)} = \frac{Q}{F} = \frac{C \times V}{F} \quad , \tag{2.20}$$

where C is the shunt capacitance and V is the potential difference across the shunt capacitor. The Piezo-Meter measures this potential difference, calculates the d_{33} (in pC/N) of the sample and displays the value digitally. Average d_{33} values are reported after taking measurements from various areas across a ceramic sample.

2.6.2 Electric Field-Strain Measurements

Both unipolar and bipolar electric field-strain measurements, were carried out by applying an electric field across a ceramic sample and measuring the relative strain. This measurement is used to calculate the converse piezoelectric coefficient by measuring the

slope of the unipolar electric field vs. strain curve, according to the relation $d_{33}=S/E$ and as well as the coercive field by measuring the bipolar electric field vs. strain relationship, as explained in Section 1.3. The sample in this case is attached to a voltage source and a photonic sensor is used to measure the displacement of the sample surface. Figure 2.11 shows how the sensor functions. The sensor works by having two fibre optic cables, one applying light and the other for sensing, at a fixed distance away from each other. The field of view of the two optic fibres will change in size depending on the relative distance away from the sample, and subsequently, so will the overlap between the fields, so that there is a maximum overlap at a particular fixed distance. This distance will correspond to the maximum intensity of the sensing signal and is used as a set point to calibrate the sensor. With the sensor calibrated, measurements of converse d_{33} can be accurately obtained by applying a known electric field and measuring the strain in the sample.

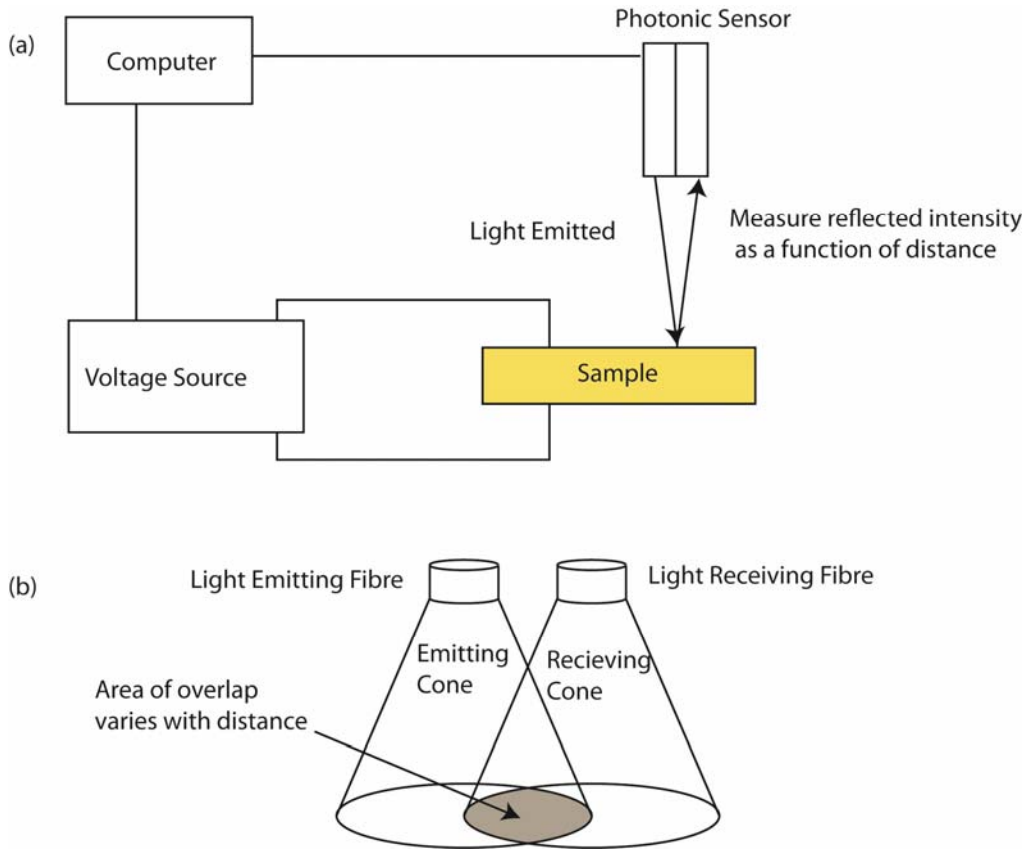

Figure 2.11: (a) Schematic diagram of unipolar electric field-strain measurements using a photonic sensor. (b) Diagram showing the photonic sensor probe which measures the reflected light intensity as a function of the probe distance.

Impedance measurements were also performed to determine the electromechanical coupling factor (k) using a Solartron 1260 impedance analyzer in conjunction with a Solartron 1296 dielectric interface. The electromechanical coupling factor is a measure of the efficiency of how well a piezoelectric material can convert electrical energy into mechanical energy, or vice versa [7]. The particular expression for k to be measured will depend on the dimensions and symmetry of the sample being probed. In this work all the piezoelectric ceramics measured are thin disks with the polarization perpendicular to the plane. A thin piezoelectric ceramic disc, like the materials prepared in this work, will produce its radial vibrations at the lowest frequency when exposed to an

alternating electric field since this is the longest dimension and should resonate at the lowest frequency. The planar coupling factor (k_p) expresses this radial coupling by the following equation[8]:

$$k_p{}^2 = 2.5\frac{(f_a - f_r)}{f_r} \quad , \tag{2.21}$$

where f_a and f_r are the anti-resonance and resonance frequencies, respectively. The resonance frequency is the frequency at which the material vibrates most readily or where the impedance is at a minimum. As the frequency is further increased the impedance reaches a maximum, and it is this frequency that is termed the anti-resonance frequency, as shown in Figure 2.12. Between the resonance and antiresonance frequencies is the frequency range at which the sample most efficiently converts electrical energy into mechanical energy, and vice versa. Once these two frequencies are determined for a ceramic disc, the planar coupling factor can be calculated using Equation 2.21 above.

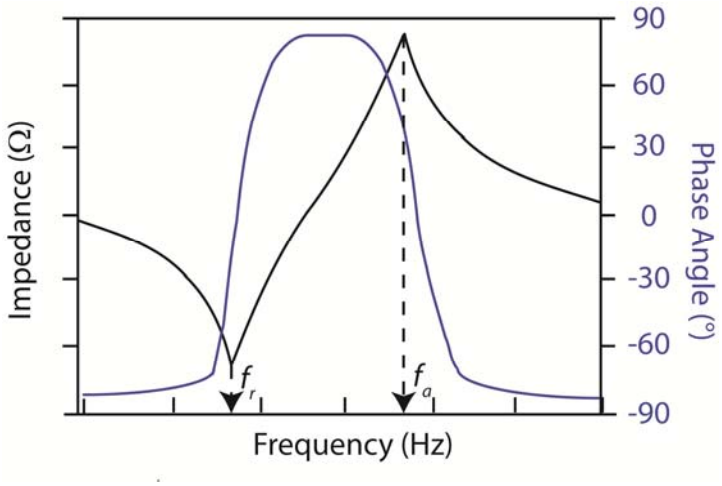

Figure 2.12 Schematic variations of impedance as a function of frequency, displaying resonance (f_r) and anti-resonance (f_a) frequencies and the associated phase angle.

2.7 Scanning Electron Microscopy (SEM)

The microstructures of the ceramics prepared in this work were examined by a Scanning Electron Microscope (SEM), which is a technique that images a sample's surface enabling us to investigate the topography, structure, morphology, grain size, defects, etc., of solid materials.

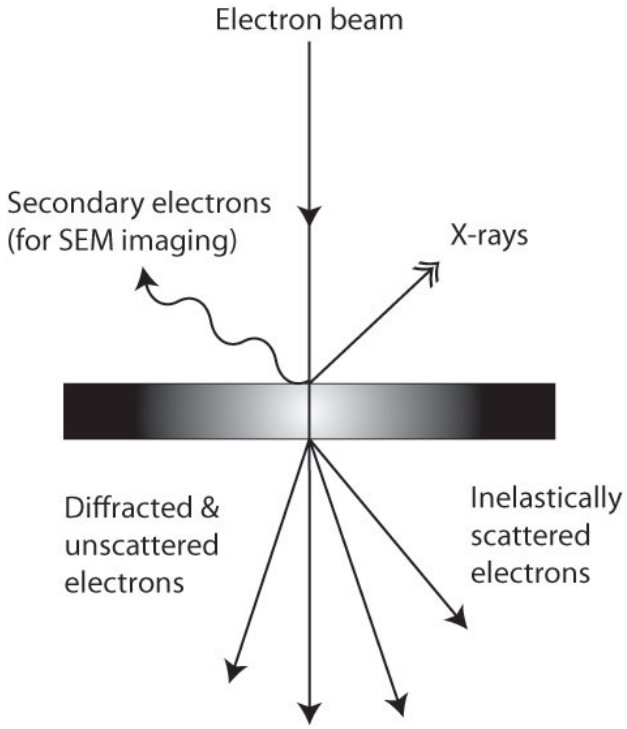

Figure 2.13: The interaction of an electron beam with a sample (adapted from Ref. [12]).

In order to image the sample's surface, an electron beam is thermally emitted from a tungsten filament under vacuum and focused on an area (< 10 nm) and then scanned across the sample (Fig. 2.13). The electrons penetrate the surface and consequently eject other electrons that are detected and used for imaging [12].

References

[1] M. Ladd and R. Palmer, *Structure Determination by X-ray Crystallography* (Kluwer Academic/Plenum Publishers, New York, (2003).

[2] A. R. West, *Basic Solid State Chemistry.* Toronto: Wiley & Sons, (2002).

[3] A. K. Jonscher, *Dielectric Relaxation in Solids.* Chelsea: Chelsea Dielectrics Press, (1983)

[4] C. B. Sawyer and C. H. Tower. Rochelle salt as a dielectric. *Physical Review,* vol 35*,* pp. 0269-0273(1930).

[5] D. Damjanovic. Ferroelectric, dielectric and piezoelectric properties of ferroelectric thin films and ceramics. *Reports on Progress in Physics ,* vol 61*,* pp. 1267-1324 (1998)..

[6] G. H. Haertling.. "Ferroelectric ceramics: History and technology." *ournal of the American Ceraicm Society* vol 82*,* pp. 797-818 (1999).

[7] Y. Xu, *Ferroelectric Materials and their Applications.* Amsterdam: North-Holland, (1991).

[8] *Electrical Measurement Methods for Piezoelectric Ceramics Elements, EMAS-6100* . Japan: Standard of Electronic Materials Manufacter Association, (1993).

[9] Principles and Applications of thermal analysis / edited by Paul Gabbott. Published Oxford ; Ames, Iowa : Blackwell Pub., (2007)

[10] Operating Guide For Model Zj-6B d33 Meter, Institute of Acoustics Chinese Academy of Sciences, Beijing China.

[11] Thermogravimetry/Differential Thermal Analyzer Module TG/DTA 6300 Operation Manual, Seiko Instruments Inc, Scientific Instrument Division (1996)

[12] A. K. Cheetham and P. Day, *Solid State Chemistry: Techniques* (Clarendon Press, Oxford, 1987).

CHAPTER 3:
Enhanced Piezoelectricity and High Temperature Poling Effect in $(1-x)Pb(Mg_{1/3}Nb_{2/3})O_3-xPbTiO_3$ (x =0.28-0.32) Ceramics via an Ethylene Glycol Route

3.1 Abstract

A solution chemical method utilizing ethylene glycol (EG) as solvent has been developed to prepare the ceramics of (1-x)$Pb(Mg_{1/3}Nb_{2/3})O_3$-$x$$PbTiO_3$ [(1-x)PMN-xPT] from a precursor powder that can be pressed and fired in one step to produce high quality ceramics with excellent piezoelectric properties. The ceramics reach a relative density of up to 97% of the theoretical value after direct calcinations. This high density is achieved without the need of additional sintering after calcination, which is usually required in conventional solid state syntheses to produce ceramics. The ceramics exhibit a unipolar piezoelectric coefficient d_{33} of 848 pC/N, which is one of the highest values for any unmodified/untextured binary systems reported to date. Since the piezoelectric properties depend on composition and electric field, the effect of poling conditions was investigated. A critical temperature limit has been found, above which poling can dramatically impair the piezoelectric properties due to a field-induced increase of the monoclinic phase component around the MPB at high temperatures.

3.2 Introduction:

Relaxor ferroelectric-based materials have received much attention for their excellent dielectric and electromechanical properties which include a high dielectric permittivity and high piezoelectric coefficients, making them excellent materials for electromechanical actuators, transducers and sensors. Particular interest has been put on

the solid solution of (1-x)Pb($Mg_{1/3}Nb_{2/3}$)O_3-xPbTiO_3 [(1-x)PMN-xPT] with compositions of x = 0.28 to 0.32 because some of the best piezoelectric properties occur close to the rhombohedral side of the morphotropic phase boundary (MPB) [1-7] in the form of single crystals and ceramics. The increase of piezoelectric properties near the MPB is thought to arise from the coexistence of rhombohedral, tetragonal and monoclinic phases. The presence of the monoclinic phase was believed to facilitate the polarization vector rotation through local energetic minima from the <111> to the <001> direction, giving rise to the enhanced piezoelectric response [2, 8-10]. However, ceramics of (1-x)PMN-xPT are difficult to prepare in completely pure perovskite phase and often require multi-step calcination for synthesis as well as an additional sintering step to produce ceramics. The difficulty in phase formation is due to the volatility of PbO at high temperatures and the differential reactivity between MgO and Nb_2O_5. The volatility of PbO leads to a change in stoichiometry, causing the formation of secondary phases, such as lead niobate pyrochlore, which degrade the dielectric and electromechanical properties. Swartz et al. [11] used a two step precursor method involving the reaction of slight excess of MgO with Nb_2O_5 to form the $MgNb_2O_6$ columbite phase first, which was then reacted with PbO and TiO_2 to form the perovskite phase. In this way, the formation of pyrochlore phase was inhibited. However, this method requires several reaction steps in the synthesis, followed by another high temperature sintering process in order to obtain adequately dense ceramics.

One approach to overcome this issue is to use a soft chemical technique to produce a solution containing all the cationic ingredients as a starting point for the solid state synthesis and ceramic sintering. This method creates molecular level mixing as opposed

to particle level mixing used in the conventional solid state technique, allowing for a higher reactivity and a lower synthesis temperature. Soft chemical synthesis, including the Pechini process [12] and other polymeric precursor methods [13, 14], involve dissolving all the cationic ingredients into a common solvent, permitting ligand exchange and cross-linking. A method was recently developed in our laboratory using polyethylene glycol as the solvent, which promotes the coordination of the metal centres by the terminal hydroxyl groups and by the ether oxygens. The advantage of this method was that the precursor solutions could be prepared at room temperature, followed by pyrolysis at high temperature to remove the organic components. The remaining precursor powder was then pressed into pellets and sintered to achieve complete reaction and densification. In this way high-density ceramics were produced. However, this process still required a high sintering temperature and a longer sintering time, and moreover, it does not yield pure phase for all compositions.

In this work, a solution chemical method using ethylene glycol is developed to prepare the ceramics of the PMN-PT solid solution with compositions close to the MPB. Ethylene glycol is chosen as the solvent because of its ability to dissolve all the starting reagents and to coordinate and crosslink the cations.[15] Furthermore, the fine precursor powder obtained after the pyrolysis process, which possesses a large specific surface area and high reactivity, is advantageous in producing high-density ceramics, which is also necessary for achieving enhanced electromechanical properties.

3.3 Experimental

The ceramics of (1-x)PMN-xPT prepared in this work had the compositions of x = 0.28, 0.30, and 0.32, which lie on the rhombohedral side of the MPB. The starting materials,

used as received, were : ethylene glycol (Reagent grade, Caledon), lead (II) acetate trihydrate [$Pb(CH_3COO)_2 \cdot 3H_2O$] (99.9% Anachemia), magnesium acetylacetone dihydrate [$Mg(O_2C_5H_7)_2 \cdot 2H_2O$] (98+% Alfa Aesar), niobium (V) ethoxide [$Nb(OC_2H_5)_5$] (99.99% Alfa Aesar), and titanium (IV) diisopropoxide bis(acetylacetone) [$Ti(O_2C_5H_7)_2(OC_3H_7)_2$] (75% in Isopropanol, Alfa Aesar). Several conditions were tested in order to dissolve the reagents into the solvent without causing them to precipitate. The starting reagents were used as received and the trials were performed in two steps: first, by stirring at room temperature or at 120°C for two hours with only one reagent in solution, and second, with two reagents in the solution at the two different temperatures. This process was repeated for every combination of the two reagents in order to produce a solution without precipitation. It is imperative to avoid precipitation because it would deteriorate the molecular level mixing and change the chemical composition in the final product from nominal stoichiometry. The results of the trials are shown in Table 3.1. It was found that the magnesium and lead precursors could form a solution when heated together at 120°C, while the niobium and titanium reagents could form a separate solution when stirred together at room temperature without forming any precipitate. The difference in solubility between the two solutions can be explained by the fact that the titanium and niobium reagents have alkoxide ligands, and are much more reactive because their ligand exchange occurs more easily. Heating the solution led to over-crosslinking, polymerization and thus precipitation. The magnesium and lead precursors are diketonates and carboxylates, respectively, which require more vigorous conditions, such as heating to facilitate ligand exchange and crosslinking. A flow chart of the scheme developed is shown in Figure 3.1.

Table 3.1: Solubility of various cationic precursors in ethylene glycol at 25 °C and 120 °C. The optimal conditions are chosen so that precipitation does not occur.

	Ti	Mg	Nb	Pb
Stir at 25 °C in Ethylene Glycol	Dissolves completely	Does not dissolve	Dissolves completely	Does not dissolve
Heat to 120 °C in Ethylene Glycol	Precipitates	Dissolves completely to produce red brown solution upon heating	Precipitates	Dissolves completely, but precipitates if heated longer than 3 hours.

A 5 mole% excess of $Pb(CH_3COO)_2 \cdot 3H_2O$ (2.3324 g) and a 3 mole % excess of $Mg(O_2C_5H_7)_2 \cdot 2H_2O$ (0.4867) were added to ethylene glycol (b.p. 200 °C) and heated at 120 °C for 2.5 hours, giving rise to a red brown solution which was then dried under vacuum at 80 °C for at least 1 hour. A few drops of toluene (b.p. 110.6 °C) were added in to ensure the vacuum and heating conditions were adequate to remove the moisture from the solution. Separately, 1 mL of dry methanol was mixed with 6 mL of ethylene glycol before a stoichiometric amount of niobium ethoxide (1.1741 g) was added, then the methanol was removed by vacuum distillation. The purpose of using the methanol was to dilute the ethylene glycol so that the niobium would not precipitate out from over crosslinking upon initial addition. Once the methanol was removed by vacuum filtration, a stoichiometric amount of $Ti(O_2C_5H_7)_2(OC_3H_7)_2$ (1.1788 g) was added drop-wise and the solution was left to stir for 30 minutes, after which the two solutions were added together to form the final solution. The pyrolysis process and thermal events were investigated by simultaneous thermal gravimetry (TG)/differential thermal analysis (DTA) on a Seiko Exstar 6300 TG/DTA Thermal Analyzer using platinum pans and 10

mg of alumina powder as the reference. The measurements were conducted by placing 10 mg of the precursor solution into a platinum TGA/DTA pan and measuring on heating and cooling between 25 °C to 850 °C, at a rate of 5 °C/min. In order to prepare the precursor powder to produce ceramics the remaining solution was pyrolyzed at 500 °C for two hours, producing an orange red powder. The pyrolyzed powder was ground in acetone and pressed into discs. The pressed pellets were then sintered into ceramics at various temperatures between 650 and 1230 °C in a Pt/Al_2O_3 double crucible setup filled with a sacrificial PMN powder to provide a PbO-rich atmosphere.

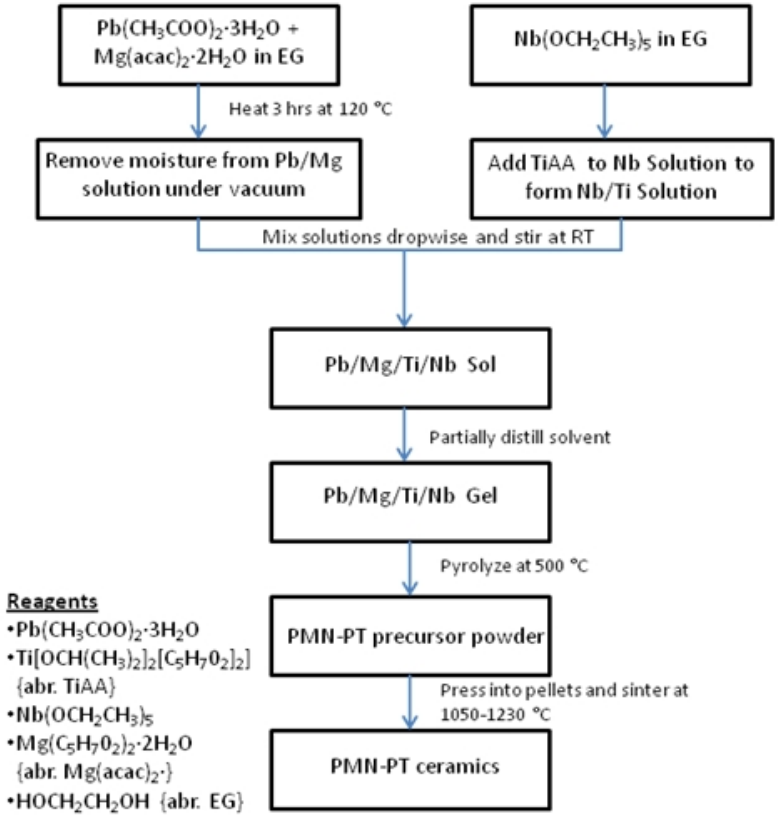

Figure 3.1: Flow scheme of ceramic preparation from the ethylene glycol soft chemical route.

The sintered ceramics were polished using silicon carbide sand paper (220, 400, 600 grit). The ceramics were ground to produce two parallel and flat surfaces and rinsed in acetone using a sonicator before being checked for phase formation by X-ray powder diffraction using Cu K_α radiation (42 mA, 45 kV Rigaku Rapid-Axis Diffractometer, step size = 0.02 °/step, collection time = 2 minutes, 2θ = 10 ° - 80 °). Once phase purity had been verified by comparing to reference patterns [14,20], the polished surfaces were sputtered (Anatech Hummer 6.2, 10 min, 15 mA plasma discharge current) with gold for electrical characterization. In order to connect the electrodes to the electrical characterization equipment and poling apparatus, gold wires were attached to the sample and instrument electrodes using silver paste. The temperature dependence of the dielectric permittivity of the ceramics was measured at various frequencies on a Novocontrol Alpha high resolution broadband dielectric analyzer. The measurements were taken isothermally every 3 °C from 0 °C to 300 °C. The samples were poled at room temperature in silicone oil with an electric field of 15 or 25 kV using a Stanton PS350 high voltage power source. In the case of high temperature poling, a Delta 9023 variable temperature chamber was used to heat the ceramics above their respective Curie temperatures (T_C), or morphotropic phase transition temperature (T_{MPB}), at which an electric field of 15 kV or 25 kV was applied and held during cooling to room temperature before piezoelectric measurements were performed. The electromechanical coupling factors were calculated based on the resonance and antiresonance frequencies found by measuring the room temperature impedance spectrum (frequency range: 200 kHz - 300 kHz, 200 point/decade) with a Solartron S1260 impedance analyzer in conjunction with an S1296 dielectric interface. The piezoelectric constant was measured by means of a

quasistatic piezoelectric meter (Model ZJ-6B, Institute of Acoustics, Chinese Academy of Sciences), and for the samples poled at room temperature, it was also calculated from the strain versus electric field curves measured using a Fotonic Sensor (MTI 2000, MTI Instruments) in conjunction with a computer controlled Keithley 2517A electrometer/voltage source (5 kV/step, 0.3 sec/step). The bipolar strain versus electric field for all of the samples was measured with a maximum applied field of ±10 kV/cm (5 kV/step, 0.3 sec/step).

3.4 Results and Discussion:

3.4.1 Thermal Analysis of Chemical Reactions:

Figure 3.2 shows the TG and DTA signals versus temperature for the PMN-0.32PT solution. The majority of weight loss (77%) occurs at 180 ºC, which is associated with an endothermic peak in the DTA curve, indicating the evaporation process of the solvent. The second small endothermic peak around 200 °C corresponds to the boiling process of ethylene glycol (b.p. =195 °C). The final weight loss occurring between 200 °C and 600 °C arises from the gradual decomposition of the remaining organic substances. The high-temperature broad endothermic peak in the DTA curve between 650°C and 725°C with little or no weight loss indicates the formation of the perovskite phase, as confirmed by the XRD patterns (see Section 3.2).

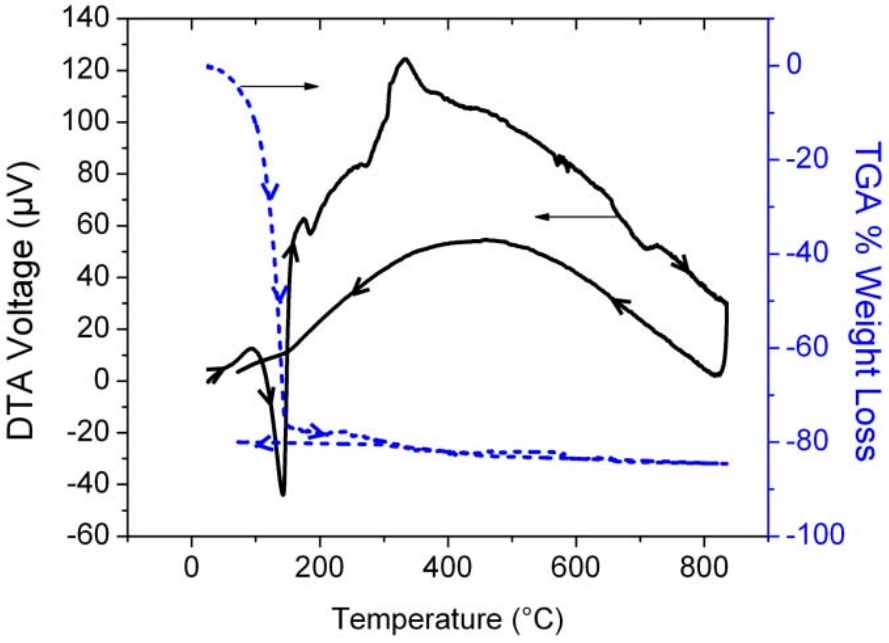

Figure 3.2: TGA/DTA curves of the PMN-0.32PT solution. Initial weight losses with endothermic peaks at 150 °C and 190 °C correspond to the evaporation and boiling of the solvent, respectively. The endothermic peak upon heating around 700 °C indicates the formation of the perovskite phase.

3.4.2 Phase Formation and Densification:

Figure 3.3 shows the X-ray diffraction patterns for the x = 0.32 ceramic sintered at different temperatures. The patterns of the ceramics sintered at low temperature show a significant amount of pyrochlore phase of the $Pb_2Nb_2O_7$ type, which is the kinetically more favourable phase due to the fact that the perovskite phase requires a higher chemical reactivity of magnesium to form [11]. Although the pyrochlore phase is formed from the initial reaction between Nb_2O_5 and PbO, it may contain other ions such as Mg^{2+} and Ti^{4+} [16-18]. As the firing temperature is increased to 950 °C, the perovskite phase is formed. In order to obtain a greater density for the ceramics, a sintering temperature larger than that required for the phase formation temperature is needed. For the sintering

of ceramics above 950 °C, a 5% excess of $Pb(Ac)_2$ is added in order to compensate for the volatilization of PbO and thereby to prevent the formation of the pyrochlore phase. The upper limit of sintering temperature was found to be 1250 °C above which the ceramics began to soften and melt. The variation of density as a function of sintering temperatures for the $x = 0.32$ ceramics is listed in Table 3.2. It can be seen that the relative density continues to increase with increasing sintering temperature above 950 °C and reaches a maximum value of 97% at 1150 °C, above which it does not change. It should be noted that the temperature at which the maximum density is obtained using this technique is lower than that used in the conventional solid state technique. Moreover, in contrast to the solid state technique which usually requires two steps of calcinations and densification, our method produces pure phase ceramics with high density using only one firing step.

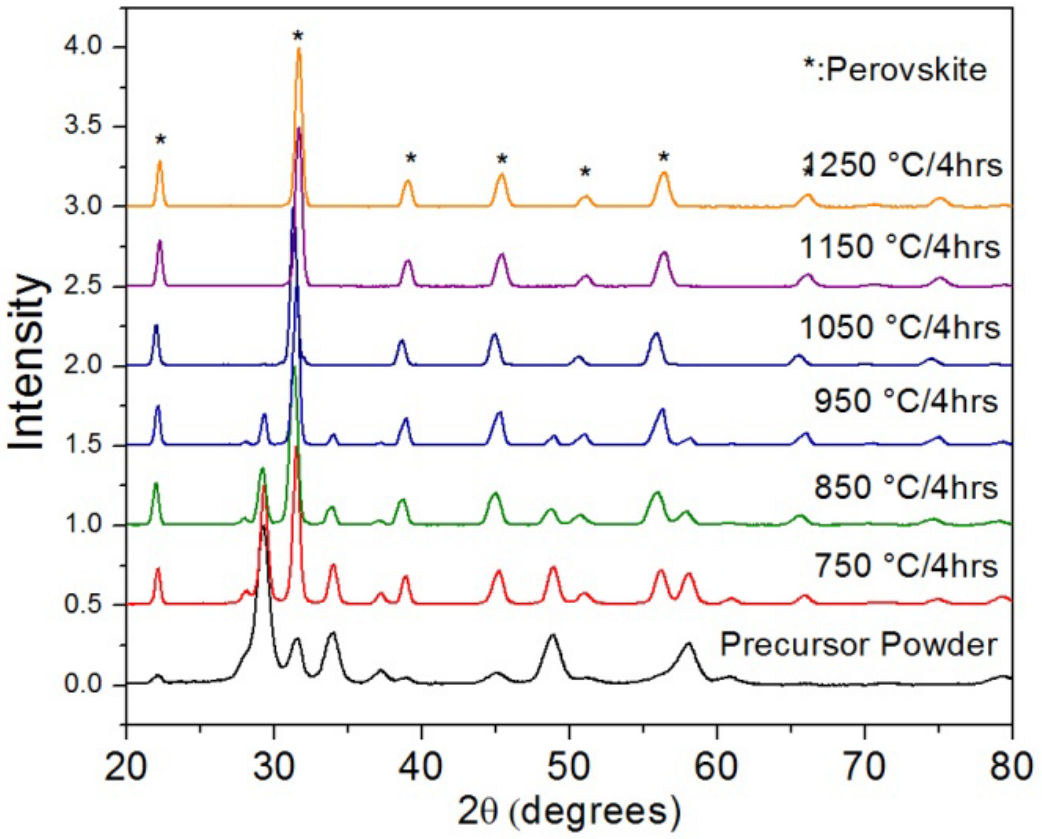

Figure 3.3:X-ray diffraction patterns of x = 0.32 ceramics sintered at various temperatures. Pure perovskite phase forms at temperatures above 950 °C.

Table 3.2: Relative density (D_{rel}) and piezoelectric properties (d_{33}, k_P) as a function of sintering temperature for 0.68PMN-0.32PT ceramics. At temperatures above 1150°C ceramic density and piezoelectric constants saturate.

Sinter. Cond.	Poling Field (kV/cm)	Quasistatic d_{33} (pC/N)	k_p	D_{rel}
1050/4hrs	25	525	0.55	94%
1150/4hrs	25	680	0.71	97%
1230/4hrs	25	680	0.71	97%

3.4.3 Dielectric Properties:

The dielectric properties (real permittivity and loss tangent) as a function of temperature measured at various frequencies are shown in Figure 3.4. The anomalies in the permittivity indicate phase transitions in the samples. The temperatures of the phase

transition are compared to the phase diagram established for the (1-x)PMN-xPT solid solution system to confirm the compositions [10]. In order to reveal the MPB phase transition more clearly, the ceramics were poled at 15 kV/cm at room temperature and the dielectric properties were the measured with zero bias field upon heating. In the x = 0.30 and 0.32 ceramics the real permittivity shows a shoulder at T_{MPB} = 95 and 80 ºC, respectively, corresponding to the rhombohedral to monoclinic phase transition. The values of the transition temperatures match those in the established phase diagrams, confirming that their compositions fall within the MPB region [10]. In the x = 0.28 ceramics, however, no MPB transition is observed, suggesting that this composition lies outside the MPB region and falls into the composition range of the rhombohedral phase[10]. All three samples, x = 0.28, 0.30 and 0.32, show peaks at higher temperatures of 120 °C, 135 °C and 150 ºC, respectively, corresponding to the ferroelectric to paraelectric phase transition temperature, T_C. The phase transitions can also be seen clearly on the dielectric loss tangent curves which show a sharper peak at the T_C, and a local maximum at T_{MPB}, in good agreement with the commonly known dielectric behavior of the materials of the corresponding nominal compositions.

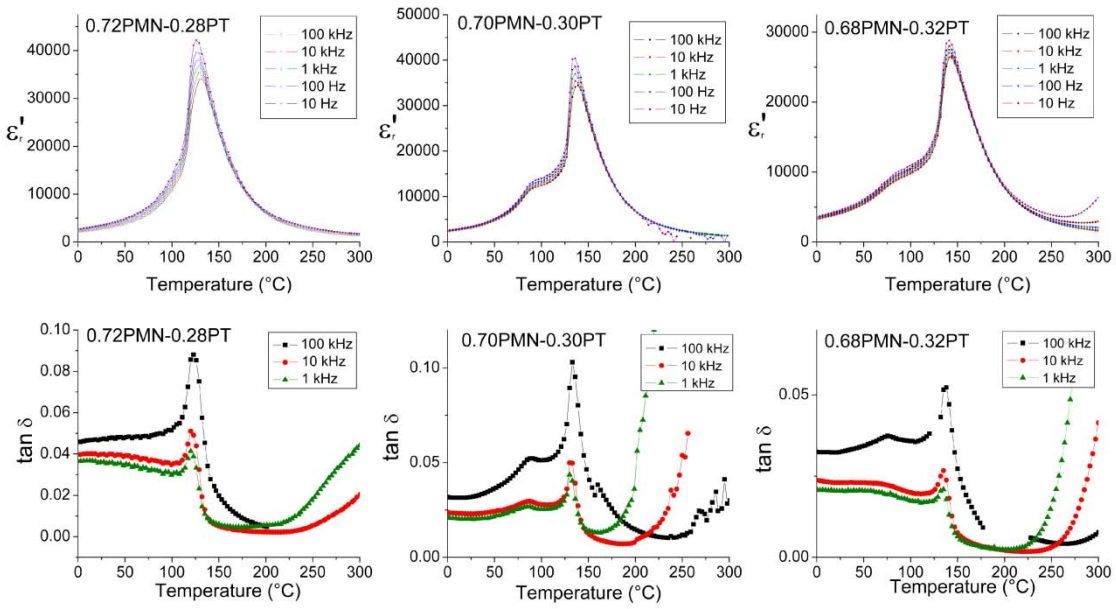

Figure 3.4: Dielectric constant (ε'_r) and loss tangent (tan δ) of x = 0.28, 0.30 and 0.32 ceramics as a function of temperature measured at frequencies between 1 Hz and 100 kHz.

3.4.4 Piezoelectric Characterization

Table 3.2 shows the quasistatic piezoelectric charge coefficients, d_{33}, of the x = 0.28, 0.30 and 0.32 ceramics poled at room temperature with a field of 25 kV/cm. The d_{33} values reach 575, 705 and 680 pC/N, respectively. The maximum value for the x = 0.30 ceramics can be explained by the fact that this composition lies on the phase boundary between rhombohedral and monoclinic phases. The ceramic compositions close to the phase boundary have a lower free energy path for polarization rotation to occur between the $<111>_{cub}$ and $<001>_{cub}$ directions compared to other compositions, which, because of their different symmetry, must overcome an energy barrier in order for the polarization rotation to occur [1, 2, 9]. Figure 3.5 presents the bipolar strain versus electric field with symmetric "butterfly" -like loops for all three compositions, which is characteristic of polarization switching. Since the polarization is coupled to the strain, the change of

polarization is accompanied by a change of strain in the sample. Whether the strain is compressive or tensile depends on the direction of the applied electric field in relation to the polarization. With the field antiparallel to the polarization the strain will be compressive until the coercive field is reached, at which point the polarization switches, causing the strain to change from negative (compressive) to positive (tensile). From the bipolar curves it is possible to obtain the coercive field from the point at which the strain changes from positive to negative with increasing field. This coercive field is the minimum field required for poling and it also limits the bipolar operating range in which a piezoelectric ceramic can be used without switching the polarization. A field of at least three times the coercive field was used to ensure adequate domain switching and complete poling. It was found that $x = 0.30$ has the smallest coercive field required for polarization switching, which may also be a result of its composition lying closest to the MPB. It is interesting to note that the ceramics of $x = 0.28$ exhibit a coercive field, E_C = 5.7 kV/cm, which is much higher than the E_C of PMN-PT single crystals (2-3 kV/cm) of the similar composition [19]. The low E_C represents one of the shortcomings of the piezocrystals, which limits their application at high field. The 0.72PMN-0.28PT ceramics prepared in this work could be used as an alternative to single crystals to overcome this drawback.

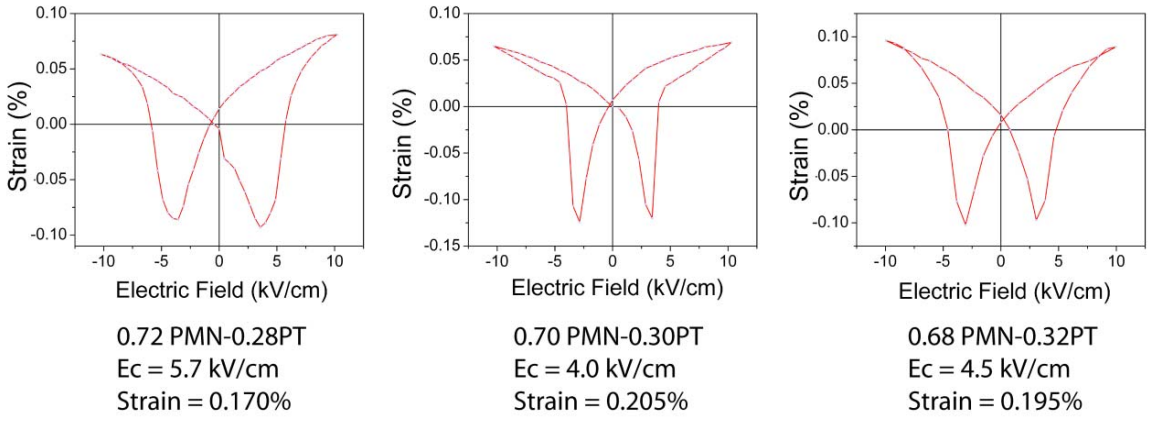

Figure 3.5: Strain versus bipolar electric field (+/- 10 kV/cm) for the (1-*x*)PMN-*x*PT ceramics. The highest strain and lowest coercive fields are found in $x = 0.30$ which is located closest to the rhombohedral/monoclinic phase boundary.

The ceramic processing temperature is known to have a significant effect on the piezoelectric properties because it leads to ceramics of different densities. Table 3.2 shows the quasistatic piezoelectric properties, d_{33} and k_p, versus sintering temperature for the ceramics of composition $x = 0.32$. It can be seen that the piezoelectric properties indeed increase with the sintering temperature and thereby the relative density of the ceramics. The maximum density is reached by sintering at $T = 1150$ °C, the temperature above which both the density and properties saturate.

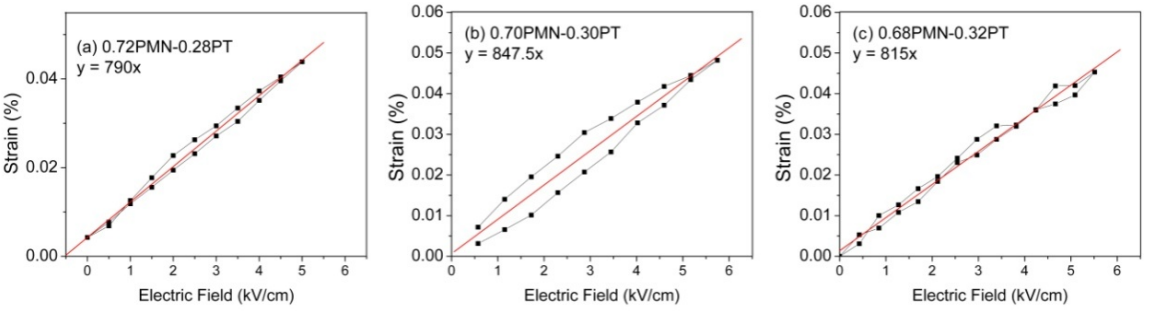

Figure 3.6: Unipolar strain versus electric field for the (1-*x*)PMN-*x*PT ceramics: (a) $x = 0.28$, (b) 0.30 and (c) 0.32, poled with a field of 15 kV/cm at room temperature.

Figure 3.6 shows the unipolar strain versus electric field curves for the ceramic samples poled at an electric field of 15 kV/cm applied at room temperature for 30 minutes. All the samples show a linear piezoelectric response with little or no hysteresis, suggesting that the extrinsic contribution (e.g. domain wall motion) to the piezoelectricity is negligible. From the slope of the curves, the values of piezoelectric coefficients d_{33} are calculated to be 789, 848 and 815 pm/V for the x = 0.28, 0.30 and 0.32 ceramics respectively. The ceramics of x = 0.30 exhibit a d_{33} value of 848 pm/V, which is one of the highest values so far reported for any polycrystalline materials of binary systems. In comparison, the smaller (quasistatic) value of 705 pC/N is possibly due to the initial strain placed on the ceramics to hold the samples in place during the quasistatic measurements, which tends to underestimate the d_{33} values as a result of clamping.

Table 3.3: Dielectric and unipolar piezoelectric properties of PMN-xPT (x = 0.28, 0.30, 0.32) ceramics measured at room temperature.

Composition	ε' (100 kHz)	$tan\ \delta$ (100 kHz)	k_p	Unipolar d_{33} (pm/V)
x =0.28	3210	0.034	0.67	726
x =0.30	3090	0.020	0.73	848
x =0.32	3040	0.020	0.72	815

Table 3.3 summarizes the dielectric and unipolar piezoelectric properties of all three ceramic compositions. All the ceramics exhibit a room temperature dielectric constant, ε' larger than 3000 and a low dielectric loss tangents ($tan\ \delta$) less than 0.035 measured at 100 kHz. The planar electromechanical coupling factor, k_p, was measured according to the IEEE Standard resonance method using the formula

$$1/(k_p)^2 = 0.398[f_r/(f_a-f_r) + 0.579], \quad (3.1)$$

where f_r and f_a are the resonance and antiresonance frequencies corresponding to the minimum and maximum of the impedance spectrum, respectively, as shown in Figure 3.7. All the samples show typical behaviour for a normal dielectric away from the resonance frequency in which the impedance is inversely proportional to the measurement frequency due to a capacitive charging effect. The impedance was measured on both samples that were unpoled (not shown) and poled in order to ensure that any observed resonances were indeed from electromechanical coupling and not from an LC resonance from the measurement circuit. All three ceramics show a maximum phase angle shift of at least 170° during resonance. From the values of the resonance and antiresonance frequencies, the k_p value is found to be 73% for $x = 0.30$, which is among the highest values reported for any unmodified/un-textured binary solid solution systems. The highest coupling factor is consistent with the highest d_{33} value found in the 0.70PMN-0.30PT ceramics [20].

The high piezoelectric properties measured from these ceramics are believed to result from their higher density compared to conventionally prepared ceramics. This is due to the fact that in this work the ceramics are synthesized from direct sintering of fine-grain, and highly reactive precursor powder resulting from the soft chemical route. The large surface area and high reactivity facilitate ionic diffusion, and thereby the perovskite phase formation, while reducing porosity and increasing density.

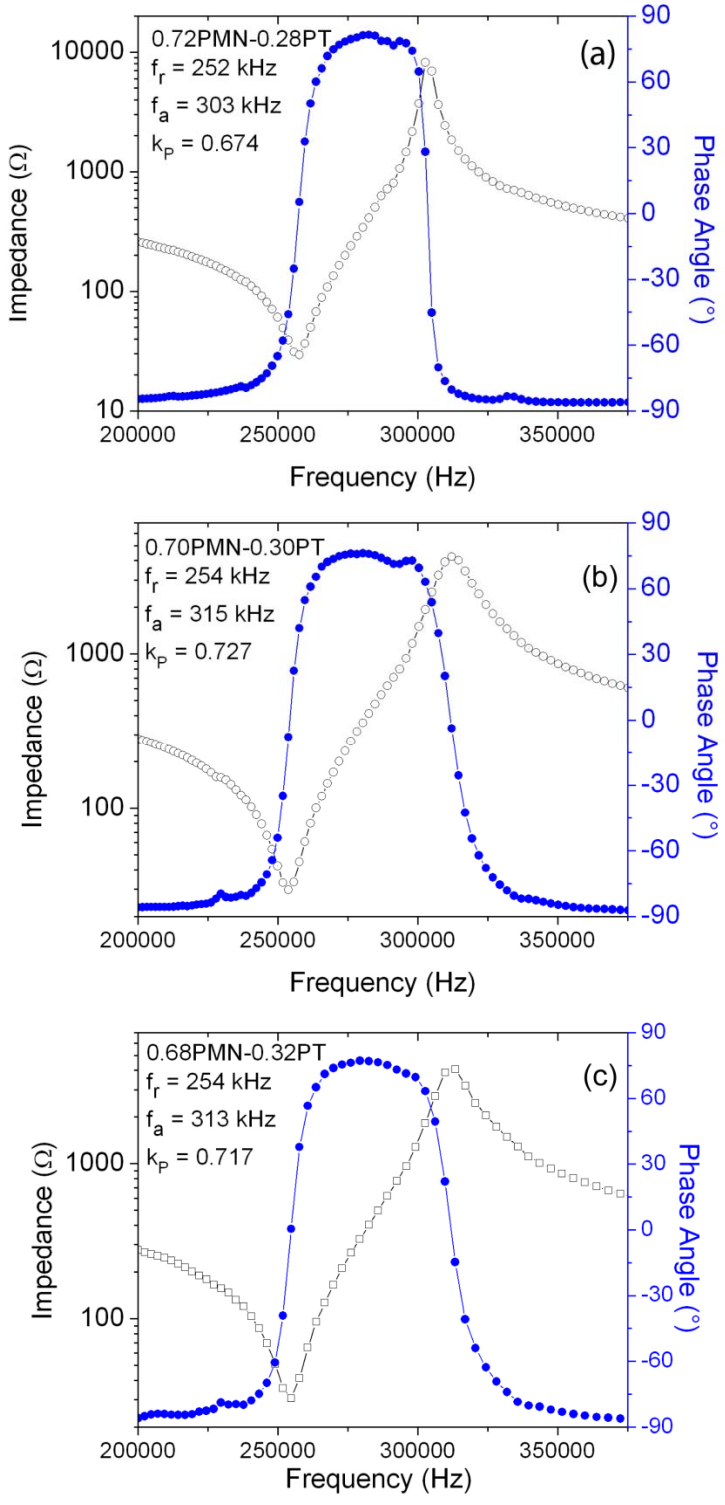

Figure 3.7 (a-c): Impedance spectra of PMN-*x*PT ceramics: (a) *x* = 0.28, (b) *x* = 0.30, and (c) *x*= 0.32, showing phase angle and resonance/antiresonance frequencies from which the planar electromechanical coupling factors are calculated.

3.5 Poling Effect on Piezoelectric Performance

It is known that poling conditions affect piezoelectric properties of PMN-PT single crystals. In order to study the effects of high temperature poling on the piezoelectric properties of the PMN-PT ceramics, the samples were poled at room temperature, and at a temperature above T_{MPB} or T_C (i.e. 100° C for x = 0.30, 90 °C and 100°C for x = 0.32 and 150 °C for x = 0.28). For poling above room temperature, the ceramics were heated to a given temperature, held for ten minutes and cooled to room temperature with the applied electric field. The quasistatic piezoelectric properties measured at room temperature after various poling conditions are shown in Table 3.4. It can be seen that in 0.68PMN-0.32PT ceramics poling above T_{MPB} (90 ºC) degrades the piezoelectric constant, d_{33}. The degradation is made more significant by poling at a higher temperature (100 °C). This effect becomes less dramatic for the 0.70PMN-0.30PT ceramics. It is interesting to note that the 0.72PMN-0.28PT ceramic samples, whose composition lies outside the MPB, do not suffer any degradation. This indicates that the electric field-induced piezoelectric degradation in the PMN-PT ceramics is dependent on temperature. According to the phase diagram in Ref. [10], 0.68PMN-0.32PT contains a major component of the monoclinic phase, while x = 0.30 and 0.28 are of rhombohedral symmetry. It seems that there is a lower tendency for piezoelectric degradation to occur as the composition shifts towards the rhombohedral phase region of the phase diagram, which contains a small, or zero component of the monoclinic phase. The ceramics of x = 0.28 show a resistance to high temperature poling degradation as this composition lies furthest from the monoclinic phase boundary. The degradation of piezoelectric properties

upon poling has been known in piezoelectric single crystals as the over poling effect, which is caused by an electric field induced phase transition into the monoclinic state [1, 19, 21]. It has been shown in the case of over poling that the applied electric field increases the monoclinic phase component at room temperature at the expense of the rhombohedral phase so as to degrade the piezoelectric performance because the piezoelectric response of the monoclinic phase is lower than the rhombohedral phase of composition near the MPB. The results of this work show that poling at high temperature also leads to piezoelectric degradation because the increase in temperature lowers the energy barrier required for the induced monoclinic phase transition to take place [22].

Table 3.4: Quasistatic piezoelectric charge constant, d_{33} of the 0.68PMN-0.32PT ceramics of different composition poled at different temperatures. Compositions closer to the rhombohedral side are less susceptible to degradation of piezoelectric properties from high temperature poling.

Composition	Poling Field (kV/cm)	Poling Temperature (°C)	Quasistatic d_{33} pC/N
x = 0.28	25	25	575
	25	100	575
	25	150	575
x = 0.30	25	25	705
	25	100	630
x = 0.32	25	25	680
	25	90	540
	25	100	500

3.6 Conclusions:

A new ethylene glycol-based solution route has been developed to produce fine (1-x)PMN-xPT solid solution precursor powders which can be pressed and sintered directly into highly dense ceramics with pure perovskite phase. This technique eliminates the

need for producing B-site precursors and the need for additional sintering after calcination as required in the conventional solid state process. The 0.70PMN-0.30PT ceramics prepared by this direct method show a relative density of 97%, a unipolar piezoelectric charge constant of 848 pm/V and a planar coupling constant k_P = 0.73. These samples exhibit the highest piezoelectric performance for any unmodified/un-textured piezoceramics of binary systems. The coercive fields of all three ceramics are larger than those of single crystals of the same composition, with the highest coercive field of E_C = 5.7 kV/cm found in 0.72PMN-0.28PT, providing a larger bipolar operating range. It was found that poling at temperatures above the T_{MPB} degrades the room temperature piezoelectricity for the x = 0.30 and x = 0.32 ceramics, whose compositions are inside the MPB region, whereas the ceramics of composition x = 0.28, which lies on the rhombohedral side of the MPB, do not suffer degradation when poled at a temperature above T_C. The degradation of the piezoelectric properties can be explained by the electric field-induced increase of the monoclinic phase component in the ceramics of compositions close or within the MPB region, consistent with the over poling effect observed in the PMN-xPT single crystals [19, 22-24]. The PMN-xPT ceramics prepared by the soft chemical route present enhanced piezoelectric performance. They are expected to find applications in high-power electromechanical transducers as an alternative to (1-x)PMN-xPT single crystals.

References

[1] S. E. E. Park and W. Hackenberger, "High performance single crystal piezoelectrics: applications and issues," *Current Opinion in Solid State and Materials Science,* vol. 6, pp. 11-18 (2002).

[2] S. E. Park and T. R. Shrout, "Ultrahigh strain and piezoelectric behavior in relaxor based ferroelectric single crystals," *Journal of Applied Physics,* vol. 82, pp. 1804-1811, (1997).

[3] S. W. Choi, T. R. Shrout, S. J. Jang and A. S. Bhalla, "Dielectric and Pyroelectric Properties in the $Pb(Mg_{1/3}Nb_{2/3})O_3$-$PbTiO_3$ System," *Ferroelectrics,* vol. 100, pp. 29-38 (1989).

[4] D. Zekria and A. M. Glazer, "Automatic determination of the morphotropic phase boundary in lead magnesium niobate titanate $Pb(Mg_{1/3}Nb_{2/3})_{(1-x)}Ti_xO_3$ within a single crystal using birefringence imaging," *Journal of Applied Crystallography,* vol. 37, pp. 143-149 (2004).

[5] Z-. G. Ye, "High Performance Single Crystals of Complex Perovskite Solid Solutions," *Materials Research Bulletin,* vol. 34, pp. 277-282 (2009).

[6] Q. M. Zhang, J. Zhao, T. R. Shrout and L. E. Cross, "The effect of ferroelastic coupling in controlling the abnormal aging behavior in lead magnesium niobate-lead titanate relaxor ferroelectrics," *Journal of Materials Research,* vol. 12, pp. 1777-1784 (1997).

[7] M. Dong and Z-. G. Ye, "High-temperature solution growth and characterization of the piezo-/ferroelectric (1-x) $Pb(Mg_{1/3}Nb_{2/3})O_3$-x $PbTiO_3$ [PMNT] single crystals," *Journal of Crystal Growth,* vol. 209, pp. 81-90 (2000).

[8] B. Noheda, D. E. Cox, G. Shirane, S. E. Park, L. E. Cross and Z. Zhong, "Polarization rotation via a monoclinic phase in the piezoelectric 92% $PbZn_{1/3}Nb_{2/3}O_3$-8% $PbTiO_3$," *Physical Review Letters,* vol. 86, pp. 3891-3894, (2001).

[9] H. X. Fu and R. E. Cohen, "Polarization rotation mechanism for ultrahigh electromechanical response in single-crystal piezoelectrics," *Nature,* vol. 403, pp. 281-283, (2000).

[10] B. Noheda, D. E. Cox, G. Shirane, J. Gao and Z. G. Ye, "Phase diagram of the ferroelectric relaxor (1-x) $Pb(Mg_{1/3}Nb_{2/3})O_3$-x $PbTiO_3$," *Physical Review B,* vol. 66, pp 054104:1-10 (2002).

[11] S. L. Swartz and T. R. Shrout, "Fabrication of Perovskite Lead Magnesium Niobate," *Materials Research Bulletin,* vol. 17, pp. 1245-1250 (1982).

[12] M. P. Pechini, "Method of preparing lead and alkalina earth titanate and niobates and coating method using the same to form a capacitor, US Patent No. 3 330 697," (1967).

[13] K. Babooram, H. Tailor and Z. G. Ye, "Phase formation and dielectric properties of 0.90 $Pb(Mg_{1/3}Nb_{2/3})O_3$-0.10$PbTiO_3$ ceramics prepared by a new sol-gel method," *Ceramics International,* vol. 30, pp. 1411-1417, 2004.

[14] K. Babooram and Z. G. Ye, "Polyethylene glycol-based new solution route to relaxor ferroelectric 0.65$Pb(Mg_{1/3}Nb_{2/}3)O_3$-0.35$PbTiO_3$," *Chemistry of Materials,* vol. 16, pp. 5365-5371, Dec. 2004.

[15] X. C. Jiang, Y. L. Wang, T. Herricks and Y. N. Xia, "Ethylene glycol-mediated synthesis of metal oxide nanowires," *Journal of Materials Chemistry,* vol. 14, pp. 695-703, (2004).

[16] H. Beltran, N. Maso, B. Julian, E. Cordoncillo, J. B. Carda, P. Escribano and A. R. West, "Preparation and characterization of compositions based on PbO-MgO-Nb_2O_5 using the sol-gel method," *Journal of Sol-Gel Science and Technology,* vol. 26, pp. 1061-1065, (2003).

[17] R. J. Cava, W. F. Peck and J. J. Krajewski, "Pyrochlore based oxides with high dielectric constant and low temperature coefficient," *Journal of Applied Physics,* vol. 78, pp. 7231-7233, (1995).

[18] R. Ubic and I. M. Reaney, "Structure and dielectric properties of lead pyrochlores," *Journal of the American Ceramic Society,* vol. 85, pp. 2472-2478 (2002).

[19] A. A. Bokov and Z-. G. Ye, "Field-induced shift of morphotropic phase boundary and effect of overpoling in (1-x)$Pb(Mg_{1/3}Nb_{2/3})O_3$-x$PbTiO_3$ piezocrystals," *Applied Physics Letters,* vol. 92, (2008).

[20] E. M. Sabolsky, S. Trolier-McKinstry and G. L. Messing, "Dielectric and piezoelectric properties of fiber-textured 0.675$Pb(Mg_{1/3}Nb_{2/3})O_3$- 0.325$PbTiO_3$ ceramics," *Journal of Applied Physics,* vol. 93, pp. 4072-4080 (2003).

[21] M. Shanthi, S. M. Chia and L. C. Lim, "Overpoling resistance of [011]-poled $Pb(Mg_{1/3}Nb_{2/3})O_3$-$PbTiO_3$ single crystals," *Applied Physics Letters,* vol. 87, (2005).

[22] K. G. Webber, R. Z. Zuo and C. S. Lynch, "Ceramic and single-crystal (1-x)PMN-xPT constitutive behavior under combined stress and electric field loading," *Acta Mater.,* vol. 56, pp. 1219-1227, (2008).

[23] E. A. McLaughlin, T. Liu and C. S. Lynch, "Relaxor ferroelectric PMN-32%PT crystals under stress, electric field and temperature loading: II-33-mode measurements," *Acta Materialia,* vol. 53, pp. 4001-4008, (2005).

[24] T. Q. Liu, C. S. Lynch and E. A. McLaughlin, "Thermodynamics of stress and electric field induced phase transition in relaxor ferroelectric crystals," *J. Intell. Mater. Syst. Struct.,* vol. 18, pp. 409-415 (2007).

CHAPTER 4:
Soft Chemical Synthesis and Dielectric Characterization of $(1-x)Pb(Mg_{1/3}Nb_{2/3})O_3–xPbTiO_3$ (x = 0.07 and 0.10) Ceramics via an Ethylene Glycol Route

4.1 Abstract

Materials based on relaxor ferroelectrics posseses some of the best properties such as high piezoelectric coefficients and extremely large dielectric constants. Because of these excellent properties they have become one of the most important families of functional materials being explored for such applications as sensors/actuators, micro-electromechanical systems (MEMS), non-volatile random access memories, and high energy density capacitors. In this work a new soft chemical synthetic method for the preparation of the complex perovskite-based relaxor ferroelectric solid solutions, $(1-x)Pb(Mg_{1/3}Nb_{2/3})O_3$ - $xPbTiO_3$ was developed using ethylene glycol as the solvent. Ceramics with compositions of x = 0.07 and 0.10 were prepared and it was found that a 10 % stoichiometric excess of Pb^{2+} was required to compensate for lead volatility at the high temperatures used for sintering. The ceramics produced by this method show excellent dielectric properties at room temperature such as a high dielectric constant (> 20 000) and low loss over a large temperatures range (< 0.01 between 100 - 200 °C). The temperature dependence of the dielectric constant of the compositions studied exhibit typical relaxor ferroelectric behaviour which can be well fit to a quadratic law which describes the high temperature slope of $\varepsilon'(T)$ in relaxors. The frequency dispersion of the temperature of maximum permittivity satisfies the Vogel-Fulcher law, with a freezing temperature, T_f which indicates the temperature at which the polar nanoregions contributing to the relaxor polarization freeze.

4.2 Introduction:

Relaxor ferroelectrics and their solid solutions have gained much attention recently due to their interesting nanostructure and extraordinary properties [1-4]. Unlike normal ferroelectrics, in which the dielectric permittivity diverges to give a sharp maximum at the Curie temperature, T_C, the dielectric behaviour of relaxors is characterized by a broad and frequency-dependent maximum of permittivity which is not associated with a macroscopic phase transition. Relaxors posses a disordered crystal structure and are often found in the form of complex perovskites of the formula $(A'_{(1-x)}A''_x)(B'_{(1-y)}B''_y)O_3$ with two or more heterovalent ions occupying crystallographically equivalent sites [2]. In these materials, polar nanoregions (PNRs) are formed instead of macroscopic domains because the chemical/crystallographic disorder created from hetero-occupancy. This disorder prevents interactions of the same type (ferroelectric or antiferroelectric) from forming over large areas and instead leads to frustration among the interacting forces between the polar regions [5]. For example, regions rich in one type of ion in a given site may favour ferroelectric ordering, whereas regions with an equal number of both ions may favour antiferroelectric ordering, or vice versa, but because of compositional inhomogeneity, long range polar order is not able to form across the whole material.[6] The dynamics of the PNR's is such that at high temperatures they begin to nucleate and are free to fluctuate due to thermal motion. Upon cooling, the reorientation of the PNR's slows down and freezes in a random, disordered polar state. It is because of this slowing down of dynamics that relaxor ferroelectrics are characterized by a broad and frequency dependent maximum of permittivity, which is not associated with any macroscopic phase transition [3]. In particular, the solid solution of (1-

x)Pb($Mg_{1/3}Nb_{2/3}$)O_3-xPbTiO_3, [(1-x)PMN-xPT] (x =0.5-0.10) has been the subject of extensive study due to the high dielectric constant, slim polarization versus electric field loop and outstanding electrostrictive effect near room temperature. These properties make the (1-x)PMN-xPT solid solution of this composition range excellent materials for dielectric capacitors and high precision actuators.

Furthermore, as described in Chapter 1, that the high temperature slope of the real permittivity (> T_{max}) in relaxors, can be described by an empirical formula:[7, 8]

$$\frac{\varepsilon_A}{\varepsilon'} = 1 + \frac{(T - T_A)^2}{2\delta^2} \quad , \tag{4.1}$$

where T_A , ε_A define the temperature and the maximum of static conventional relaxor permittivity, respectively and δ describes the shape or the diffuseness of the permittivity peak. This quadratic law has been used to analyze relaxor ferroelectric solid solutions with a focus on modeling the static contribution of the conventional relaxor susceptibility, which is described in further detail in Chapter 5. It can be used to measure the diffuseness of a phase transition since the δ parameter quantifies the broadness of the permittivity peak. This equation has been applied to some compositions of (1-x)PMN-xPT, but not yet to the ceramics made by this solution chemical method in which the statistical contribution of the dipole moments to the permittivity as a function of temperature remains unknown.

Although the PMN-PT solid solution of compositions rich in PMN($x \leq 0.10$) shows very interesting properties, its ceramics are difficult to synthesize in pure perovskite phase and high density. This is due to an undesirable pyrochlore phase of the $Pb_2Nb_2O_{7-y}$ type which forms as a result of lead deficiency due to PbO volatility at high temperatures, as well as the differential reactivity between Nb_2O_5 and MgO [9]. One

manner to overcome this problem is to use a wet chemical process to produce a solution containing all the cationic ingredients as a starting point for the solid state synthesis [10-13]. Following successful synthesis of PMN-PT ceramics of MPB compositions (Chapter 3), in this work, a solution chemical method is developed to fabricate ceramics with $x = 0.07$ and 0.10. The ceramics produced by this method are characterized to understand their mechanism of phase formation and analysis of the dielectric spectra to reveal the variation of dielectric properties as a function of their composition, synthetic and thermal processing.

4.3 Experimental:

The (1-*x*)PMN-*x*PT ceramics with $x = 0.07$ and 0.10 were prepared by a chemical solution method using ethylene glycol (regent grade, Caledon) as the solvent. The starting materials, used as received, were lead (II) acetate trihydrate [$Pb(CH_3COO)_2 \cdot 3H_2O$] (99.9 Alfa Aesar), magnesium acetylacetate dihydrate [$Mg(O_2C_5H_7)_2 \cdot 2H_2O$] (98+ % Alfa Aesar), niobium (V) ethoxide [$Nb(OC_2H_5)$] (99.999 % Alfa Aesar) and titanium diisopropoxide bis(acetylacetate) [$Ti(OC_3H_7)_2(O_2C_5H_7)_2$] (75% in isopropanol).

A flow chart of the procedure is described in Figure 4.1. Three separate solutions of different Pb^{2+} content (with 0, 5 and 10 % mole percent of excess of Pb^{2+}, respectively) were prepared by dissolving $Pb(CH_3COO)_2 \cdot 3H_2O$ (5.246 g) into ethylene glycol (b.p. = 200 °C). To each of these three solutions a 3 mole % excess of $Mg(O_2C_5H_7)_2 \cdot 2H_2O$ (0.8368 g) was added to ethylene glycol and heated at 120 °C for 2.5 hours, giving rise to a red brown solution which was then dried under vacuum at 80 °C for at least 1 hour. A

few drops of toluene (b.p. = 110.6 °C) were added to ensure the vacuum and heating conditions were adequate to remove the moisture from the solution. Separately, 1 mL of dry methanol was mixed with 6 mL of ethylene glycol before a stoichiometric amount of niobium ethoxide (2.000 g) was added. The methanol was then removed by vacuum distillation. The purpose of using the methanol was to dilute the ethylene glycol so that the niobium would not precipitate out from over crosslinking upon initial addition. Once the methanol was removed by vacuum filtration, a stoichiometric amount of $Ti(O_2C_5H_7)_2(OC_3H_7)_2$ (2.130 g) was added drop-wise and the solution was left to stir for 30 minutes, after which the two solutions were added together and pyrolyzed at 500 °C for two hours, producing an orange red powder. The pyrolyzed powder was ground in acetone and pressed into discs using a 10 mm die. The pressed pellets were then sintered into ceramics at various temperatures between 950 and 1150 °C in a Pt/Al_2O_3 double-crucible setup filled with sacrificial PMN powder to provide a PbO-rich atmosphere.

The sintered ceramics were polished using silicon carbide sand paper (220, 400, 600 grit) to produce parallel flat surfaces. The polished surfaces were used for phase formation analysis by X-ray powder diffraction using Cu K_α radiation, (42 mA, 45 kV Rigaku Rapid-Axis Diffractometer, step size = 0.02 °/step, collection time = 2 minutes, 2θ = 10 ° - 60 °) and sputtered with gold layers (Anatech Hummer 6.2, 10 min, 15 mA plasma discharge current) as electrodes for electrical characterization. Scanning electron microscopy (SEM) images were taken on a FEI Dualbeam Field-Emission SEM. The temperature dependence of the dielectric permittivity of the ceramics was measured at various frequencies on a Novocontrol Alpha high resolution broadband dielectric analyzer. The dielectric measurements were taken isothermally every 3 K from 550 K to

275 K. Variable-temperature polarization versus electric field ($P(E)$) measurements were taken using an ferroelectric testing instrument (Radiant Technologies RT66a, ± 13 kV/cm, 100 points, 10 Hz) in conjunction with a Delta 9023 variable temperature chamber in which the sample was cooled to the desired temperature, allowed to equilibrate for 15 minutes before the $P(E)$ loops were measured.

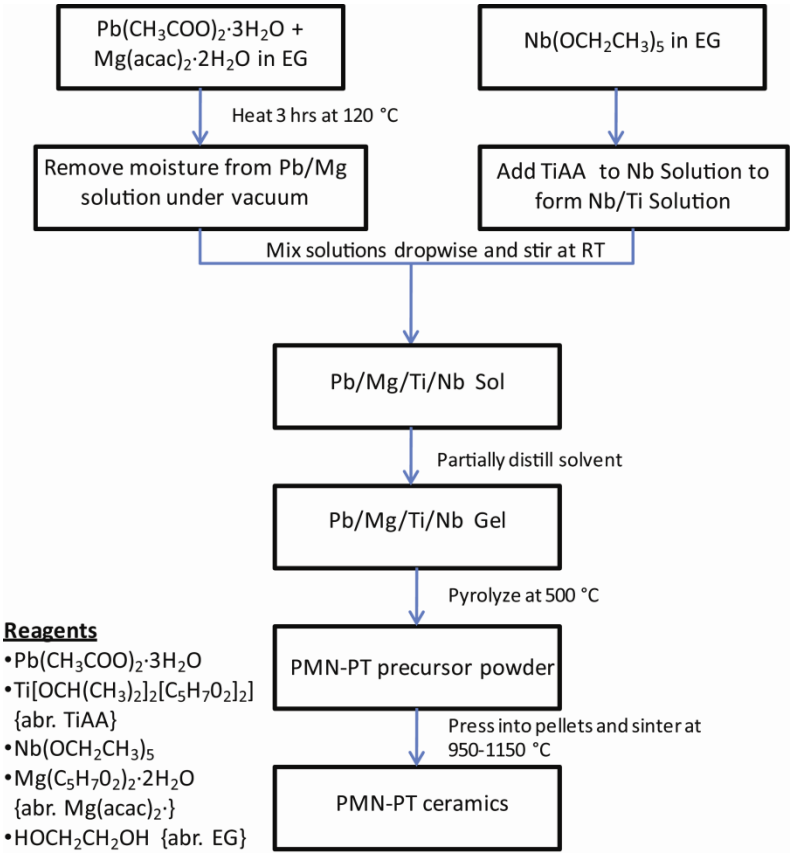

Figure 4.1: Flow chart describing the synthesis of the (1-*x*)PMN-*x*PT ceramics.

4.4 Results/Discussion:

4.41 Phase Formation and Sintering Mechanism:

Figure 4.2 shows the X-ray diffraction patterns of the 0.90PMN-0.10PT ceramics sintered at various temperatures with different amounts of excess Pb^{2+} in the precursor

solution. The phase formation of the 0.90PMN-0.10 ceramics at low temperature is similar to that described in Chapter 3, in which a sintering condition of 950 °C/4 hours is required for the perovskite phase to be formed, however, in order to obtain higher density ceramics, a sintering temperature larger than that required for the phase formation temperature must be used.

However, it was found that the pyrochlore phase reappeared during the sintering process at 1050 °C/4 hours. To sinter at higher temperature while avoiding the formation of pyrochlore, excess lead content was needed in the precursor powders in order to compensate for PbO volatility. A 5% excess of Pb^{2+} gave rise to ceramics of pure perovskite phase after sintering at 1050°C/4 hours (Fig.4.2(b)). A 10% excess of lead is required to sinter the ceramics at 1150 °C/4hours with no detectable pyrochlore phase in the XRD spectra, resulting in a higher relative density of 97%. This amount of Pb^{2+} excess is greater than that required in producing (1-*x*)PMN-xPT ceramics by the ethylene glycol route of compositions near the morphotropic phase boundary (Chapter 3). This may be because the perovskite structure becomes more stable with a higher titanium concentration on the B-site, given the fact that the pyrochlore phase is formed by the reaction of Pb^{2+} with the Nb^{5+}. Table 4.1 gives the relative densities of the 0.90PMN-0.10PT ceramics prepared under various sintering conditions and precursor compositions that gave pure perovskite phase. It is apparent that the higher sintering temperature of 1150 °C led to the ceramics of good quality with a density reaching 97%.

Figure 4.3 shows the SEM images of the of the : (a) 950 °C held for 4 hours with stoichiometric $Pb(OAc)_2$, (b) held 4 hours at 1050 °C with 5% excess $Pb(OAc)_2$ and (c) held 4 hours at 1150 °C with 10% excess $Pb(OAc)_2$. The images indicate that the

average grain size increases with increasing sintering temperature and excess $Pb(OAc)_2$ from 1-3 μm for the 950 °C/4hour samples to the largest grain size of 5-7 μm for the ceramics sintered at 1150 °C/4hour with 10% excess $Pb(OAc)_2$. The increase in density and grain size may arise for two reasons. Firstly, the higher ceramic processing temperatures provides greater thermal activation energy for grain growth and elimination of pores, favouring a more effective sintering process, thereby leading to higher density. Secondly, the excess lead used in the sol, in the form of PbO (T_{mp} = 888 °C), which remains after pyrolysis, serves as a liquid phase sintering aid by decreasing the melting point of the mixture through a eutectic mechanism, thus further enhancing the pore elimination and sintering processes. At the end of the sintering at high temperature the excess PbO compensated for the evaporation to result in stoichiometric 0.90PMN-0.10PT ceramics.

Table 4.1: Relative density of 0.90PMN-0.10PT ceramics prepared under various sintering conditions that produce pure phase ceramics. The highest relative density is obtained with 10% excess Pb and sintered for 1150 °C/4hours .

Sintering Condition	Relative Density (%)
950 °C/4hrs stoichiometric	90
1050 °C/4hrs 5% Pb excess	95
1150 °C/4hrs 10% Pb excess	97

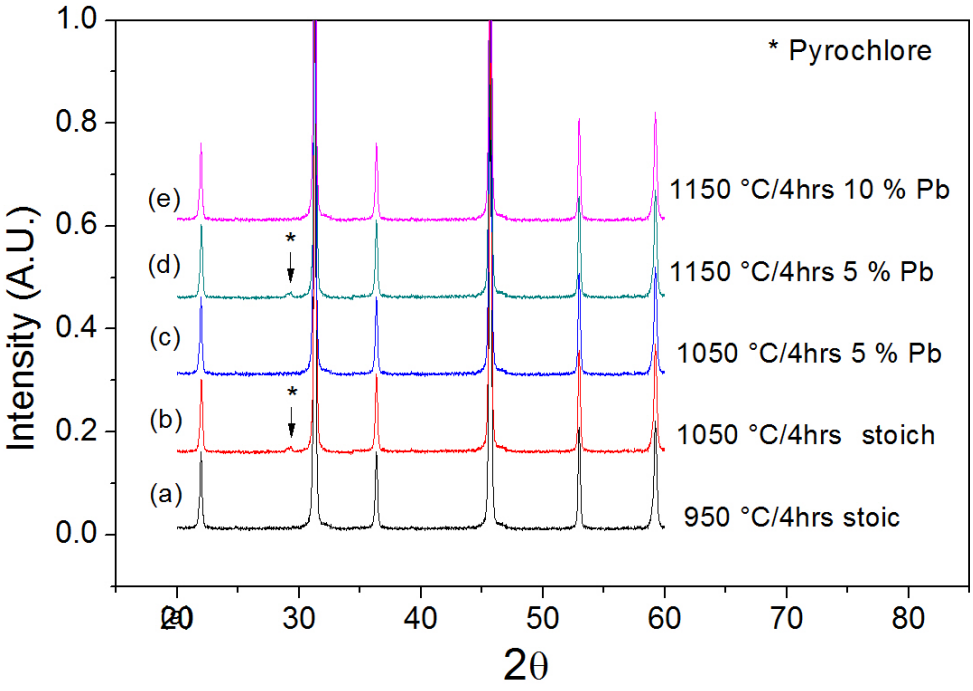

Figure 4.2: X-ray diffraction patterns for the 0.90PMN-0.10PT ceramics sintered at different temperatures and excess lead content. (a) at 950 °C/4hrs without excess Pb2+, (b) 1050 °C/4hrs without excess Pb^{2+}, (c) 1050 °C/4hrs with 5% excess Pb^{2+} (c) 1050 °C/4hrs with 5% excess Pb^{2+}, (d) 1150 °C/4hrs with 5% excess Pb^{2+}, (e) 1050 °C/4hrs with 10% excess Pb^{2+}.

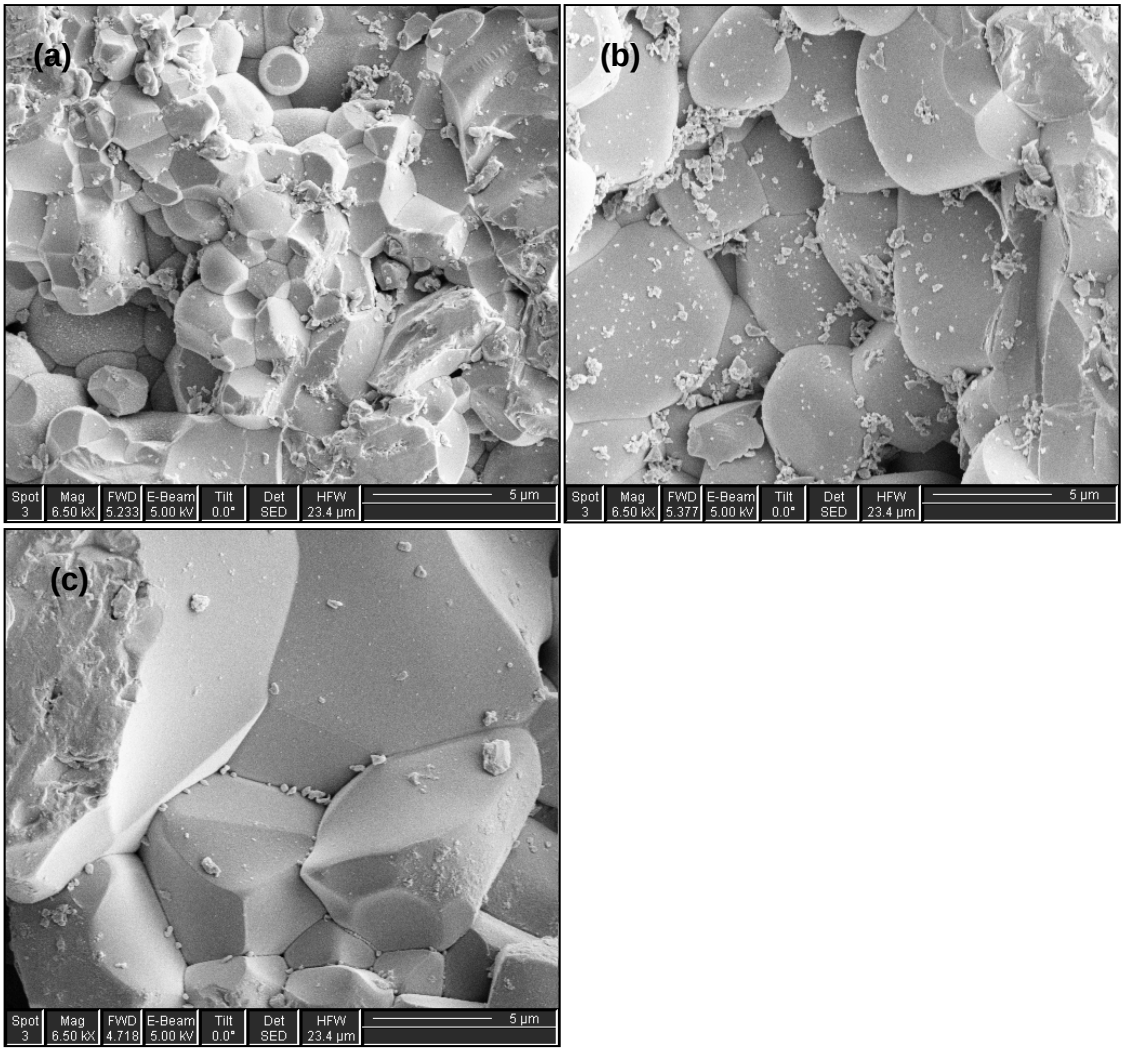

Figure 4.3: SEM images of the 0.90PMN-0.10PT ceramics sintered at different temperatures and excess lead content. (a) 950 °C/4hrs without excess $Pb(OAc)_2$, (b) 1050 °C/4hrs with 5% excess $Pb(OAc)_2$ and (c)1150 °C/4hrs with 10% excess $Pb(OAc)_2$.

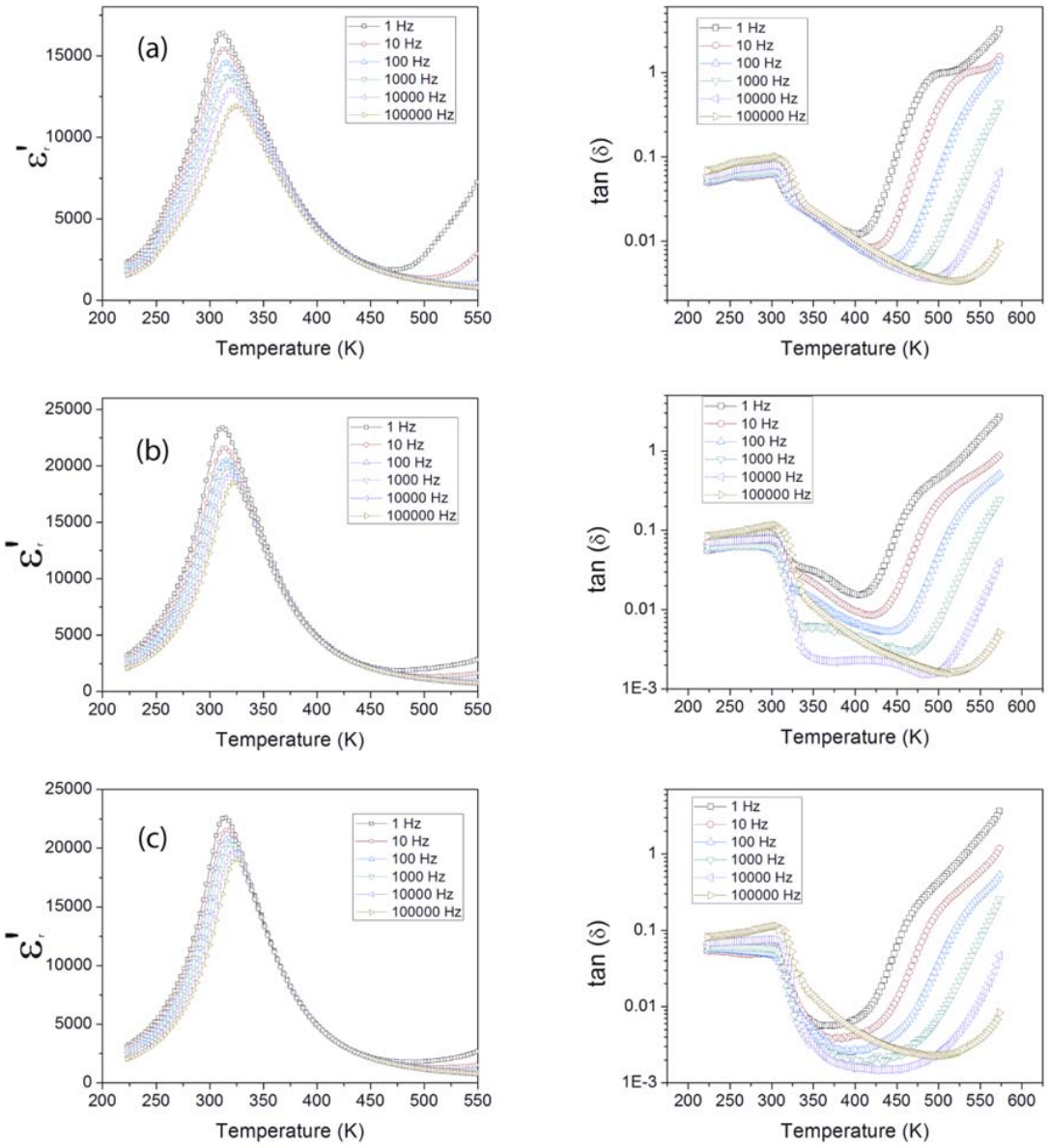

Figure 4.4: Dielectric constant and loss tangent for the 0.90PMN-0.10PT ceramic sintered at different sintering temperatures with various lead contents: (a) 950 °C/4hrs, stoichiometric, (b) 1050 °C/4hrs, 5% Pb, (c) 1150 °C/4hrs, 10% Pb.

4.4.2 Dielectric Properties:

Figure 4.4 shows the dielectric properties for 0.90PMN-0.10PT ceramics prepared under different sintering conditions that gave pure phase for each sintering condition: (a) 950 °C held for 4 hours with stoichiometric Pb^{2+} (abr. 950), (b) held 4 hours at 1050 °C

with 5% excess lead (abr. 1050) and (c) held 4 hours at 1150 °C with 10% excess lead (abr. 1150). All three samples exhibit similar variation in the $\varepsilon'(T)$ plots. They all show a diffuse, frequency dependent maximum of permittivity, with the temperature of maximum increasing with increasing measurement frequency, which is typical of relaxor behaviour. Comparing the dielectric permittivity of the 950 and 1050 samples, it can be seen that the latter exhibits a higher permittivity value at T_{max}, with ε'_{max} reaching ~ 20 000 at 1 kHz. The 1150 samples show almost the same value of ε'_{max} as the 1050 ones. The higher dielectric constant in the 1050 and 1150 ceramics can be attributed to their higher density compared to the 950 sample. Sintering temperatures of at least 1050 °C were required to obtain ceramics of adequate density. The 1050 sample shows the highest permittivity (ε') out of all three samples at 1 Hz, with 1150 having the next highest value.

By comparing the dielectric losses it is evident that although the 1050 and 1150 ceramics display a larger dielectric constant than the 950 ceramic, the 950 ceramics also exhibits higher losses than the 1050 and 1150 samples. The losses for all samples decrease with increasing density. The high frequency dielectric constant is the highest for the 1150 sample which also exhibits the lowest losses for all frequencies. The lowest loss and high permittivity confirms that the 1150 samples exhibit the best dielectric performance. The ceramics sintered at higher temperature would typically posses a larger average grain size and higher density. The larger permittivity values can attributed to the higher density, since a larger volume fraction of the ceramic will be crystalline perovskite. The higher density would also provide a lower proportion of grain boundaries in the ceramics which can be detrimental to the dielectric properties because they can allow for greater charge

dissipation and loss through defects and poorly crystallized material in the grain boundary. This shows that the higher sintering temperature improves the dielectric properties since permittivity at high frequencies will not have contributions arising from low density and instead will be dominated by contributions from usual relaxor polarization, thus having a lower degree of dielectric losses.

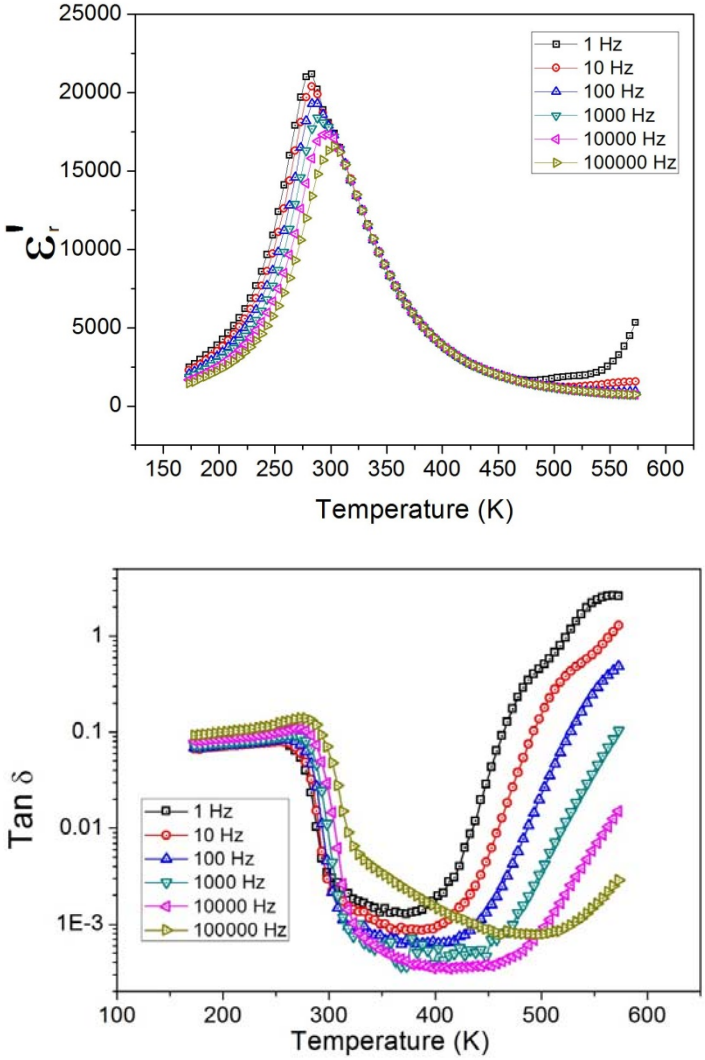

Figure 4.5: Dielectric constant (a) and loss tangent (b) for 0.93PMN-0.07PT ceramic sintered at 1150 °C for 4 hours and with 10% excess Pb^{2+}.

Figure 4.5 shows the dielectric constant as a function of temperature for the 0.93PMN-0.07PT ceramics, measured at various frequencies. The ceramic of this composition shows a large and diffuse maximum of dielectric constant (~ 20 000) and low loss tangent (*tan* δ) near room temperature. The dielectric properties are similar to the 0.90PMN-0.10 ceramics and show typical relaxor behaviour with a frequency dependent temperature of maximum permittivity which decreases with increasing measurement frequency.

Figure 4.6 shows a comparison of the two compositions studied (x = 0.07 and x = 0.10). The room temperature dielectric constants of these materials are much larger than currently used dielectric materials, $BaTiO_3$ (ε' = 1500), SiO_2 (ε' = 4). The ceramic of both compositions exhibit excellent dielectric properties with ε'_{max} > 20 000 measured at 1 Hz. Furthermore, the ceramic of composition x = 0.10 show the maximum dielectric constant measured low frequency (1 Hz) near room temperature making them excellent materials for use in high density capacitors. The x = 0.07 ceramics have their high frequency (100 kHz) permittivity reaching its maximum value at room temperature, which would be useful in high frequency applications such as in frequency filters in telecommunication.

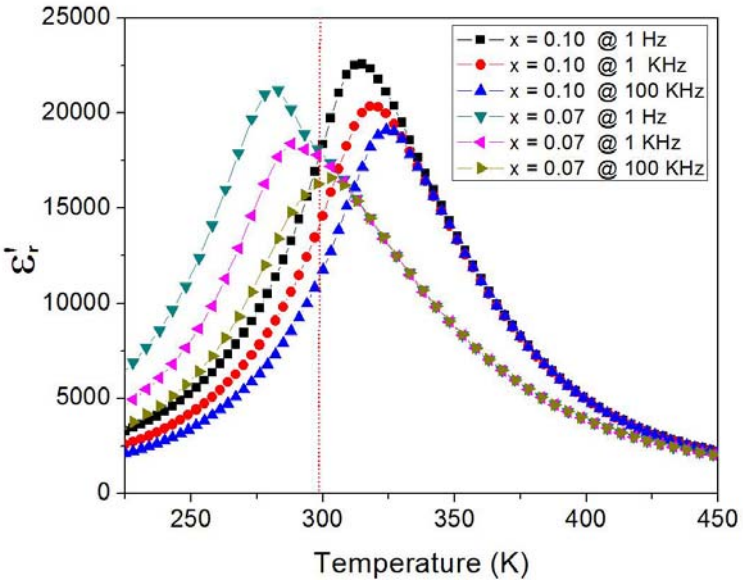

Figure 4.6: Comparison of temperature dependence of dielectric constant of the (1-*x*)PMN-*x*PT ceramics with *x* = 0.07 and 0.10 measured at various frequencies. The dotted line indicates room temperature.

4.4.3 Relaxor Ferroelectric Properties:

The temperature and frequency dependencies of the dielectric permittivity of the (1-*x*)PMN-*x*PT (*x* = 0.07 and 0.10) show typical relaxor ferroelectric behaviour. Detailed analysis of the relaxor behaviour is provided in this section to provide a better understanding of this fascinating phenomenon and properties. As mentioned in Chapter 1, high temperature slope of the permittivity peak can be characterized by Equation 4.1. Figure 4.7 shows the fitting of the dielectric properties as a function of temperature for the *x* = 0.07 and 0.10 ceramics to the quadratic law in Eq. 4.1 using a least squares method. Very good fitting results were obtained for both ceramics with a value of δ = 40.3 and 35.0 K, for *x* = 0.07 and 0.10, respectively. The delta parameter is a measure of the width of the permittivity peaks and is used as a measure of the diffuseness of the

permittivity peak. The smaller δ parameter indicates that the $x = 0.10$ ceramics have a sharper permittivity peak expected with a higher concentration of PT and ferroelectric behaviour [7, 18]. Furthermore this sharpening also manifests itself as an increase in the maximum of dielectric constant as can be seen in Figure 3.6. This follows the trend of a sharpening of the permittivity peak with an increase in PT content since the correlations and size of the PNR's would increase more at a larger temperature and with a larger concentration of the ferroelectrically active Ti^{4+} ions, which favours long-range polar order. [17-20].

The deviation at low temperature is due to the fact that Equation 4.1 is meant to describe the static, zero frequency contribution of the relaxor polarization, but high frequency data were used here for fitting to avoid any contribution from relaxation processes arising from grain boundary contributions discussed earlier. The deviation occurs because the permittivity at the measured frequency peaks at a higher temperature than the static permittivity ($\omega = 0$).

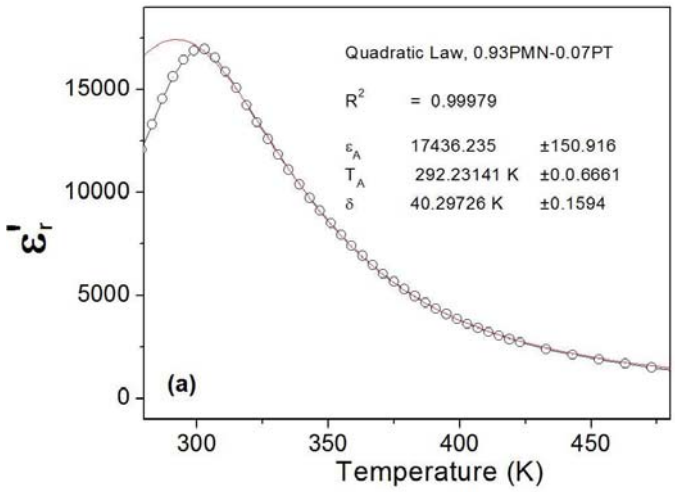

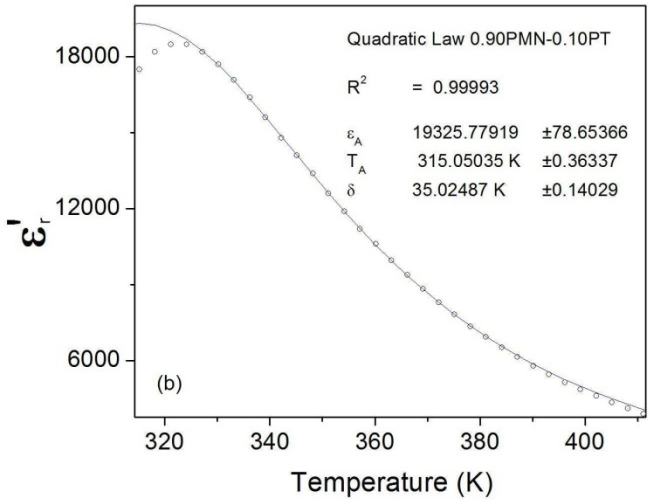

Figure 4.7: Fitting of the dielectric constant as a function of temperature measured at 100 kHz to the quadratic law described in Equation 4.1 for the 0.93PMN-0.07PT (a) and 0.90PMN-0.10PT (b) ceramics.

As described in Chapter 1, the frequency dependence of the temperature of maximum permittivity, $T_{max,}$ in relaxors can be described by the Vogel Fulcher law which provides some insights into the dynamics of dielectric relaxation of relaxors [5]:

$$\omega = \omega_O \exp\left(\frac{E_a}{(T_{\max} - T_f)}\right) \quad , \tag{4.2}$$

where E_a is the activation energy, ω_o is the Debye frequency and T_f is the freezing temperature which is very close to the depolarization temperature, T_d above which no macroscopic polarization can be formed with an applied field.

Figure 4.7 shows the fitting results of T_{max} of the 1150 sample to the Vogel Fulcher equation. From the fitting, a freezing temperature of 296 K and an E_a of 0.041 eV were obtained which are in good agreement with literature values for 0.90PMN-0.10PT ceramics prepared by conventional solid state reaction (0.0407 eV and 291 K) [5].

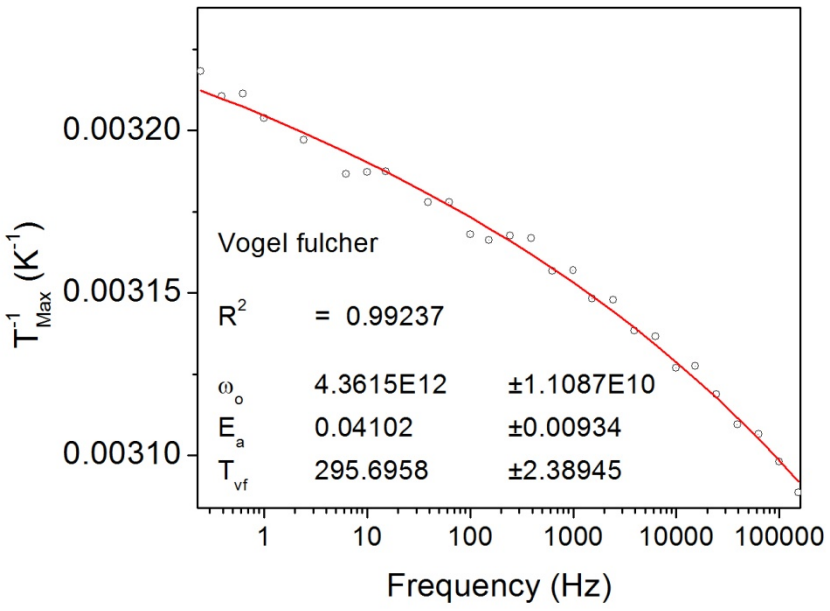

Figure 4.8: Vogel-Fulcher fitting for the x = 0.10 ceramic sintered at 1150 °C with 10% excess Pb^{2+} precursor.

In order to investigate the meaning of the freezing temperature in terms of macroscopically polar state, the polarization versus electric field, $P(E)$ relationship was measured as a function of temperature. From the $P(E)$ hysteresis loops (selected curves shown in Figure 4.9), the induced remnant polarization was extracted and its temperature

variation is plotted in Figure 4.10. It can be seen that upon cooling a macroscopic polarization is established at an onset temperature of about 290 K, which is close to the T_f deduced from the Vogel-Fulcher fitting of the dielectric properties. This lets us conclude that the freezing temperature from the Vogel-Fulcher fitting indicates a critical slowing down of the dynamics of the PNRs in relaxors leading to the onset of a macroscopic polarization under the application of an external electric field.

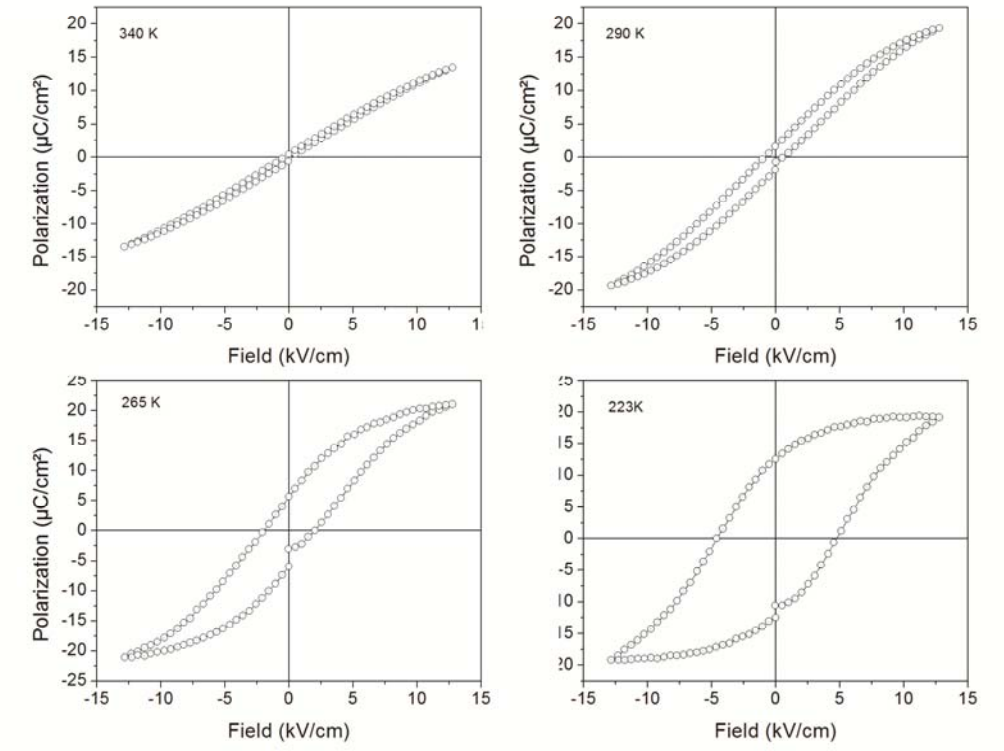

Figure 4.9: Polarization versus electric field curves of the ceramics sintered at 1150 °C and 10% Pb measured at various temperatures, showing linear behaviour at high temperature and an opening of the loop with decreasing measurement temperature.

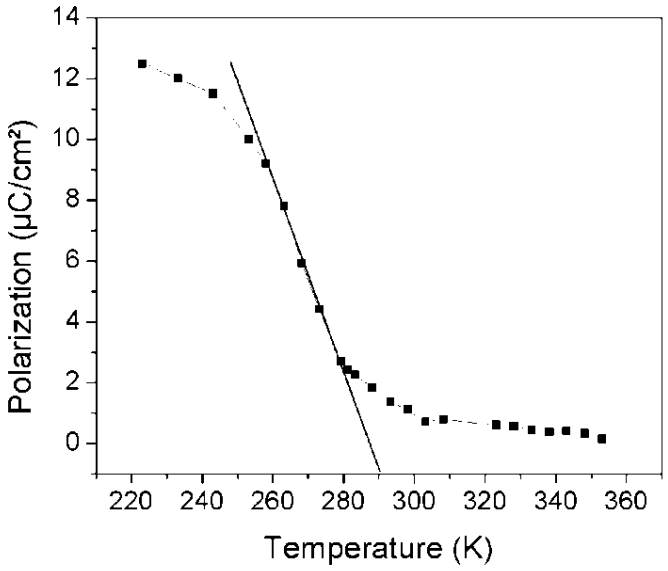

Figure 4.10: Remnant polarization versus temperature for the 0.90PMN-0.10 ceramic sintered at 1150°C/4 hours with 10% excess Pb.

4.5 Conclusion:

An ethylene glycol route has been developed to produce (1-*x*)PMN-*x*PT ceramics with low PT content (*x* = 0.07 and 0.10) in a one step heating process without the need for additional calcination before sintering. It was found that sintering at 1150 °C for 4 hours with an excess of 10% lead resulted in the best ceramics with a relative density as high as 97 %. This process prevents the formation of the pyrochlore phase. The ceramics sintered under these conditions showed the lowest loss and highest dielectric constant measured at high frequency. The ceramics with *x* = 0.10 exhibit their low frequency maximum of permittivity near room temperature at different frequencies, making ceramics produced by this method excellent candidates for use in the next generation of high performance ceramic capacitors for the reason that they are able to store large amounts of charge in small volumes with low leakage current. The ceramics

of x = 0.07 show their maximum of permittivity at high frequencies, making them suitable for use in high frequency capacitance applications such as frequency filters.

The ceramics show typical relaxor behaviour with a broad and diffuse peak in $\varepsilon'(T)$ plot, with the temperature maximum of permittivity increasing with increasing measurement frequency. The high temperature slope of $\varepsilon'(T)$ can be well described by the quadratic law in Equation 4.1, with the parameters δ and ε_A indicating the change in diffuseness and maximum of the permittivity peak.

The temperature dependencies of the dielectric permittivity satisfies the Vogel-Fulcher law from which a freezing temperature is determined. This freezing indicates a critical slowing down of the dynamics of PNRs in (1-x)PMN-xPT ceramics. A macroscopic polarization was found to be established below T_d, which is close to the freezing temperature T_f, indicating the onset of a long range polar state induced by an electric field.

References

[1] L. E. Cross., Relaxor ferroelectrics. *Ferroelectrics* vol 76*,* pp. 241-267, (1987).

[2] A. A. Bokov and Z-. G. Ye, "Recent progress in relaxor ferroelectrics with perovskite structure," *Journal of Materials Science,* vol. 41, pp. 31-52, (2006).

[3] Z-. G. Ye and A. A. Bokov, "Dielectric and structural properties of relaxor ferroelectrics," *Ferroelectrics,* vol. 302, pp. 473-477, (2004).

[4] Z-. G. Ye, Relaxor ferroelectric complex perovskites: Structure, properties and phase transitions. *Key Eng Materials*, vol 155 pp. 81-82 (1998).

[5] D. Viehland, S. J. Jang, L. E. Cross and M. Wuttig, "Freezing of the Polarization Fluctuations in Lead Magnesium Niobate Relaxors," *Journal of Applied Physics,* vol. 68, pp. 2916-2921, (1990).

[6] A. A. Bokov and Z-. G. Ye, "Universal relaxor polarization in $Pb(Mg_{1/3}Nb_{2/3})O_3$ and related materials," *Physical Review B,* vol. 66, pp 064103: 1-10 (2002).

[7] A. A. Bokov, Y. H. Bing, W. Chen, Z-. G. Ye, S. A. Bogatina, I. P. Raevski, S. I. Raevskaya and E. V. Sahkar, "Empirical scaling of the dielectric permittivity peak in relaxor ferroelectrics," *Physical Review B,* vol. 68, pp. 0521020:1-4, (2003).

[8] A. A. Bokov and Z-. G. Ye, "Phenomenological description of dielectric permittivity peak in relaxor ferroelectrics," *Solid State Communications,* vol. 116, pp. 105-108, (2000).

[9] S. L. Swartz and T. R. Shrout, "Fabrication of Perovskite Lead Magnesium Niobate," *Materials Research Bulletin,* vol. 17, pp. 1245-1250, (1982).

[10] K. Babooram, H. Tailor and Z-. G. Ye, "Phase formation and dielectric properties of $0.90Pb(Mg_{1/3}Nb_{2/3})O_3$-$0.10PbTiO_3$ ceramics prepared by a new sol-gel method," *Ceramics International,* vol. 30, pp. 1411-1417, 2004.

[11] K. Babooram and Z-. G. Ye, "Polyethylene glycol-based new solution route to relaxor ferroelectric $0.65Pb(Mg_{1/3}Nb_{2/3})O_3$-$0.35PbTiO_3$," *Chemistry of Materials,* vol. 16, pp. 5365-5371, (2004).

[12] M. P. Pechini, "Method of preparing lead and alkalina earth titanate and niobates and coating method using the same to form a capacitor, US Patent No. 3 330 697," (1967).

[13] A. B. Panda and P. Pramanik, "A novel solution-based method for the preparation of nanocrystalline single-phase $0.90Pb(Mg_{1/3}Nb_{2/3})O_3$-$0.10PbTiO_3$ powders," *Materials Letters,* vol. 56, pp. 435-440, (2002).

[14] R. Ubic and I. M. Reaney, "Structure and dielectric properties of lead pyrochlores," *Journal of the American Ceramic Society,* vol. 85, pp. 2472-2478, (2002).

[15] H. Beltran, N. Maso, B. Julian, E. Cordoncillo, J. B. Carda, P. Escribano and A. R. West, "Preparation and characterization of compositions based on PbO-MgO-Nb_2O_5 using the sol-gel method," *Journal of Sol-Gel Science and Technology,* vol. 26, pp. 1061-1065, (2003).

[16] R. J. Cava, W. F. Peck and J. J. Krajewski, "Pyrochlore based oxides with high dielectric constant and low temperature coefficient," *Journal of Applied Physics,* vol. 78, pp. 7231-7233, (1995).

[17] Z-. G. Ye, Y. Bing, J. Gao, A. A. Bokov, P. Stephens, B. Noheda and G. Shirane, "Development of ferroelectric order in relaxor (1-x)$Pb(Mg_{1/3}Nb_{2/3})O_3$-x$PbTiO_3$ (0 <= x <= 0.15)," *Physical Review B,* vol. 67, pp. 104104: 1-8, (2003).

[18] O. Bidault, E. Husson and P. Gaucher, "Study of the electric field-induced low temperature phase in $Pb(Mg_{1/3}Nb_{2/3})O_3$: Titanium influence," *Journal of Physique III France,* vol. 7, pp. 1163-1172, (1997).

[19] C. Lei, A. A. Bokov and Z-. G. Ye, "Ferroelectric to relaxor crossover and dielectric phase diagram in the $BaTiO_3$-$BaSnO_3$ system," *Journal of Applied Physics,* vol. 101, pp. 084105:1-9, (2007)

[20] G. A. Samara and E. L. Venturini.. Ferroelectric/relaxor crossover in compositionally disordered perovskites. *Phase Transit,* vol 79, pp. 21-40. (2006)

CHAPTER 5:

SYNTHESIS AND THE DIELCTRIC CHARACTERIZATION OF A NEW RELAXOR SOLID SOLUTION OF $(1\text{-}x)Pb(Mg_{1/3}Nb_{2/3})O_3\text{-}xBi(Zn_{1/2}Ti_{1/2})O_3$

5.1 Abstract

Ceramics of a new binary solid solution $(1\text{-}x)Pb(Mg_{1/3}Nb_{2/3})O_3\text{-}xBi(Zn_{1/2}Ti_{1/2})O_3$ [$(1\text{-}x)$PMN-xBZT] have been prepared (with x = 0.05-0.30) and examined by X-ray diffraction and dielectric spectroscopy to investigate the structure and the relaxor ferroelectric properties. It is found that the upper limit of thermal stability for the perovskite phase decreases with increasing x, and the structure remains pseudocubic (or rhombohedral) with constant lattice parameter up to the solubility limit of x = 0.275. All the compositions studied show a broad and diffuse peak in the temperature dependence of dielectric permittivity $\varepsilon(T)$, the temperature of which increases with increasing measurement frequency, indicating typical relaxor behaviour. All the samples measured were found to follow an empirical quadratic law that describes the high temperature slope of the permittivity ($> T_{max}$). The diffuseness of the permittivity peak was found to increase linearly with the increasing amount of BZT.

Furthermore, analysis of the dielectric behaviour shows that it consists of the same types of contributions as the prototypical relaxor $Pb(Mg_{1/3}Nb_{2/3})O_3$. One contribution to the permittivity; the χ^*_{CR}, can be described by the Kohlrausch-Williams-Watts law (KWW), $P \propto \exp[-(t/\tau)^{\beta}]$. It was found that the β and τ parameters used to describe this contribution both follow the Vogel-Fulcher law with the freezing temperature, T_f decreasing with increasing BZT content. The change in diffuseness and freezing

temperature can be attributed to the increase in chemical disorder because the addition of BZT end member introduces two more heterovalent cations (Zn^{2+} and Ti^{4+}) on the perovskite octahedral B-site and the Bi^{3+} cation on the perovskite A site of PMN.

5.2 Introduction:

Relaxor ferroelectric-based materials have received much attention in fundamental science as well as for materials research for their excellent dielectric and electromechanical properties which include a high dielectric permittivity and large electrostrictive and piezoelectric coefficients, making them excellent materials for electromechanical actuators, transducers and sensors [1, 2]. Particular interest has been put on solid solutions between end members of rhombohedral and tetragonal ferroelectric symmetry because some of the best pyroelectric, piezoelectric and electro-optic properties have been found close to the rhombohedral side of the morphotropic phase boundary (MPB) in single crystals [3, 4].

The high dielectric permittivity is one of the important parameters contributing to the excellent electromechanical properties in these systems. An important class of relaxors belong to complex perovskites of the formula $(A'_{(1-x)}A''_{x})(B'_{(1-y)}B''_{y})O_3$ with two or more heterovalent ions occupying a crystallographically equivalent site.

Recently, a new perovskite compound, $Bi(Zn_{1/2}Ti_{1/2})O_3$ (BZT) has been synthesized under high pressure and found to have exceptionally high tetragonality and polarization [5]. Although the compound itself cannot be synthesized under ambient conditions, it has shown to be able form solid solutions with lead based perovskites such as $PbTiO_3$[6, 7]. However, to date, no work has been reported on the investigation of the

solid solutions containing the tetragonal BZT and rhombohedral/cubic end member, such as the relaxor ferroelectric $Pb(Mg_{1/3}Nb_{2/3})O_3$ (PMN). Investigation into such systems are of great interest because they may be analogous to other systems such as (1-*x*)$Pb(Mg_{1/3}Nb_{2/3})O_3$-*x*$PbTiO_3$ and (1-*x*)$Pb(Zn_{1/3}Nb_{2/3})O_3$-*x*$PbTiO_3$ which show exceptional properties near their respective MPBs[8]. Moreover, a new solid solution such as (1-*x*)PMN-*x*BZT will provide a unique system to investigate the structure and relaxor ferroelectric property relationship.

The temperature and frequency dependencies of the dielectric permittivity of relaxor ferroelectrics are reminiscent of those observed in dipolar glasses. In particular, a broad maximum of the real part of the permittivity (ε') is observed, and the temperature of the maximum permittivity, T_{max}, increases with increasing measurement frequency. Although the mechanism of this behaviour is still under intensive investigation, it is qualitatively related to the relaxation of dipoles arising from compositional inhomogeneity. Due to the compositional disorder, long range polar ordering is prevented polar nanoregions (PNRs) form instead of macroscopic domains that occur in normal ferroelectrics [2, 9]. It is supposed that at high enough temperatures the dipolar moments of PNRs change in direction due to thermal motion. Upon cooling the PNR's begin to increase in number and size, causing the permittivity to increase. Simultaneously, upon cooling the PNR dynamics continuously slow, until at some point, the moments can no longer keep up with the oscillating measuring voltage, leading to a maximum of dielectric permittivity with different T_{max} for each frequency. Unlike normal ferroelectrics, whose high temperature slope of the permittivity follows the Curie-Weiss law above the respective T_C, relaxors only obey the Curie-Weiss law at temperatures well above the

temperature of maximum permittivity [10]. Recently the variation of the permittivity in relaxors at T> T_{max} are found to follow an empirical formula that describes a quadratic [11, 12].

$$\frac{\varepsilon_A}{\varepsilon'} = 1 + \frac{(T - T_A)^2}{2\delta^2} \quad , \tag{5.1}$$

where ε_A and T_A define the permittivity peak position of the fitting curve and δ describes the diffuseness of the peak shape. This so called "quadratic law" has been applied to describe the diffuseness of the permittivity peak in many relaxor ferroelectrics and their solid solutions.

According to the soft polar nanoregion model described in Section 1.4, PNRs are comprised of two different types of dipole moments. (i) those that are fixed due to a dominance of one type of interaction and, (ii) those that are free to fluctuate due to frustration between different interactions. Previous work from our laboratory has shown that that the dielectric behaviour of the prototypical relaxor $Pb(Mg_{1/3}Nb_{2/3})O_3$ contains several contributions to its permittivity [13]:

$$\varepsilon^*(f,T) = \chi_U^*(f,T) + \chi_{CR}^*(f,T) + \varepsilon_\infty(T) \quad , \tag{5.2}$$

where χ_{CR}^* contribution comes from the polarization of the fixed cells, called the conventional relaxor susceptibility, and χ_U^* called the universal relaxor susceptibility is the contribution arising from the free cells. It was found that the χ_{CR}^* contribution could be fitted to the Kohlrausch-Williams-Watts law (KWW):

$$P \propto \exp[-(t/\tau)^{\beta}] \quad , \tag{5.3}$$

which describes the change in polarization in the time domain. However in order to express this relationship in the frequency domain, the Fourier transform of the derivative of the KWW function must be taken, so that one has:

$$\chi^{*}_{KWW}(f) = \chi_{KWW0}\beta\tau^{-\beta}\int_0^{\infty} t^{\beta-1}\exp\left[-\left(\frac{t}{\tau}\right)^{\beta} - i2\pi ft\right]dt, \qquad (5.4)$$

where, χ_{KWW0} is the susceptibilty at zero frequency, τ indicates the relaxation time and β describes the shape of the imaginary permittivity peak in the frequency domain.

Relaxations in highly disordered system, such as relaxors, do not follow the classical Arrhenius temperature, behaviour of freezing at 0 K. Instead, on cooling the relaxation time (τ) often diverges to infinity at a nonzero temperature, T_f, which can be considered as the freezing temperature below which the system becomes non-ergodic. Ergodic implies that over a long time average, there is an equal probability for the polarizations to be in any state. In the non-ergodic state, the polarization is frozen and is only likely to be in one state out of all those that are possible. The temperature dependence of τ at $T > T_f$ can be described by the Vogel-Fulcher Law (V-F) [10, 13, 14],

$$\tau = \tau_0 \exp[E_\tau /(T - T_f)] \quad , \qquad (5.5)$$

where τ_o and E_τ are the fitting parameters.

It was found that the β and τ parameters used to describe the KWW relaxation in PMN both follow the V-F law [13]:

$$\tau = \tau_0 \exp[E_\tau /(T - T_f)] \quad , \qquad (5.6)$$

$$\beta = \beta_0 \exp[E_\beta /(T - T_\beta)] \quad , \qquad (5.7)$$

and decrease simultaneously towards zero at the same value for T_f and T_β (i.e. 210 K) indicating a unique simultaneous freezing phenomenon.

In this work, a new solid solution of (1-x)Pb($Mg_{1/3}Nb_{2/3}$)O_3-xBi($Zn_{1/2}Ti_{1/2}$)O_3 has been prepared and its structure, limit of solubility and dielectric properties characterized. This system is found to exhibit typical relaxor behaviour, with the same types of contributions to its permittivity as in PMN. The temperature dependence of the permittivity is found to satisfy the quadratic law described in Equation 5.1, which describes the diffuseness of the permittivity peak as a function of composition. The temperature and frequency dependencies of the conventional relaxor polarization are fit to the KWW law, in order to investigate the temperature dependencies of the parameters τ and β.

5.3 Experimental

The ceramics of (1-x)Pb($Mg_{1/3}Nb_{2/3}$)O_3-xBi($Zn_{1/2}Ti_{1/2}$)O_3 [(1-x)PMN-xBZT] were prepared using the constituent oxides as is in solid state reaction to produce compositions of x = 0.05 - 0.30. The powders were synthesized by the two step columbite method [15] in which MgO (99.95 % Alfa Aesar) and Nb_2O_5 (99.9 % Alfa Aesar) were first reacted to form the $MgNb_2O_6$ columbite phase which was then reacted with the other oxides to form the perovskite phase. In the first step a stoichiometric amount of Nb_2O_5 and a 3% mole excess of MgO powders were mixed together, ball milled in acetone for 12 hours, pressed uniaxially into a single pellet and then calcined at 1100 °C for 4 hours in a muffle furnace. The pellet was then pulverized in an agate mortar and pestle and re-milled using a ball mill (ZrO_2 balls, 3mm diameter) for 24 hours. In the second step, a stoichiometric amount of the $MgNb_2O_6$ powder was then mixed with stoichiometric amounts of ZnO (99.9% Koujundo Chemicals), TiO_2 (99.5 % Alfa Aesar), Bi_2O_3 (99.9 % Alfa Aesar) and

PbO (99.9 Alfa Aesar). The mixture was ball milled before being pressed into a single pellet for calcination at 850°C for 4 hrs. The calcined pellet was then reground, ball milled for 24 hrs and pressed uniaxially into 10mm diameter ceramics discs for sintering. In order to prevent the evaporation of PbO and Bi_2O_3 the pressed pellets were placed in a bed of sacrificial (1-*x*)PMN-*x*BZT powder (of the same composition) covering the pellets during sintering process that took place at various temperatures between 1000 and 1100 °C to form ceramics. The sintered ceramics were polished using silicon carbide sand paper (220, 400, 600 grit) to produce two parallel and flat surfaces and rinsed in acetone using a sonicator. The polished surfaces were used to analyze phase formation by X-ray powder diffraction. The diffraction data was measured using Cu K_α radiation, (42 mA, 45 kV Rigaku Rapid-Axis Diffractometer, step size = 0.02 °/step, collection time = 2 minutes, 2θ = 10 ° - 80 °) to confirm the formation of pure perovskite phase.

Gold electrodes were sputtered (Anatech Hummer 6.2, 10 min, 15 mA plasma discharge current) on the polished surfaces of the ceramics for electrical characterization. Gold wire was used to connect the ceramic electrodes to the dielectric analyzer probes using colloidal silver paste. The temperature dependence of the dielectric permittivity was measured at various frequencies using a Novocontrol Alpha high resolution broadband dielectric analyzer. The measurements were taken isothermally every 3 °C, from 300 °C to -100 °C. A least squares fitting method described in reference [13] was used to fit the experimental data to the KWW function.

5.4 Phase Formation and Thermal Stability

Figure 1 shows the X-ray diffraction patterns for the (1-*x*)PMN-*x*BZT ceramics of *x* = 0.05, 0.10, 0.15, 0.20, 0.25, 0.275 and 0.30, sintered at different temperatures. In order to form pure perovskite phase, the sintering temperature had to be decreased by approximately 50 °C for every 10 mol% of BZT added above *x* = 0.10, so that a sintering temperature of 1200 °C was used for *x* < 0.10 and it was decreased to 950 °C for *x* = 0.275. It can be seen that the solubility limit of the perovskite phase was reached at *x* = 0.275. Diffraction patterns of ceramics prepared with a nominal stoichiometry above *x* = 0.275 showed a peaks corresponding to a undesirable pyrochlore phase. Several methods and conditions were tried in order to produce pure perovskite phase for *x* = 0.30, such as using lower synthetic temperatures and regrinding before multiple calcinations, but none was successful as the pyrochlore phase subsisted with these conditions.

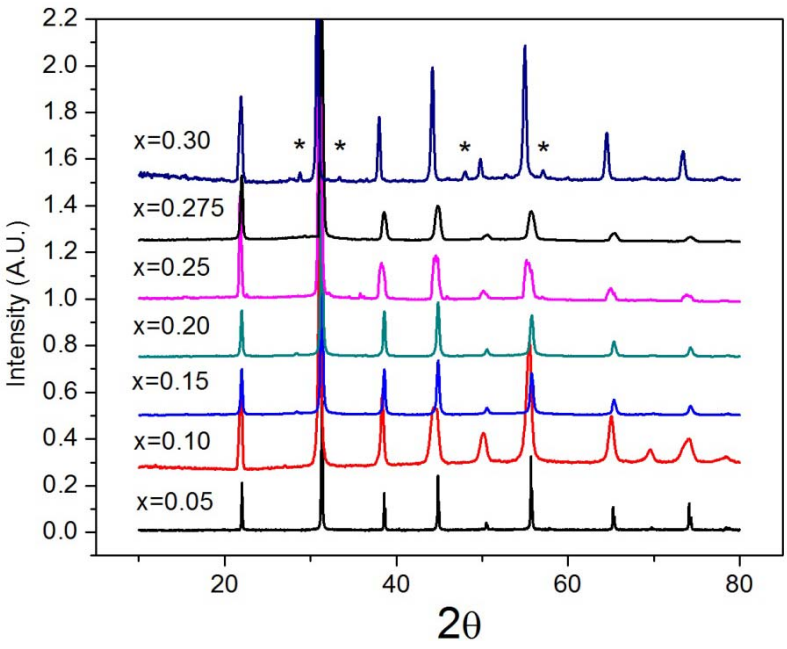

Figure 5.1 X-ray diffraction patterns of the (1-*x*)PMN-*x*BZT (*x* = 0.05-0.30) ceramics prepared at various sintering temperatures. Stars indicate the peaks of a pyrochlore phase in the ceramics of *x* = 0.30.

The XRD patterns of the solid solution ceramics in Fig. 5.1 suggest that a rhombohedral or pseudocubic phase persists with increasing concentration of the tetragonal (P4mm) BZT end member. Figure 5.2 shows the dependence of the pseudo-cubic lattice parameters on the BZT content, which shows no significant change. This differs from the trend seen in the solid solution between BZT and $PbTiO_3$ (PT), where the addition of the tetragonal end member (PT) increases the tetragonality, *c*/*a* lattice constant ratio in the structure. The solubility of the tetragonal end member BZT into the rhombohedral/pseudocubic PMN is such that the morphotropic phase boundary and tetragonal phase would form at compositions that are greater than that of the solubility limit [5]. Even in the (1-*x*)PMN-*x*PT system, the addition of PT does not lead to a tetragonal structure until $x > x_{MPB} = 0.35$, while a smaller x results in a rhombohedral structure first at $x > 0.05$ [16, 17]. Furthermore the absence of the morphotropic phase boundary may not occur within the limits of solubility because of the presence of the non-ferroactive Mg^{2+} ion. It has been shown by Suchomel et al.[7] that in order to enhance tetragonality in bismuth based systems, the B-site sublattice must be fully populated by a combination of fully ferroelectric active cations. The high degree of ionic bonding for the Mg^{2+} ion along with its larger cationic radius ($r_{Mg2+} = 0.72$ Å, $r_{Ti4+} = 0.605$ Å) prefers non polar formation. This is because those ions with large cationic radius and higher ionicity prefer symmetric bonding by equalizing electrostatic interactions. The ions that allow for ferroelectric distortions have to meet the requirement that they have small radii, lower ionicity and higher covalency in their bonding [18]. The ions with these properties can tolerate more ferrodistortive displacement because of the larger space in coordination sphere as well as from greater orbital overlap which can create a bigger non-centric

displacement, thus producing distortions away from the ideal cubic perovskite structure. The trend of the relatively constant lattice parameters has also been seen in the case of solid solutions containing non ferroactive ions with PT, such as $Bi(Mg_{1/2}Ti_{1/2})O_3$ and in which the lattice parameters remain relatively constant, preserving the degree of tetragonality in the systems[7].

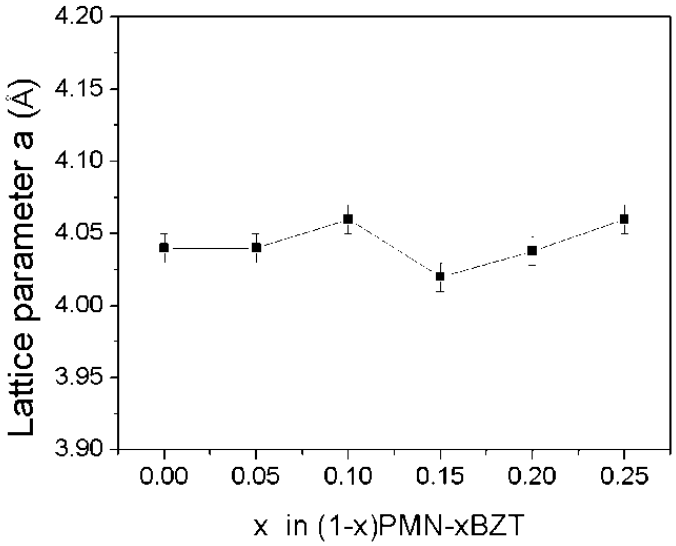

Figure 5.2: The variation of the pseudo-cubic lattice parameter (*a*) as a function of BZT content for the (1-*x*)PMN-*x*BZT solid solution.

5.5 Dielectric Properties

The dielectric properties (real permittivity ε', and loss tangent, $tan\delta$) measured as a function of temperature at various frequencies are shown in Figure 5.3. All the solid solution ceramics show typical relaxor-type characteristics in their $\varepsilon'(T)$ plots: a broad maximum of permittivity with strong frequency dispersion at the low temperature slope of the peak, and more importantly, the temperatures of the permittivity peaks (T_{max})

increases with increasing frequency. The difference in T_{max} at different frequencies:ΔT_{max} = [T_{max} (100 kHz) - T_{max} (10 Hz)] can be used to measure the degree of dispersion in relaxors [19]. Figure 5.4 shows the variation of ΔT_{max} as a function of composition. The increase in ΔT_{max} with increasing BZT content corresponds to an increase in frequency dispersion of permittivity, indicating an enhanced relaxor behaviour.

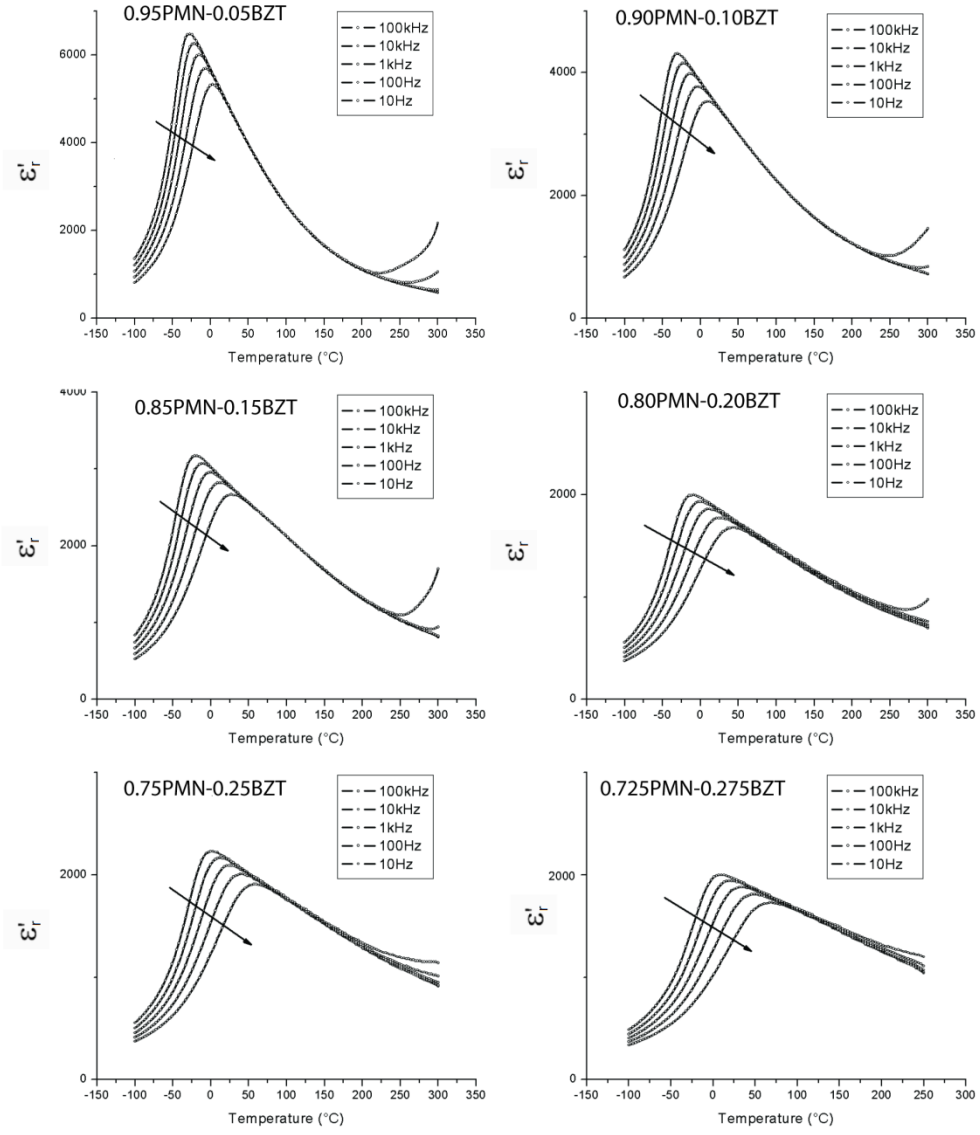

Figure 5.3: Variation of the dielectric constant as a function of temperature and frequency of the (1-*x*)PMN-*x*BZT solid solution showing typical relaxor dispersion. The arrows indicate increasing measurement frequency.

It is known that the temperature variation of the permittivity on the high temperature side of the maximum, which is dominated by contributions from the static limit of the conventional relaxor polarization (the contribution from the flipping of the fixed cells in the PNRs), can be described by a Lorentz-type function shown in Equation (5.1). This quadratic function was used to fit the high temperature slope of the ε'(*T*) plots measured at 100 kHz. The fitting of the dielectric spectra was performed using a least squares method with dielectric data measured at 100 kHz in order to avoid contributions from non-relaxor related components such as low frequency dispersion coming from mobile charge carriers. These charge carriers contribute to the overall permittivity at high temperatures and low measurement frequencies, but are not related to intrinsic relaxor dielectric response.

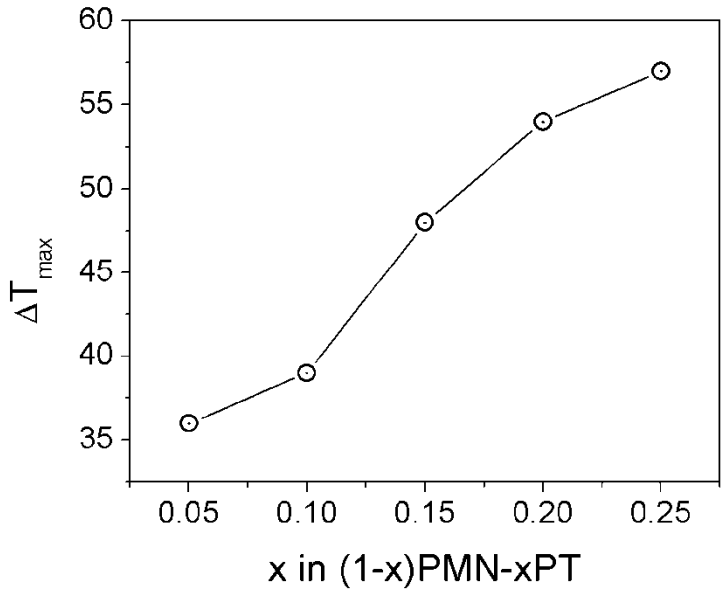

Figure 5.4: Variation of the ΔT_{max} = [T_{max}(100 KHz) - T_{max}(10 Hz)] as a function of composition in the (1-*x*)PMN-*x*BZT solid solution showing an increase with increasing BZT content

Figure 5.5 shows the graphical fitting results of the dielectric permittivity of the (1-x)PMN-xBZT ceramics to the quadratic law described Equation 5.1. Each of the samples measured shows a good fit over a large temperature range, consistent with the behaviour found in other relaxor ferroelectrics [10, 11, 19]. Deviations from the quadratic relationship occur on the low temperature sides of the permittivity peak. The deviation is from the conventional relaxor dispersion (CRD). Since the quadratic law models the static permittivity contribution of the CRD, the dispersion that occurs at high frequencies used for fitting causes the measured maxima to occur at a lower temperature than the maximum of the fitting curve. Table 5.1 shows the parameters obtained by fitting the $\varepsilon'(T)$ curves to Equation 5.1. The ε_A and T_A parameters both decrease with increasing BZT content from x = 0.05 to 0.20. This trend is consistent with the dielectric behaviour of the solid solution, in which the value of the maximum permittivity decreases with increasing BZT content. The deviation from this trend for the x = 0.25 ceramic can be explained by the fact that to obtain a reasonable fitting to a Lorentzian peak in shape, a fitting range must be larger than the δ parameter. This requirement is necessary to provide a sufficient ratio of fitted data to peak size in order to obtain adequate statistics to accurately describe the shape of the curve.

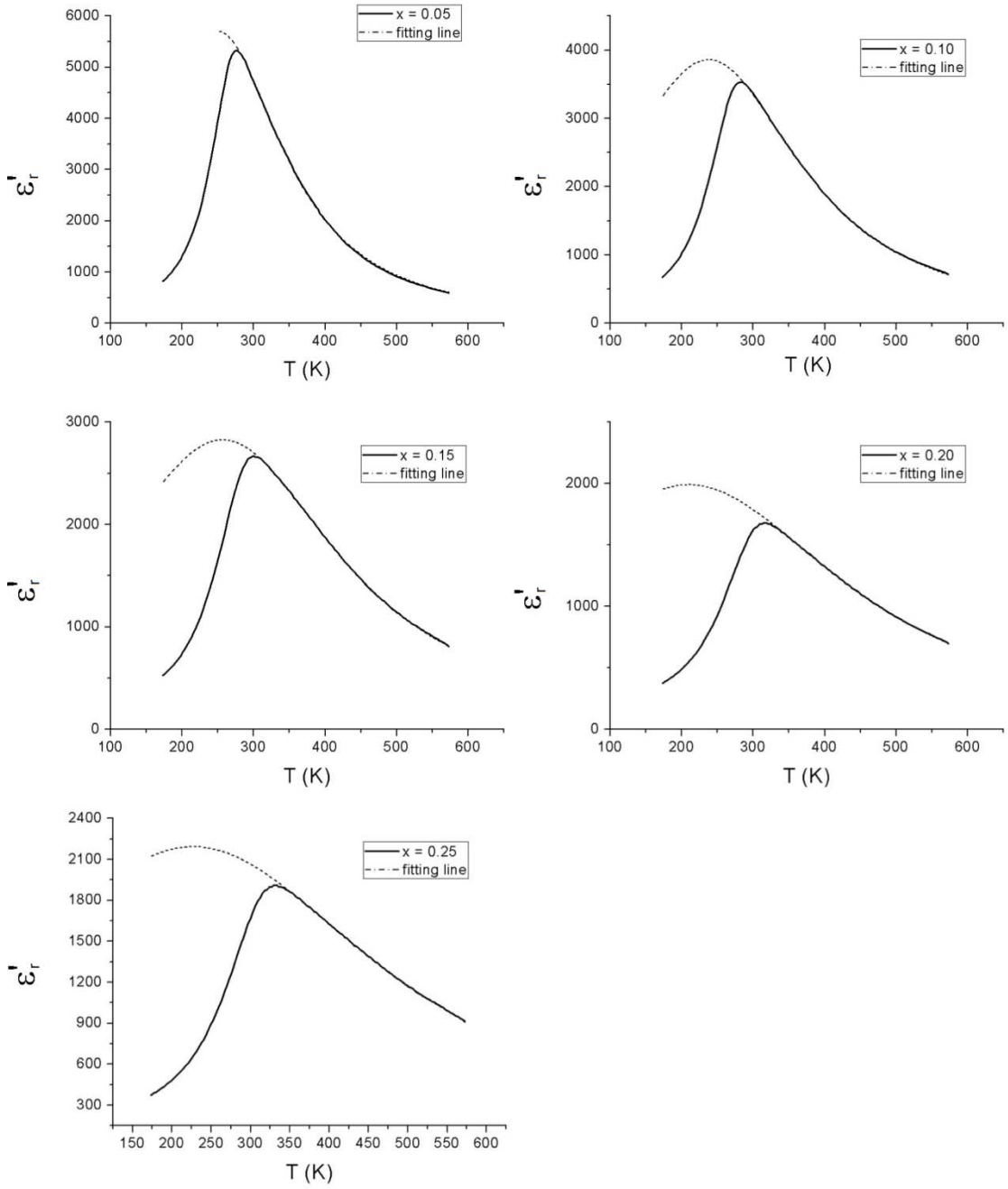

Figure 5.5: Fitting of the dielectric peaks of the (1-*x*)PMN-*x*BZT ceramics measured at 100 KHz to Equation 1. Deviations at low temperatures come from conventional relaxor dispersion.

Table 5.1: Parameters obtained from fitting dielectric data of the (1-*x*)PMN-*x*BZT ceramics to Equation 5.2

Composition	ε_A	T_A (K)	δ (K)
x = 0.05	5681 ± 25	250 ± 1	78.8 ± 0.2
x = 0.10	3856 ± 21	237 ± 1	113.0 ± 0.2
x = 0.15	3180 ± 20	218 ± 3	153.0 ± 1.0
x = 0.20	1991 ± 19	209 ± 3	189.1 ± 0.5
x = 0.25	2193 ± 21	206 ± 1	207.1 ± 1.4

Figure 5.6 shows the variation of the δ parameter as a function of BZT content. The δ parameter, which can be used as a measure of the diffuseness of the permittivity peak, varies linearly with the BZT content. The increase in diffuseness can be related to the increase in chemical disorder because the addition of the BZT end member introduces two more heterovalent cations (Zn^{2+}/Ti^{4+}) on the perovskite octahedral B-site and the Bi^{3+} cation on the perovskite A-site. The degree of diffuseness of the permittivity peak is generally associated with the degree of disorder in the cationic matrix [20, 21]. Moreover, the parameters that describe the relaxor properties (ΔT_{max}, δ) indicate that the relaxation behaviour is in fact enhanced with BZT content, which is opposite to the trend in the (1-*x*)PMN-*x*PT solid solution system, in which the addition of PT into PMN decreases the degree of dispersion. Instead, the addition of BZT to the canonical relaxor, PMN, creates a solid solution that exhibits a greater degree of relaxor-like behaviour up to the solubility limit of x = 0.275.

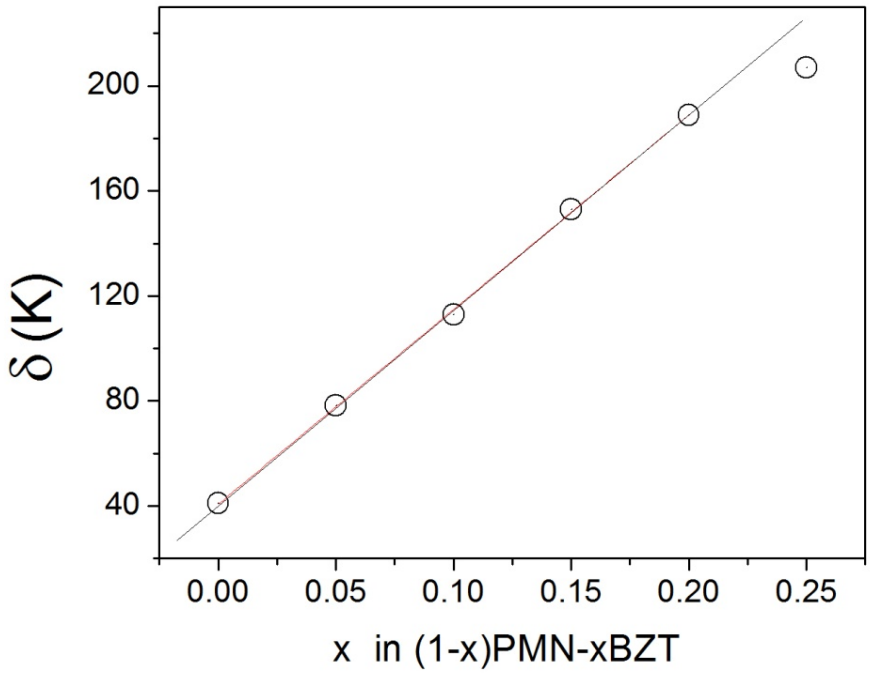

Figure 5.6: Variation of the δ diffuseness parameter in Equation 1 as a function of composition in the (1-*x*)PMN-*x*BZT solid solution showing a linear increase with increasing BZT content.

Figure 5.7 shows the real (ε') and imaginary (ε'') permittivity spectra in the frequency domain for the (1-*x*)PMN-*x*BZT ceramics with $x = 0.10$ and 0.15, measured at various temperatures. The ε'' peaks broaden and shift to lower frequencies with decreasing measurement temperature. With decreasing measurement temperature the drop in the real permittivity occurs over a larger interval and moves to lower frequency. The ε' and ε'' spectra could be fit to the KWW function, where the parameters, β and τ describe the width of the loss peak and the position in the frequency domain, respectively.

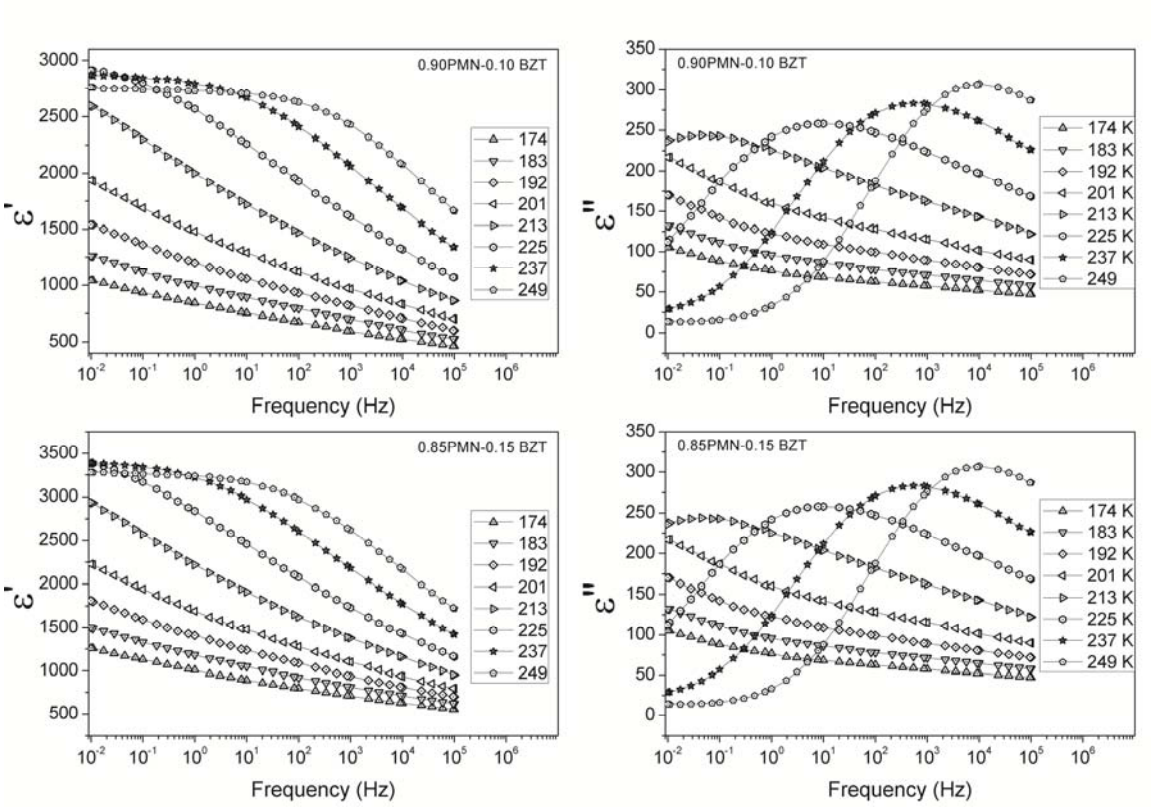

Figure 5.7: Real (ε') and imaginary (ε'') dielectric spectra of the (1-*x*)PMN-*x*BZT ceramics with *x* = 0.10 and 0.15 measured at various temperatures.

Figure 5.8 shows the variation of the relaxation frequency (f_{KWW}), which is the inverse of the relaxation time ($f_{KWW} = \tau^{-1}$), as a function of temperature for the (1-*x*)PMN-*x*BZT ceramics with *x* = 0.10 and 0.15. Expressing the relaxation time in terms of frequency is necessary in order to be able to extrapolate data from the Vogel-Fulcher analysis which will be described later on. Both parameters, β and f_{KWW} decrease in value with decreasing measurement temperature. The decrease of the f_{KWW} parameter signifies that the relaxation time for this process is increasing, indicating a slowing down in the dynamics of this polarization contribution. This is further supported by the β parameter decreasing, corresponding to a broadening of the peak in the imaginary permittivity.

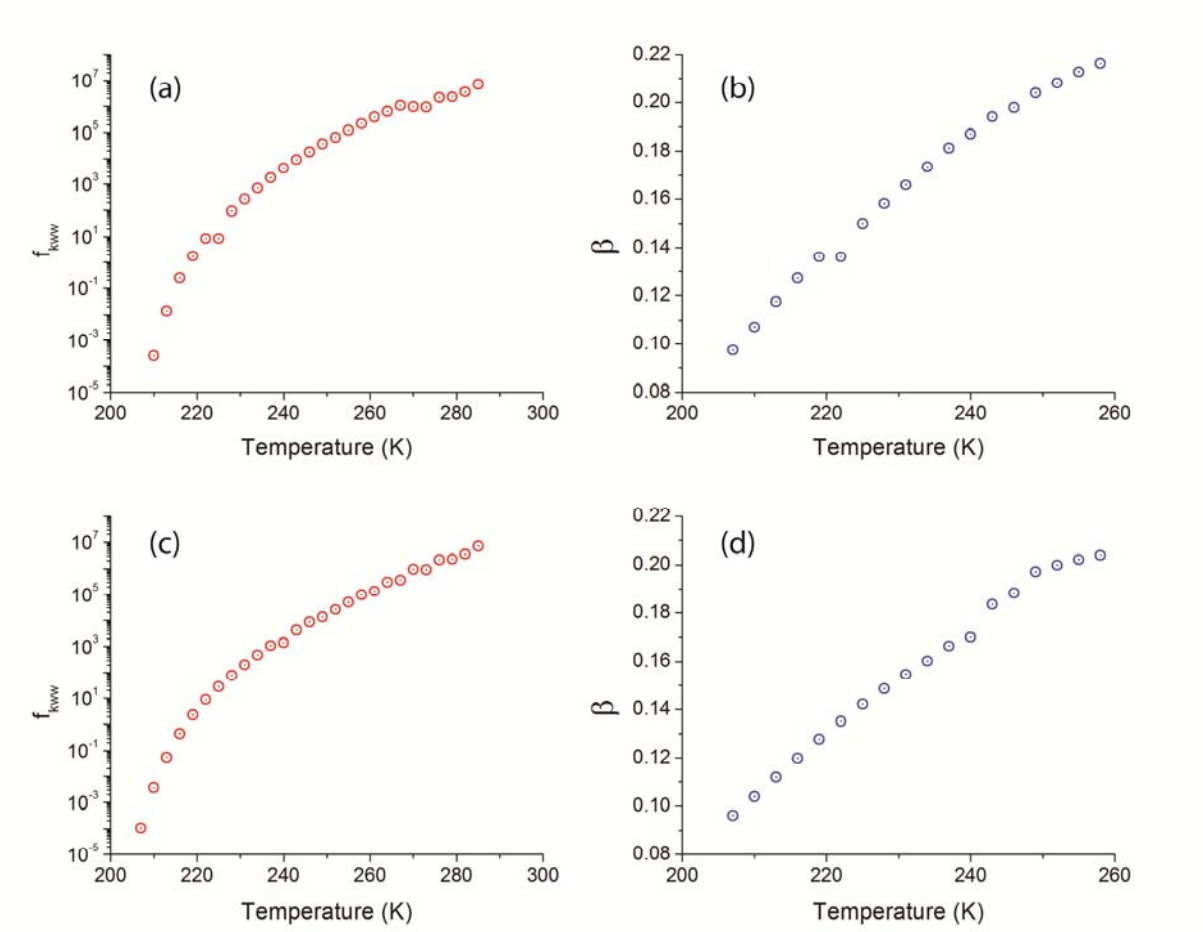

Figure 5.8: The variation of the KWW fitting parameters, f_{KWW} and β obtained from fitting dielectric spectra obtained at different temperatures for the (1-*x*)PMN-*x*BZT ceramics. (a-b) *x* = 0.10, (c-d) *x* = 0.15.

The Vogel-Fulcher fittings of the KWW parameters, f_{KWW} and β for both compositions are presented in Figure 5.9, showing a good fit of the experimental data. The extrapolation of the lines obtained from fitting show that both f_{KWW} and β go to zero at the same temperature for each composition. This graph shows the importance of expressing the relaxation time in terms of frequency, since a plot of τ in the time domain cannot be extrapolated to the temperature axis as it diverges to infinity.

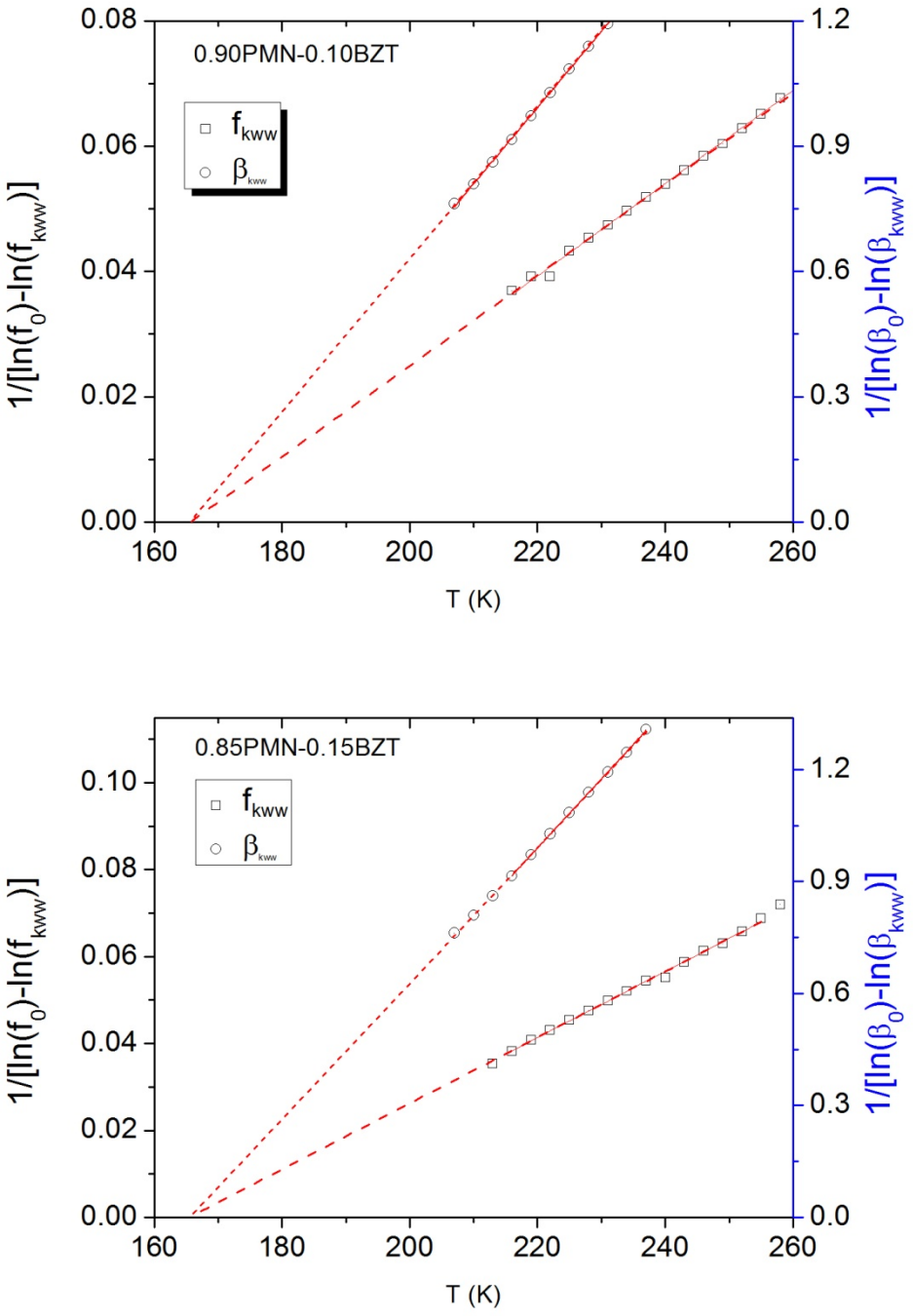

Figure 5.9: Linear Vogel-Fulcher fitting plot of the β and f_{KWW} parameters for the 1-*x*PMN-*x*BZT ceramics with *x* = 0.10 and 0.15. The red line indicates the extrapolation of the freezing temperature when β_0 and $f_{KWW} = 0$.

Table 5.2 : Vogel Fulcher fitting values for the KWW parameters of the (1-*x*)PMN-*x*BZT ceramics. Data for PMN are taken from Ref [13]

Composition	τ_0 (s)	E_τ (eV)	T_f (K)	β_0 (s)	E_β (eV)	T_β (K)
PMN	1.6×10^{-14}	0.069 ± 0.005	213 ± 2	0.43 ± 0.02	0.00361 ± 0.00043	210 ± 2
0.90PMN-0.10BZT	1.5×10^{-13}	0.116 ± 0.003	167 ± 3	0.40 ± 0.02	0.00467 ± 0.00010	169 ± 3
0.85PMN-0.15BZT	1.5×10^{-12}	0.111 ± 0.002	166 ± 2	0.36 ± 0.02	0.00467 ± 0.00031	166 ± 4

Table 5.2 gives the parameters obtained from fitting the KWW parameters to the Vogel-Fulcher law described in Equation 5.2. The value of the pre-exponential parameter, τ_0 increases with the BZT content. The reciprocal of this value is the Debye frequency, which is the upper limit of frequency the polarization mechanism can respond to and thereby contribute to the permittivity. The β_0 parameter also decreases with increasing BZT concentration. This indicates that the upper limit of the ε'' peak width increases with BZT content, since a smaller β value corresponds to a broader peak width. Furthermore, the temperature at which these two values go to zero has the same value for each composition, which is the same behaviour as first seen in the canonical relaxor PMN [13]. This finding further supports previous work that the two parameters describing conventional relaxor susceptibility should go to zero at the same temperature in relaxor ferroelectrics[13]. Moreover, the addition of BZT to PMN results in a decrease in the freezing temperature. This decrease may come from the increase in chemical disorder at the A and B-sites which may disrupt the growth of polar nanoregions, reduce their correlation length, and weaken their interactions. This argument may hold true assuming that the activation energy for the reorientation of a cluster of PNRs scales with the mean volume of the cluster. Recent theoretical work based on this assumption has shown that

the characteristic relaxation time is found to diverge as the PNR volume reaches the percolation limit [22].

5.6 Conclusions

Ceramics of a new binary solid solution system from two complex perovskite end members [(1-*x*)PMN-*x*BZT] were prepared by solid state reaction. The upper limit of thermal stability for the perovskite phase decreases with increasing *x*, and the room temperature structure remains pseudocubic or rhombohedral up to the solubility limit of *x* = 0.275. All the compositions studied show a broad and diffuse peak in the temperature and frequency dependencies of the dielectric permittivity $\varepsilon'(T)$, the temperature of which increases with increasing frequency, indicating typical relaxor behaviour. The dielectric properties of all the samples studied were found to follow the quadratic relationship for the temperature dependence of permittivity, with the diffuseness δ parameter increasing linearly with the addition of BZT. In addition, the ΔT_{max} = [T_{max} (100 kHz) - T_{max} (10 Hz)] increases with the increasing amount of BZT, indicating an increased dielectric dispersion. Therefore, the addition of BZT is found to enhance the relaxor behaviour of canonical relaxor PMN. This unusual enhancement can be attributed to the increase in chemical disorder caused by the BZT end member which introduces two additional heterovalent cations on the octahedral B-site and introduces the Bi^{3+} cation on the A-site of the perovskite structure. Furthermore, the addition of BZT to PMN decreases the freezing temperature at which the parameters that describe the conventional relaxor susceptibility diverge. This phenomenon can be explained by an hindering of the growth of the polar nanoregions as a result of increased chemical disorder.

References

[1] A. A. Bokov and Z-. G. Ye, "Recent progress in relaxor ferroelectrics with perovskite structure," *Journal of Materials Science,* vol. 41, pp. 31-52, (2006).

[2] Z-. G. Ye, "Relaxor ferroelectric complex perovskites: Structure, properties and phase transitions," *Key. Eng. Mat.,* vol. 155-1, pp. 81-122, (1998).

[3] S. W. Choi, T. R. Shrout, S. J. Jang and A. S. Bhalla, "Dielectric and Pyroelectric Properties in the (1-x)$Pb(Mg_{1/3}Nb_{2/3})O_3$-x$PbTiO_3$ System," *Ferroelectrics,* vol. 100, pp. 29-38, (1989).

[4] S. E. E. Park and W. Hackenberger, "High performance single crystal piezoelectrics: applications and issues," *Current Opinion in Solid State and Materials Science,* vol. 6, pp. 11-18, (2002).

[5] M. R. Suchomel, A. M. Fogg, M. Allix, H. J. Niu, J. B. Claridge and M. J. Rosseinsky, "Bi_2ZnTiO_6: A lead-free closed-shell polar perovskite with a calculated ionic polarization of 150 μC/cm^2" *Chemistry of Materials,* vol. 18, pp. 4987-4989, (2006).

[6] I. Grinberg, M. R. Suchomel, W. Dmowski, S. E. Mason, H. Wu, P. K. Davies and A. M. Rappe. "Structure and polarization in the high T-c ferroelectric $Bi(Zn_{1/2}Ti_{1/2})O_3$-$PbTiO_3$ solid solutions." *Physical Review. Letters,* vol 98*,* pp. 107601:1-10. (2007)

[7] M. R. Suchomel and P. K. Davies, "Enhanced tetragonality in (x)PbTiO3-(1-x)Bi $(Zn_{1/2}Ti_{1/2})O_3$ and related solid solution systems," *Applied Physics Letters,* vol. 86, pp. 262905:1-4, (2005).

[8] Z-. G. Ye, "High Performance Single Crystals of Complex Perovskite Solid Solutions," *Materials Research Bulletin,* vol. 34, pp. 277-282, (2009).

[9] Z-. G. Ye, Y. Bing, J. Gao, A. A. Bokov, P. Stephens, B. Noheda and G. Shirane, "Development of ferroelectric order in relaxor (1-x)$Pb(Mg_{1/3}Nb_{2/3})O_3$ x$PbTiO_3$ ($0 <= x <= 0.15$)," *Physical Review B,* vol. 67, pp. 104104:1-8,(2003).

[10] D. Viehland, S. J. Jang, L. E. Cross and M. Wuttig, "Freezing of the Polarization Fluctuations in Lead Magnesium Niobate Relaxors," *Journal of Applied Physics,* vol. 68, pp. 2916-2921, (1990).

[11] A. A. Bokov, Y. H. Bing, W. Chen, Z-. G. Ye, S. A. Bogatina, I. P. Raevski, S. I. Raevskaya and E. V. Sahkar, "Empirical scaling of the dielectric permittivity peak

in relaxor ferroelectrics," *Physical Review B,* vol. 68, pp. 0521020:1-4, Aug. (2003).

[12] A. A. Bokov and Z-. G. Ye, "Phenomenological description of dielectric permittivity peak in relaxor ferroelectrics," *Solid State Communications,* vol. 116, pp. 105-108, (2000).

[13] A. A. Bokov and Z-. Ye, "Double freezing of dielectric response in relaxor $Pb(Mg_{1/3}Nb_{2/3})O_3$ crystals." *Physical Review B,* vol 74, p. 132102:1-9. (2006)

[14] A. A. Bokov and Z-. G. Ye, "Freezing of dipole dynamics in relaxor ferroelectric $(1-x)Pb(Mg_{1/3}Nb_{2/3})O_3$-$xPbTiO_3$ as evidenced by dielectric spectroscopy," *Journal of Physics-Condensed Matter,* vol. 12, pp. L541-L548,. (2000).

[15] S. L. Swartz and T. R. Shrout, "Fabrication of Perovskite Lead Magnesium Niobate," *Materials Research Bulletin,* vol. 17, pp. 1245-1250, (1982).

[16] B. Noheda, D. E. Cox, G. Shirane, J. Gao and Z-. G. Ye, "Phase diagram of the ferroelectric relaxor $(1-x)Pb(Mg_{1/3}Nb_{2/3})O_3$-$xPbTiO_3$," *Physical Review B,* vol. 66 p 054104:1-10 , (2002).

[17] O. Bidault, E. Husson and P. Gaucher, "Study of the electric field-induced low temperature phase in $(1-x)Pb(Mg_{1/3}Nb_{2/3})O_3$-$xPbTiO_3$: Titanium influence," *Journal of Physique III France,* vol. 7, pp. 1163-1172, (1997).

[18] R. E. Cohen. Origin of ferroelectricity in perovskite oxides. *Nature 358(6382),* pp. 136-138. (1992)

[19] C. Lei, A. A. Bokov and Z-.G. Ye, "Ferroelectric to relaxor crossover and dielectric phase diagram in the $BaTiO_3$-$BaSnO_3$ system," *Journal of Applied Physics,* vol. 101, pp. 084105:1-10, 2007. (2007).

[20] X. F. Long, A. A. Bokov, Z-. G. Ye, W. G. Qu and X. L. Tan, "Enhanced ordered structure and relaxor behaviour of $0.98Pb(Mg_{1/3}\ Nb_{2/3})O_3$-$0.02La(Mg_{1/3}Nb_{2/3})O_3$ single crystals," *Journal of Physics-Condensed Matter,* vol. 20, pp 015210 1-9 (2008).

[21] X. Zhao, W. Qu, X. Tan, A. A. Bokov and Z-. G. Ye, "Influence of long-range cation order on relaxor properties of doped $Pb(Mg_{1/3}Nb_{2/3})O_3$ ceramics," *Physical Review B,* vol. 79, pp. 1441011:1-12, (2009).

[22] R. Pirc and R. Blinc. "Vogel-fulcher freezing in relaxor ferroelectrics." *Physical Review B,* vol 76, pp. 020101:1-3. (2007).

CHAPTER 6
Structure, Properties and Phase Diagram of the $Pb(Mg_{1/3}Nb_{2/3})O_3$ -$PbTiO_3$- $Bi(Zn_{1/2}Ti_{1/2})O_3$ Ternary Solid Solution System

6.1 Abstract:

The ternary solid solution of xPb($Mg_{1/3}Nb_{2/3}$)O_3 - $y$$PbTiO_3$- zBi($Zn_{1/2}Ti_{1/2}$)O_3 [xPMN – yPT – zBZT] is studied in order to investigate its structural, dielectric and piezo-/ferroelectric properties as a function of temperature and composition for use as a lead-reduced, high Curie temperature (T_C) piezoelectric material. It is found that the system exhibits a wide range of ferroelectric phase transition temperatures, reaching 700 °C along the (1-x)BZT-xPT pseudo-binary line of the ternary system. Although the binary system shows very large tetragonality, it is possible to produce highly dense, pure-phase ceramics at relatively low sintering temperatures (< 1100°C) compared to purely lead-based ceramics. The mechanism of this enhanced sintering process is attributed to the eutectic melting between PbO and Bi_2O_3. The large strain (c/a > 1.109) and high phase transition temperatures on the (1-x)BZT-xPT binary system side make these ceramic compositions difficult to pole at room temperature. However, increasing the PMN content in the ceramics provides a handle to control the phase transition temperatures so as to reduce the relative coercive fields, making it possible to pole the samples, a crucial process for device applications. By balancing the ease of poling, phase transition temperatures and reducing the relative amount of the lead component, the PMN-PT-BZT system shows its potential as a lead-reduced high T_C piezo- and ferroelectric system.

6.2 Introduction

The complex perovskite solid solution $Pb(Mg_{1/3}Nb_{2/}3)O_3$ (PMN) exhibits typical relaxor ferroelectric behaviour [1-8], while perovskite $PbTiO_3$ is a prototypical ferroelectric material with a high Curie temperature (T_C = 490 °C) and high spontaneous polarization. The solid solution between these two compounds: $(1-x)Pb(Mg_{1/3}Nb_{2/}3)O_3$-$xPbTiO_3$ [(1-*x*)PMN-*x*PT], has shown some of the highest piezoelectric properties in the form of single crystals and ceramics for compositions near the rhombohedral side of the morphotropic phase boundary (MPB) (x = 0.30-0.35)[9-13], making it an excellent material for use in a wide range of applications, such as for the production and detection of sound, generation of high voltages, microbalances, and ultra fine focusing of optical assemblies. However, the PMN-PT system suffers from some drawbacks such as a low T_C and an even lower rhombohedral to tetragonal transition temperature, (T_{MPB}). Furthermore, its low coercive field necessitates the use of a bias field in high power piezoelectric applications in order to prevent polarization switching.

Most end members in their solid solution with PT cause the phase transition temperatures to be below that of PT itself (T_C = 490 °C)[14, 15], however, $Bi(Zn_{1/2}Ti_{1/2})O_3$ (BZT) has been shown to be an exception as it results in a significant increase in the phase transition temperature of its solid solution with PT, BZT-PT, reaching 700 °C at its solubility limit (40 mole % BZT in PT)[16, 17]. However, the ternary system between PMN-PT and BZT is not known. In this work, the ternary solid solution between PMN, PT and BZT was prepared by solid state reaction and its structural, dielectric, ferroelectric and piezoelectric properties were investigated as a function of temperature and composition. The system is expected to show a wide range

of phase transition temperatures as high as 700 °C on the BZT-PT side of the ternary phase diagram making the ceramics useful as lead-reduced, high temperature piezoelectric materials for electromechanical applications.

6.3 Experimental

The ceramics of $Pb(Mg_{1/3}Nb_{2/3})O_3$-$PbTiO_3$-$Bi(Zn_{1/2}Ti_{1/2})O_3$ [PMN-PT-BZT] were prepared by solid state reaction using all the constituent oxides as received. The powders were reacted using the two step columbite method[18], in which MgO (99.95 % Alfa Aesar) and Nb_2O_5 (99.9 % Alfa Aesar) were first reacted to form the $MgNb_2O_6$ columbite phase [18]. The columbite phase was then reacted with the remaining oxides to form the perovskite phase. A stoichiometric amount of Nb_2O_5 and a 3 mole % excess of MgO powders were mixed together, ball milled in acetone in a rotary tumbler using 5 mm zirconia balls for 12 hours, pressed uniaxially into a single pellet and then calcined at 1100 °C for 4 hour in a muffle furnace to form the $MgNb_2O_5$ columbite phase. The pellet was then pulverized, re-milled in a tumbler for 24 hours and checked by X-ray diffraction to confirm the formation of pure columbite phase. In the second step, stoichiometric amounts of $MgNb_2O_6$, ZnO (99.9 % Koujoundo Chemicals), TiO_2 (99.5 % Alfa Aesar), Bi_2O_3 (99.9% Alfa Aesar) and PbO (99.9 % Alfa Aesar) were mixed together. The mixture was ball milled before being pressed into pellets for calcination at 850 °C for 4 hours. The calcined pellets were then reground, ball milled for 24 hours and pressed uniaxially into 10 mm diameter discs for sintering. In order to prevent PbO and Bi_2O_3 from evaporating, the pressed pellets were placed in a bed of sacrificial PMN-PT-BZT powder (of the same composition) covering the pellets during the sintering process that took place at various temperatures between 1000 °C and 1100 °C to form ceramics.

The sintered ceramics were polished using silicon carbide sand paper (220, 400, 600 grit) to produce flat and parallel surfaces. X-ray powder diffraction was performed on the ceramics using Cu K_α radiation (40 mA, 40 kV Bruker D8 Advance Diffractometer, step size = 0.02 °/step, 2θ = 10 ° - 80 °)). Gold layers were sputtered (Anatech Hummer 6.2,10 min, 15 mA plasma discharge current) on to the parallel surfaces of the ceramics for electrical characterization. In order to connect the electrodes to the electrical characterization equipment and poling apparatus, gold wires were attached to the sample and instrument electrodes using colloidal silver paste. The temperature dependence of the dielectric permittivity ($\varepsilon(T)$) was measured at various frequencies using two setups, depending on the temperature interval to be measured. For $\varepsilon(T)$ measurements between -160 °C and 350 °C, a Novocontrol Alpha high resolution broadband dielectric analyzer was used to take isothermal measurements every 3 °C. For the measurements taken from 20 °C to 700 °C, a Solartron S1260 impedance analyzer was used in conjunction with an S1296 dielectric interface and a homemade furnace powered by an Omega CN3001 temperature controller used to take isothermal measurements every 5 °C. The ferroelectric hysteresis loops were measured at a frequency of 10 Hz, using a Radiant Technologies RT66A standardized ferroelectric testing system in conjunction with a Trek 609E-6 High Voltage Bipolar Amplifier. The samples were poled using a Stanton PS350 high voltage power source at room temperature in silicone oil and the piezoelectric constants were measured by means of a quasistatic piezoelectric meter, Model ZJ-6B as described in Section 2.3.

6.4 Motivations and Challenges in the PMN-BZT-PT system

Since the ternary system between PMN-BZT-PT has not been investigated to date, many questions on the preparation, limits of solubility and structure of the perovskite phases remain to be answered. In addition, one of the major underlying goals of materials science is to characterize the physical properties and performance of the system as a function of the composition and preparation. Furthermore, once the structure and properties are investigated and understood, the structure property relationships must be developed in order to provide insight into how the crystal structure and chemical composition affect the performance and properties of the materials.

Structure property relationships are vital in optimizing material properties as we have seen in the example of the MPB described in Chapter one, in which many of the electrical properties, such as d_{33} and k_P, reach their optimum values as a function of composition near this region [19]. Thus further interest is given to finding a morphotropic phase boundary in this ternary system, since two of the end members are tetragonal, and they must undergo a phase transformation when approaching the rhombohedral PMN end member. Further studies were performed in order to investigate if any compositions in the system help to address the drawbacks found in the PMN-PT system such as the low T_C and low E_C.

In order to study a ternary phase system, it is important to be able to read and understand triangular-coordinate ternary phase diagrams. In such diagrams, each corner of the triangle corresponds to 100% of one of the three constituents of the system (e.g. A, B or C). All compositions containing only two components lie on one edge of the

triangle, so the mixtures of A and C (no B) lie on the AC line. The closer a point is to a corner, the more of the corresponding component there is in the mixture. As one moves from C to A along the edge, the concentration of A increases. Each point inside the triangle represents a composition containing all three components. Figure 6.1 shows an example of an arbitrary composition at point P. The composition of P can be read by extending parallel lines to each side of the triangle, as shown in Figure 6.1(a). The lengths of lines PR, PS and PQ are proportional to the mole fraction of each component. This generalizes so that any point inside the triangle represents a composition for which the sum of the three constituents is constant. In other words, the ratio between the length of each segment to the length of the edge of the triangle can be used to express the percentages of the overall composition. Thus, x(%A) + y(%B) + z(%C) = 100%.

Since describing compositions in a ternary systems can be quite complex using this notation, one useful approach to systematically study ternary systems is to investigate compositions by constructing pseudo-binary lines which simplify the composition variations in the system. Figure. 6.1 shows an example of several pseudo-binary lines and the resulting formula for the pseudo binary solid solution along that line. Pseudo-binary lines that originate from one end member, e.g. A in the ABC ternary system, will have the ratio of B to C remain constant along the line. Pseudo-binary lines that begin along the mid-edge of the phase diagram and run parallel to one of the binary lines between the end members (e.g. between B and C in Fig 6.1(c)) will hold the concentration of the remaining member constant (in this case, A). The construction of appropriate pseudo-binary lines facilitates the investigation of the areas of interest in a

systematic fashion. This method allows for taking a cross section in any direction and simplifies the expression of the compositional variance along the line.

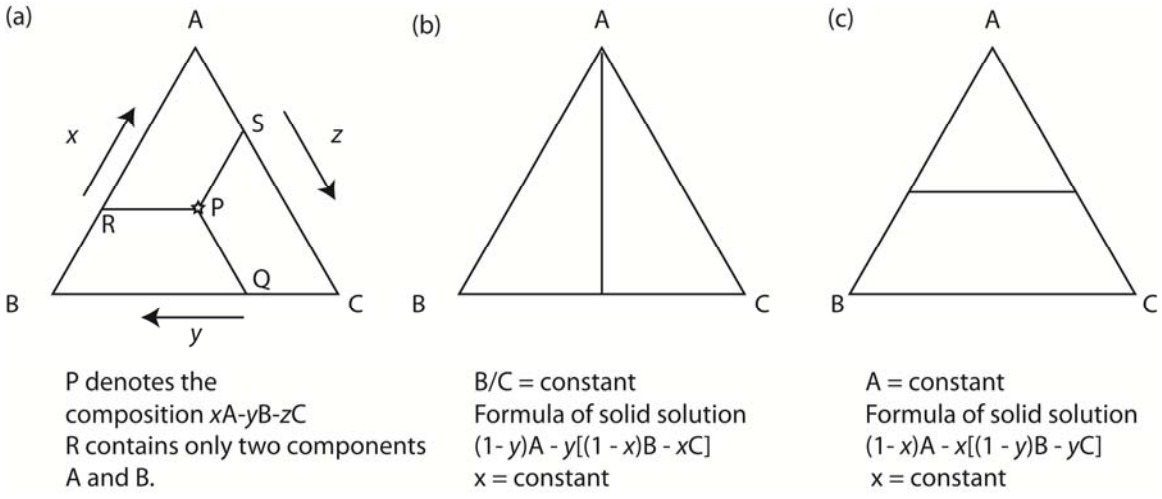

Figure 6.1: Schematics of ternary phase diagrams: (a) The point P denotes a composition containing all three phase components in the ratio *x*A-*y*B-*z*C and any point along the edge only contains two components (e.g. composition at point R only contain A and B). (b) Pseudobinary line radiating from a corner which represents the pure end compound. (c) Pseodobinary line parallel to one edge.

6.5 The Pseudo-Binary 0.70[(1-*m*)PMN - *m*PT]-0.30BZT System

In order to find compositions with high Curie temperatures in the vicinity of an MPB, the pseudobinary line 0.70[(1-*m*)PMN-*m*PT]-0.30BZT was investigated because the large concentration of BZT along this line was thought to help maintain high Curie temperatures as seen in the (1-*x*)PT-*x*BZT system. Furthermore, from Chapter 5, it is known that the PMN-BZT end of the phase diagram is of rhombohedral symmetry, while the PT-BZT edge of the phase diagram is highly tetragonal, thus facilitating the formation

of a morphotropic phase boundary which may have enhanced properties and higher phase transition temperatures compared to the (1-*m*)PMN-*m*PT system.

6.5.1 Structure

Figure 6.2 shows the X-ray diffraction patterns for the 0.70[(1-*m*)PMN-*m*PT]-0.30BZT ceramics (*m* = 0.30 to 0.90), which indicate pure perovskite phase for all the compositions prepared. Pure perovskite phase could only be obtained for x > 0.30, which is consistent with the solubility limit of *x* = 0.275 along the (1-*x*)PMN-*x*BZT line described in the Chapter 5. There is a change in phase from a pseudocubic or rhombohedral structure to a tetragonal structure at *x* = 0.30 based on the 100 and 001 diffraction peaks at $2\theta \sim 23$ °. The tetragonal distortion becomes more clear as *x* increases as shown by the increasing split of the 100 and 001 peaks, which is characteristic of tetragonal symmetry (See Chapter 2, Fig 2.4). This is confirmed by the variation in the lattice parameters, as a function of composition shown in Figure 6.3, in which the *a* and *c* parameters deviate from each other at *x* = 0.30, where the difference between *a* and *c* increases as *m* increases.

Figure 6.4 shows the variation of the tetragonality, which is the ratio of the *c*/*a* lattice parameters, as a function of composition. The tetragonality rises linearly with increasing PT/BZT content to a maximum value of ~ 1.09 found for *m* = 0.90.

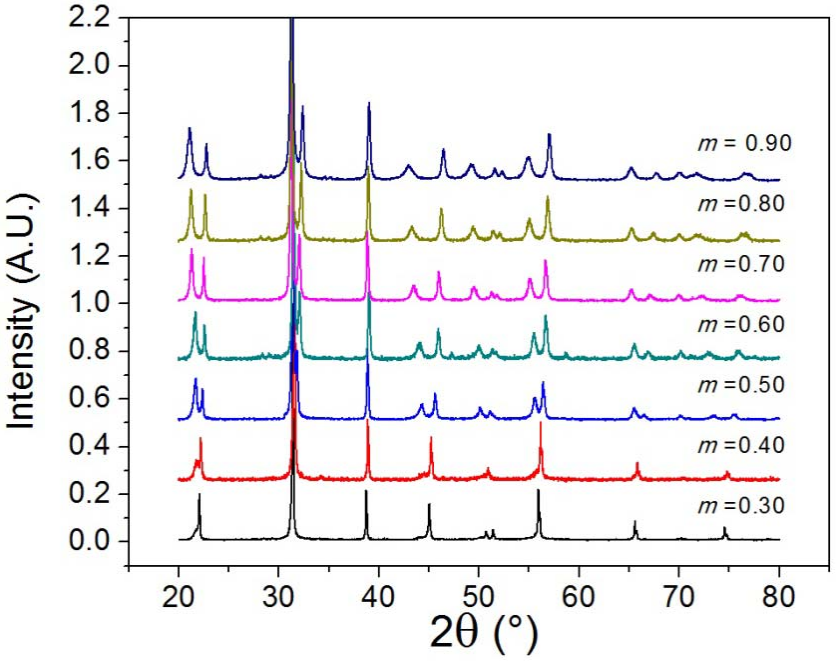

Figure 6.2: X-ray diffraction patterns of 0.70[(1-*m*)PMN-*m*PT]-0.30BZT ceramics (with *m* = 0.30 to 0.90).

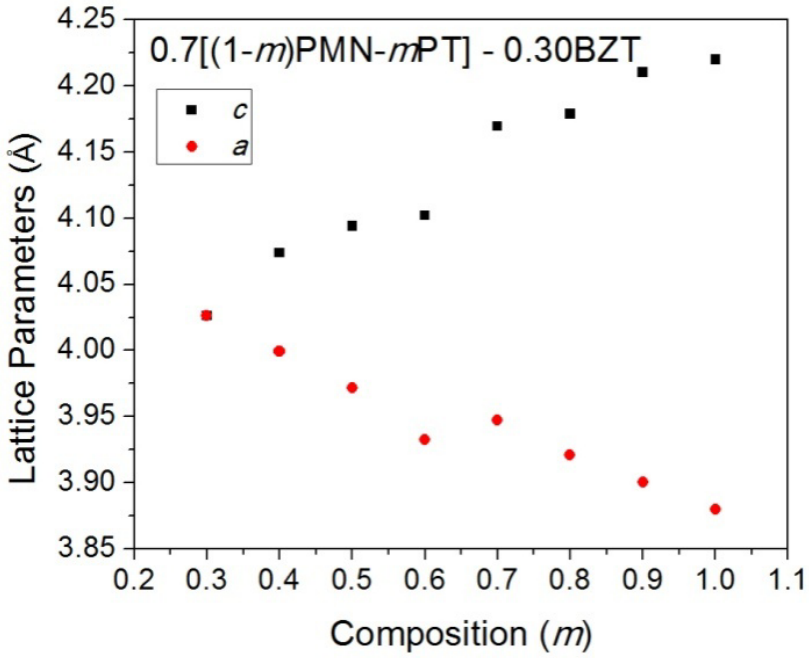

Figure 6.3: Variation of the lattice parameters *a* and *c* as a function of PT content for the 0.70[(1-*m*)PMN-*m*PT]-0.30BZT ceramics.

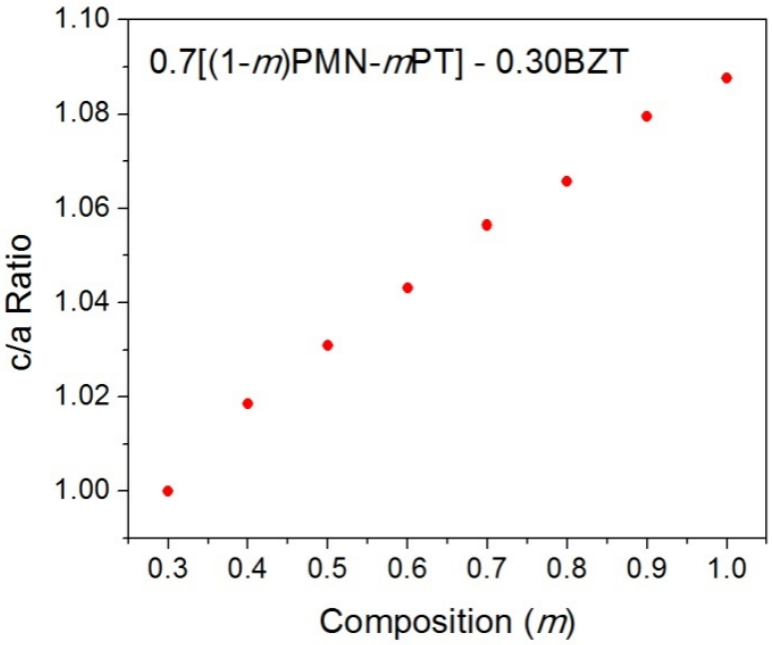

Figure 6.4: Variation of the tetragonality, *c*/*a* lattice parameter ratio as a function of PT content for the 0.70[(1-*m*)PMN - *m*PT]-0.30BZT ceramics.

6.5.2 Dielectric Properties and Phase Transitions

Figure 6.5 shows the temperature dependence of the real part of the permittivity measured at various frequencies (100 kHz, 10 kHz, 1 kHz and 100 Hz) of the 0.70[(1-*m*)PMN-*m*PT]-0.30BZT ceramics. The ceramics of compositions with $x \geq 0.60$ show normal sharp transitions from the paraelectric state to the ferroelectric state at their respective Curie temperatures. The peaks become broader and more diffuse with increasing PMN content and the temperature of maximum permittivity, T_{max}, is dependent on frequency which is characteristic of relaxor behaviour. Although relaxor behaviour is exhibited, it is still possible to produce an electric field induced ferroelectric phase at a temperature below the maximum of permittivity [20, 21]. Figure 6.6 shows the $\varepsilon'(f,T)$

curves of 0.70[0.50PMN-0.50PT]-0.30BZT ceramics upon zero field heating after poling (ZFH af. poling) process. This is done by applying an electric field (E = 10 kV/cm) while cooling to 0 °C and measuring the permittivity with the field removed upon heating. The disappearance of the poled state occurs at the depolarization temperature (T_d) and is indicated by a change in frequency dispersion as well as an abrupt increase in the permittivity upon heating. The composition dependence of the ceramics in the unpoled state is such that the $\varepsilon'(f,T)$ curves show an increase in dispersion and broadening, while T_d decreases with increasing PMN content.

The dispersion observed at high temperature, which increases with temperature and measurement frequency in all ceramic compositions, is due to extrinsic contributions to the permittivity. In single crystal perovskites, this is from the migration of mobile charge carriers such as oxygen vacancies. In the perovskite structure, the oxide ions have the closest distance between nearest ions of the same type, and thus have the smallest migration distance to fill vacancies. As the temperature increases, these vacancies can move as the oxygen ions have sufficient energy to migrate and create polarization. As the temperature is increased or the measurement frequency decreased, a greater number of migrations can occur, leading to an increase in permittivity, which is consistent with the dispersion seen in all of the $\varepsilon'(f,T)$ plots. Furthermore, in ceramics the additional contribution of defects at the grain boundaries can allow for a larger concentration of mobile charge carriers described above.

Based on these structural and dielectric studies, the variations of T_C and T_d as a function of composition are plotted, which shows a linear decrease with increasing PMN content up to the solubility limit at m = 0.30, as shown in Figure 6.7.

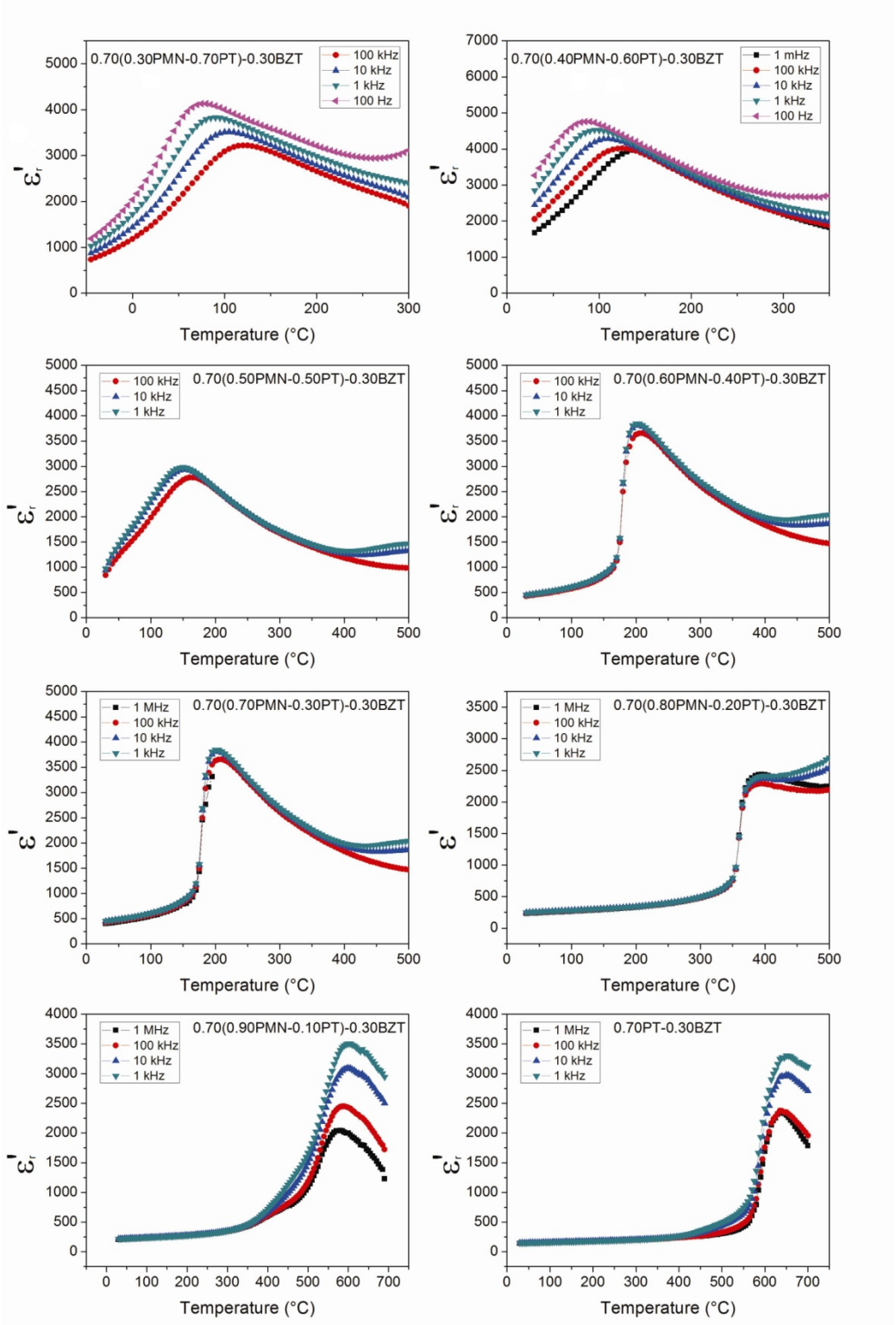

Figure 6.5: Temperature dependence of the real permittivity of the 0.70[(1-*m*)PMN - *m*PT]-0.30BZT ceramics measured at various frequencies.

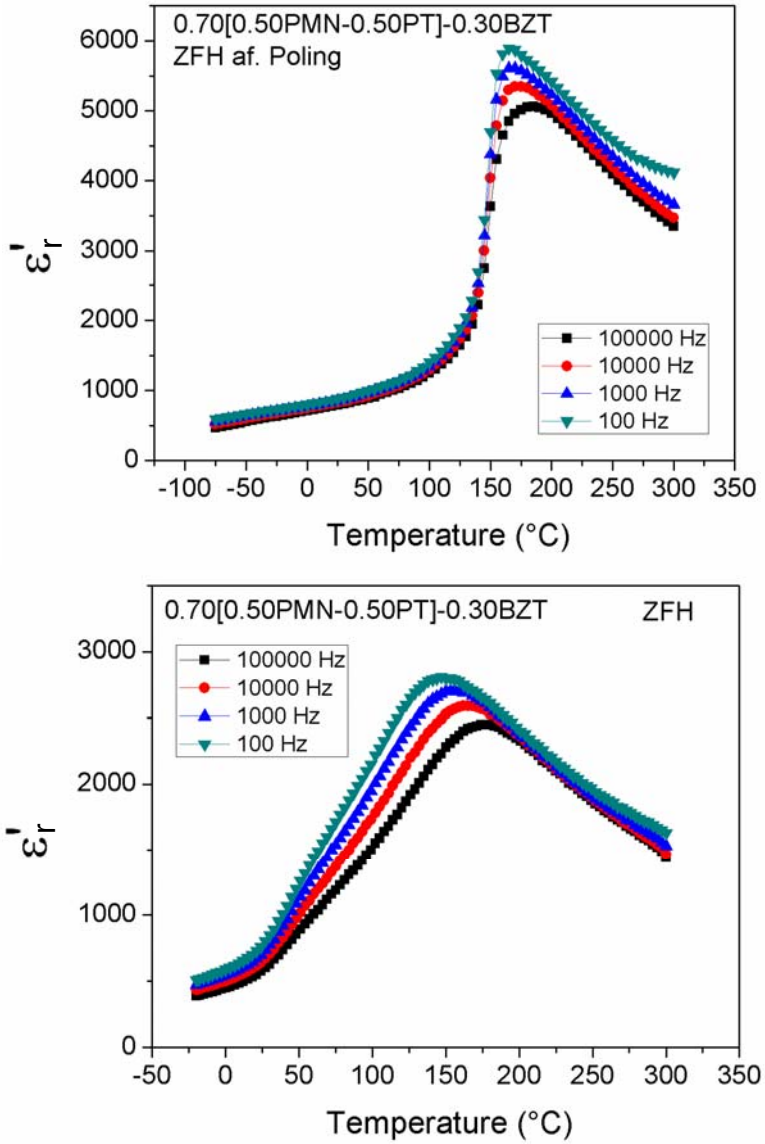

Figure 6.6 : (Top)Variation of the dielectric constant as a function of temperature and frequency measured with zero electric field upon heating (ZFH) for the 0.70(0.50PMN-0.50PT)-0.30BZT solid solution showing typical relaxor dispersion. (Bottom) Variation of the dielectric constant as a function of temperature and frequency measured upon zero-field-heating after heating after field-cooling (10 kV/cm) for the 0.70[0.50PMN - 0.50PT]-0.30BZT ceramic. The dielectric permittivity shows a sharper increase upon heating with attenuated frequency dispersion, indicating an electric field induced ferroelectric state which disappears at 150 °C.

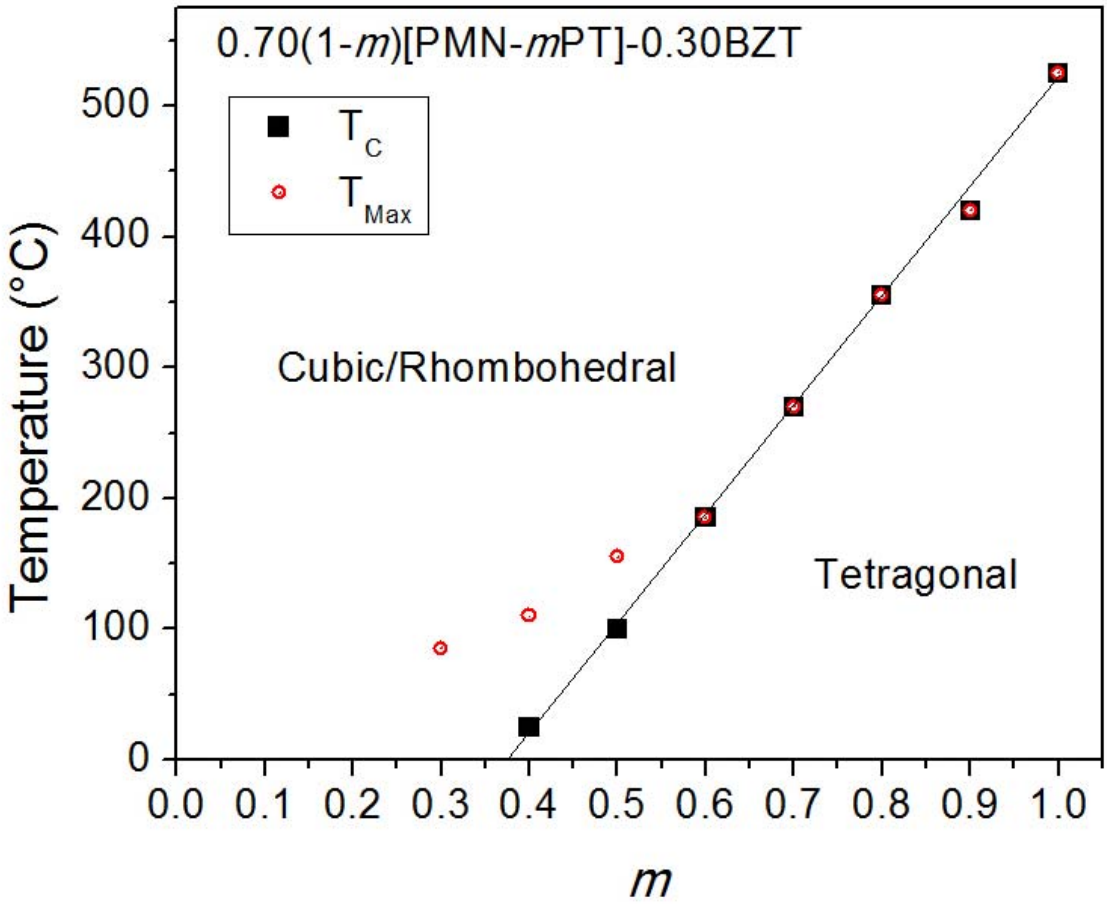

Figure 6.7: Partial structural phase diagram of the 0.70[(1-*m*)PMN-*m*PT]-0.30BZT pseudobinary solid solution (black squares indicate the T_C or T_d, the red circles indicate the maximum of permittivity (T_{Max}) at 1 kHz).

6.5.3 Piezoelectric and Ferroelectric properties

Figure 6.8 shows the polarization versus electric field ($P(E)$) hysteresis loops of the 0.70[(1-*m*)PMN-*m*PT]-0.30BZT ceramics (with m = 0.40-1.00). The coercive field (E_C) increases with PT content. It was possible to obtain saturated hysteresis loops for ceramics of m = 0.40 - 0.60. However, the coercive field increased to the point where it was not possible to obtain saturated hysteresis loops for all samples measured, because of dielectric breakdown at high fields. For the samples of $m > 0.70$, the coercive fields were larger than those that could be measured with our setup and it was not possible to obtain

saturated hysteresis or large remnant polarizations. These compositions exhibited coercive fields that are larger than the dielectric breakdown strength of the ceramics. The $P(E)$ loops shown for the m = 0.70 - 1.00 samples are shown with the highest electric field that could be applied across the ceramic before breakdown. These measurements do not show significant opening of the hysteresis loops or saturation of the polarization at high field which is characteristic of domain switching. Furthermore, the decreases in polarization with increasing fields is indicative of dielectric breakdown or conductivity through the sample. The decrease in polarization is from the generated charge leaking through the sample instead of staying bound to the electrode surface at high field.

Table 6.1 shows the piezoelectric charge constant for the 0.70[(1-m)PMN-mPT]-0.30BZT ceramics. Along this pseudo binary line, the increase in PT content led to a reduction in the piezoelectric constants for three reasons. Firstly, the decrease in room temperature permittivity leads to a decrease in d_{33}, because the piezoelectric charge constant varies as the square root of the permittivity according to :

$$d_{33} = \sqrt{\varepsilon'_{33} s_{33}} \quad , \qquad 5.1$$

where, s is the elastic compliance, ε' is the real part of the permittivity, and the 33 subscript denotes that the measurement is taken in the same direction as the polar direction.

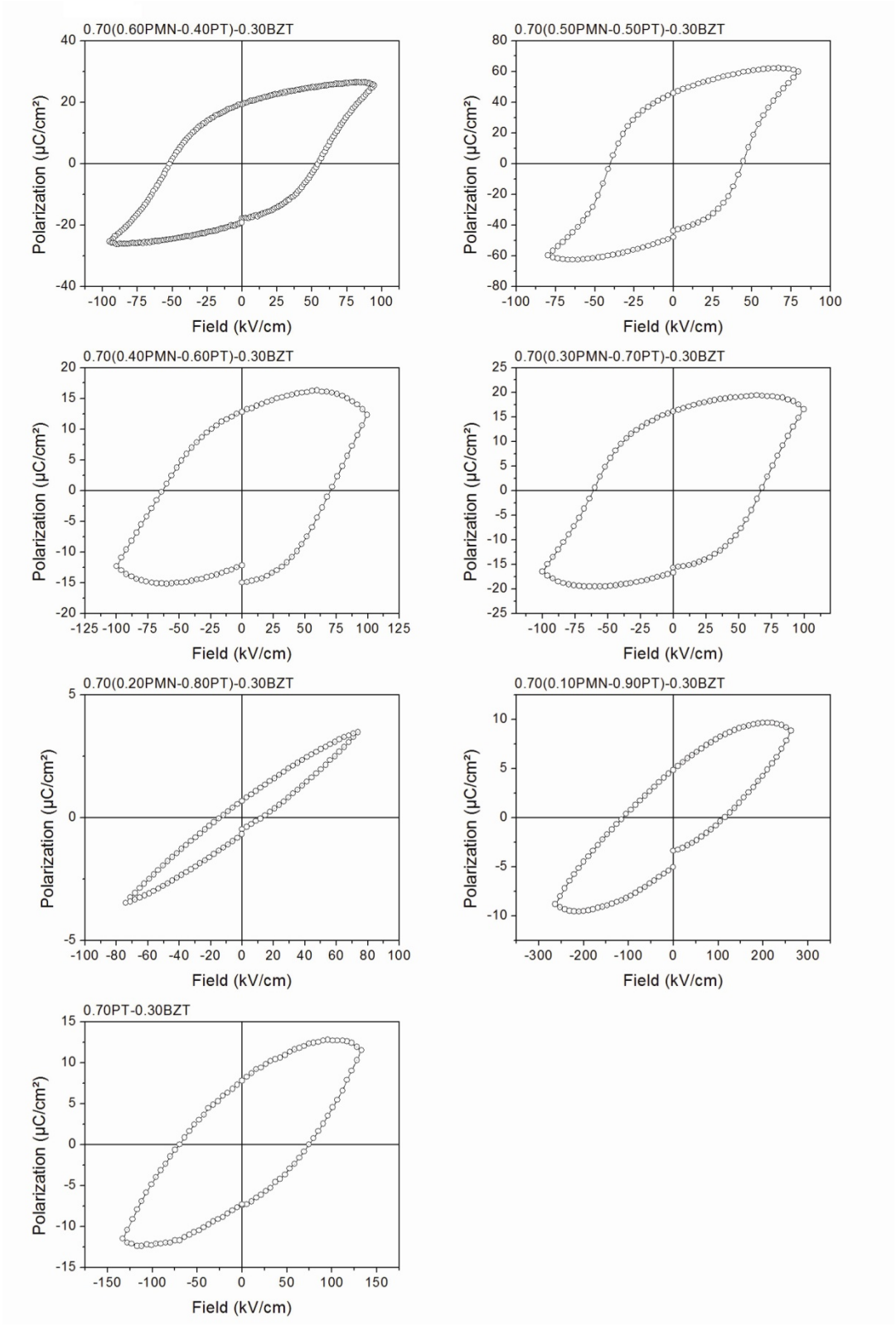

Figure 6.8: Polarization versus electric field measurements of the 0.70[(1-*m*)PMN-*m*PT]-0.30BZT ceramics.

Since all the compositions prepared were of tetragonal symmetry, the mechanism of polarization rotation cannot occur to create the piezoelectric effect. As discussed in Chapter 1, the best piezoelectric properties occur on the rhombohedral side of the PMN-PT and PZN-PT phase diagrams by having the polarization vector rotate within the (011) plane to the <001> direction [10, 19, 22, 23]. Lastly, the large increase in coercive fields with PT content makes it problematic to completely realize the full potential of the piezoelectric properties, due to the fact that it is difficult to pole the ceramics fully without dielectric breakdown. Future efforts will be needed to investigate the appropriate methods to decrease the coercive field or "soften" these ceramics by chemical modification in order to make use of their full piezoelectric potential.

Table 6.1: Piezoelectric and ferroelectric properties of 0.70[(1-*m*)PMN-*m*PT]-0.30BZT (*m* = 0.50-0.70). Ceramics of *m* = 0.70 exhibit coercive fields larger than 100 kV/cm and could not be poled without dielectric breakdown.

Composition	E_C (kV/cm)	T_C (°C)	ε' (RT)	d_{33} (pC/N)
m = 0.40	45	30	2500	38
m = 0.50	50	100	1000	130
m = 0.60	65	200	450	90
m = 0.70	> 90	285	300	10

6.6. The Pseudo-Binary [1-*n*]PMN - *n*[60PT-0.40BZT] System

The pseudobinary system discussed in Section 6.3 does not possess a morphotropic phase transition above room temperature. Another line was investigated in order to find compositions near an MPB, which exhibited high Curie temperatures. In Chapter 5, it was discovered that the addition of BZT to PMN resulted in a decrease of polar order and freezing temperature. In order to maintain high phase transition

temperatures, one end member of pure PMN was chosen as the rhombohedral end member since it exhibits the highest freezing temperature along the (1-*x*)PMN-*x*BZT line. The other end member was fixed along the (1-*y*)PT-*y*BZT binary system with $y = 0.40$ in order to provide the solid solution with high Curie temperature and large tetragonality.

6.6.1 Structure:

Figure 6.9 shows the XRD spectra for (1-*n*)PMN-*n*(0.60PT-0.40BZT) solid solution ($n = 0.20 - 0.80$). All spectra show pure perovskite phase indicating complete solubility for all the compositions studied. The compositions with $n = 0.20 - 0.30$ do not show any peak splitting from the prototypical cubic structure, which would indicate cubic symmetry or a rhombohedral symmetry with distortion from the cubic structure as seen in pure PMN. The XRD patterns of the ceramics with $n > 0.40$ show a peak splitting of the 011 and 002 peaks, which is indicative of tetragonal symmetry. The transformation from cubic to tetragonal phase is more clearly observed from the variation in the *a* and *c* lattice constants as a function of composition shown in Figure 6.10, which shows an increasing divergence of *a* and *c* lattice parameters, with the *c* parameter increasing, while the *a* parameter contracting. Figure 6.11 shows the tetragonality (lattice constant ratio *c/a*) versus composition in which the tetragonality increases from 1.00 (for ceramics of $n < 0.40$), to > 1.00 (at $n = 0.40$), indicating the onset of tetragonal distortion. It reaches a value of 1.08 for the end composition, 0.6PT-0.40BZT. This pseudo binary system differs from the 0.70[(1-*m*)PMN-*m*PT]-0.30BZT line in that the rhombohedral phase appears within the solubility limits of the ternary solid solution system.

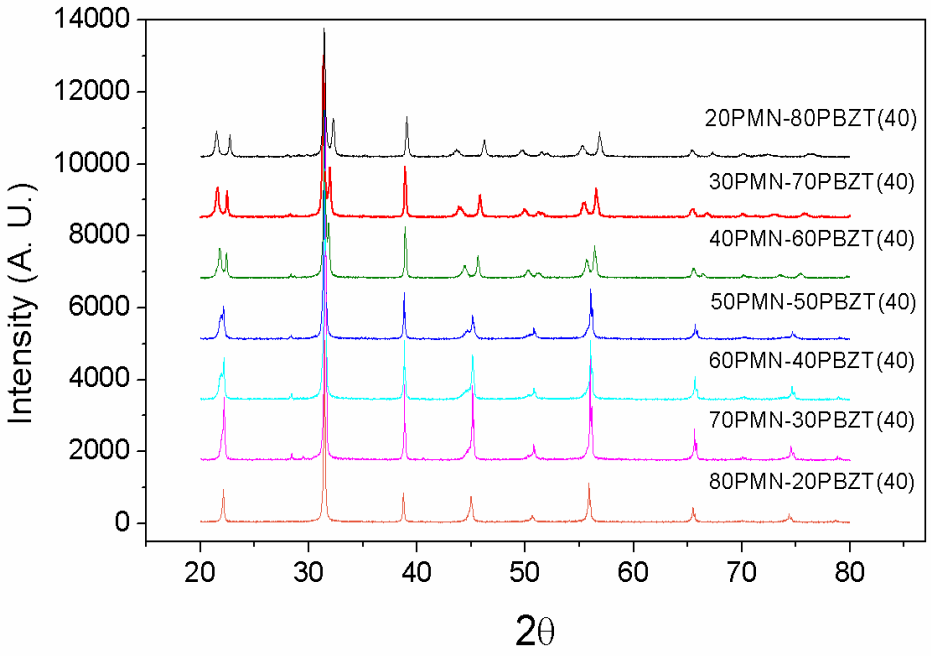

Figure 6.9: X-ray diffraction patterns of (1-*n*)PMN-*n*(0.60PT-0.40BZT) ceramics prepared showing the change in symmetry from rhombohedral/pseudocubic to tetragonal with increasing *n*.

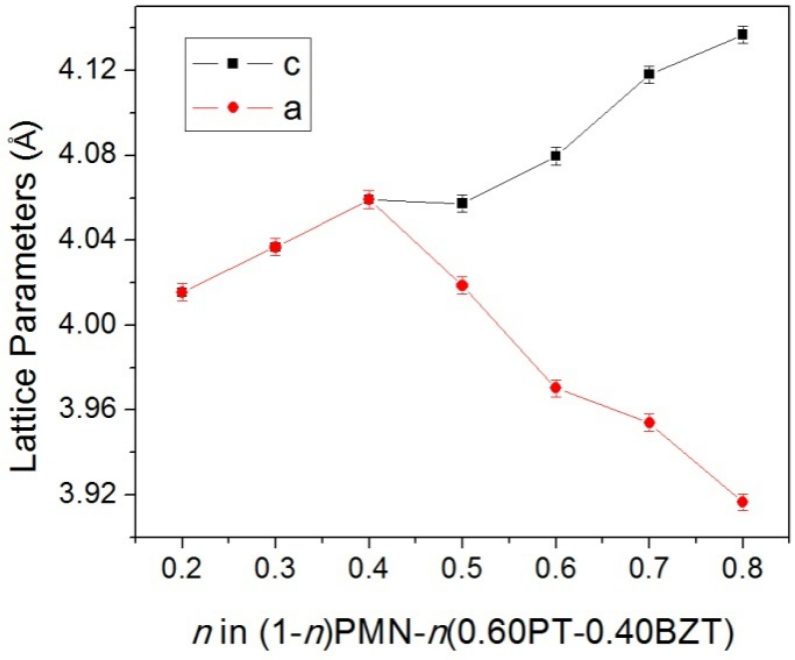

Figure 6.10: The variation of the *a* and *c* parameters as a function of BZT content of the (1-*n*)PMN-*n*(0.60PT-0.40BZT) ceramics as a function of PT/BZT concentration. A morphotropic phase boundary exists at *n* = 0.40

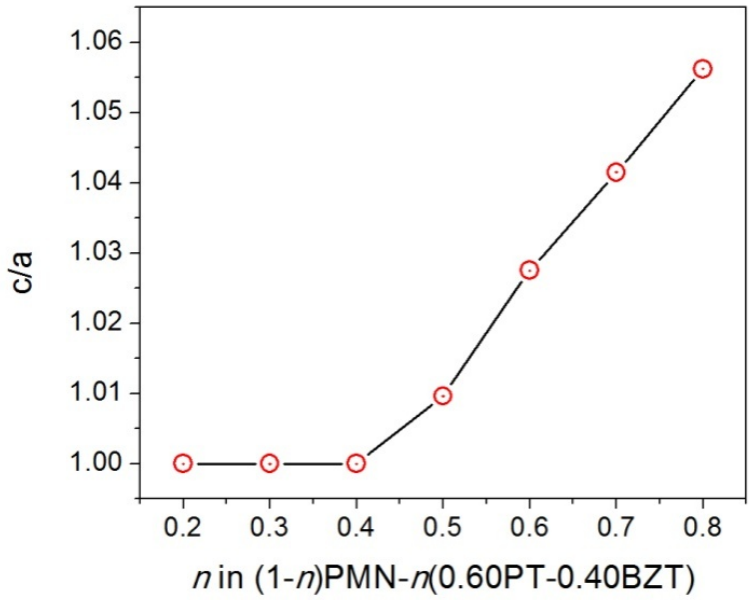

Figure 6.11: The variation of the tetragonality, lattice parameter ratio, *c/a*, as a function of *n* for the (1-*n*)PMN-*n*(0.60PT-0.40BZT) pseudobinary solid solution.

6.6.2 Dielectric Properties and Phase Transitions:

Figure 6.12 shows the real part of the permittivity as a function of temperature measured at various frequencies for the (1-*n*)PMN-*n*(0.60PT-0.40BZT) ceramics. The compositions with $n < 0.70$ show frequency dependent maximum of permittivity, which is characteristic of relaxor behaviour.

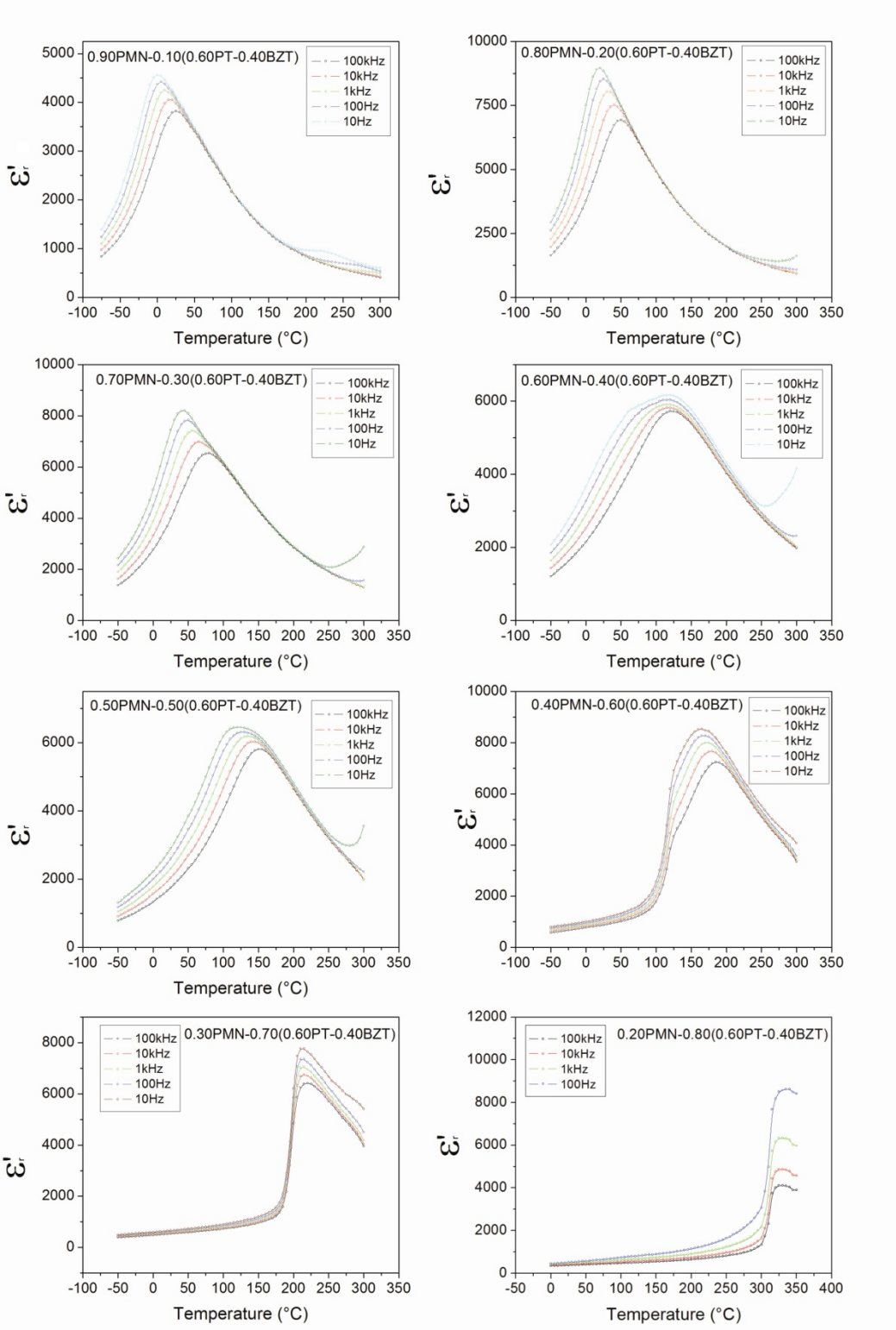

Figure 6.12: Temperature dependence of the real permittivity, ε'_r, measured at various frequencies for the (1-*n*)PMN-*n*(0.60PT-0.40BZT) ceramics.

Although the n = 0.60 ceramic shows frequency dispersion in its maximum of permittivity, it shows an abrupt decrease in the dielectric constant at ~ 100 °C which is indicative of a relaxor to ferroelectric transition. The (1-n)PMN-n(0.60PT-0.40BZT) sample with n = 0.70 and 0.80 exhibits frequency dispersion in the maximum value of the dielectric constant, but the maximum does not vary with temperature, suggesting that it is not from relaxor dispersion. The dispersion may instead be due to a contribution from mobile charge carriers as discussed earlier.

As for the composition displaying relaxor behaviour in the previous Section, an electric field induced transition from a relaxor to a ferroelectric state could be induced by applying an electric field (10 kV/cm) at a temperature well below (>50 °C) the T_{max}. Figure 6.13 shows the ZFH after poling measurement for the ceramics with n = 0.40 - 0.60. The dielectric constant shows an abrupt rise, which is characteristic of the depolarization temperature, T_d.

Figure 6.13 shows the variation of the T_C/T_d and T_{max} of the (1-n)PMN-n(0.60PT-0.40BZT) system as a function of n. As n increases the difference between the T_{Max} and T_d decreases until they converge at a T_C = 265 °C for n = 0.70. The change in the dispersion and phase transition behaviour results from the development of long range polar order from the disordered structure of PMN. This is partially due to the replacement of the non-ferroactive Mg^{2+} ion by the more ferroactive Zn^{2+} and Ti^{4+}ions, which allow for long range polar order to form [14, 24]. By comparing the phase diagram in Figure 6.13 to the room temperature c/a ratio shown in Figure 6.11, it can be seen that the increase of tetragonality from c/a = 1 at n = 0.40 is the result of an increased T_C above room temperature, giving rise to a tetragonal phase at room temperature. At n

= 0.70, the T_{max} and T_C coincide with each other indicating normal ferroelectric behaviour. At $n > 0.70$ T_C increases more rapidly with increasing the (0.60PT-0.40BZT) phase component.

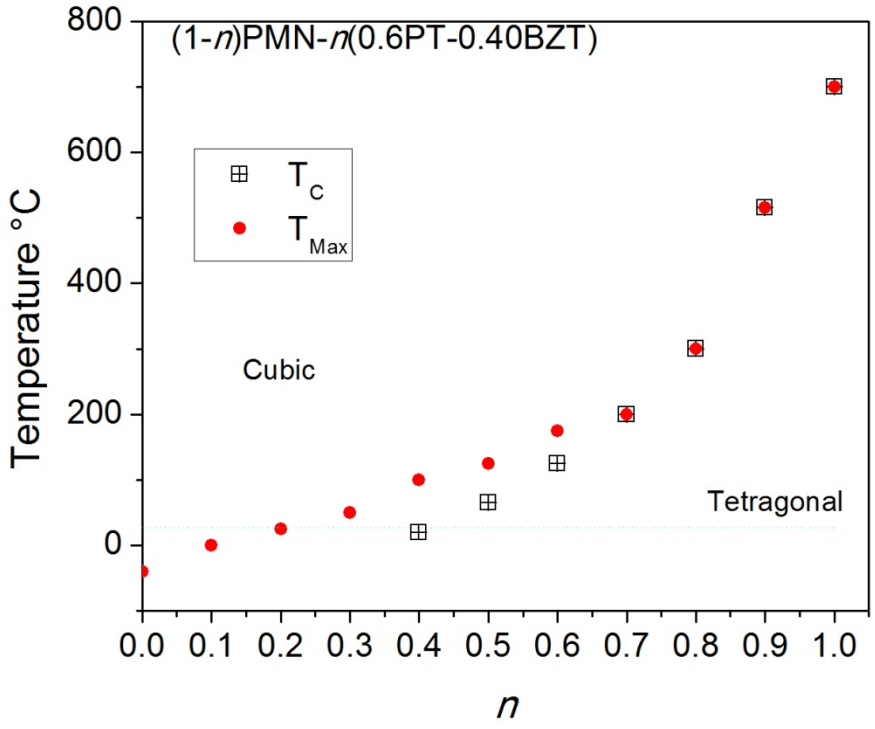

Figure 6.13: Phase diagram of (1-*n*)PMN-*n*(0.60PT-0.40BZT) pseudobinary solid solution, squares indicate the T_C or T_d, the red circles indicate the temperature of maximum of permittivity, T_{max} at 1 kHz.

6.6.3 Piezoelectric and Ferroelectric Properties:

Figure 6.14 shows the polarization versus electric field ($P(E)$) hysteresis loops of the (1-*n*)PMN-*n*(0.60PT-0.40BZT) ceramics (n = 0.30-0.70). The compositions with $n <$ 0.40 show linear dielectric response with no hysteresis or opening of the loop. For n = 0.40, there is a small opening of the loop, indicating ferroelectric behaviour and the

coercive field, E_C, increases with increasing (0.60PT-0.40BZT) phase component, from 12 kV/cm for n = 0.50 to 55 kV/cm for n = 0.60. It was possible to obtain saturated hysteresis loops for ceramics of x = 0.30 - 0.60, however, the coercive field increased to the point where it was not possible to obtain saturated hysteresis loops for all samples measured as a result of dielectric breakdown at high fields. The loss of polarization at high fields, shown in the n = 0.70 loops, is indicative of breakdown in the sample

It is interesting to note that even in the case of ceramics with n = 0.50 (with T_C = 50 °C), the coercive field is relatively high compared to other ferroelectric perovskites with similarly low Curie temperatures. This helps to overcome the drawback that is associated with low ferroelectric transition temperature, making these materials suitable for high power piezoelectric applications. The piezoelectric charge coefficients show the same trend as the room temperature dielectric constant as a function of composition; both decrease with increasing ferroelectric phase transition temperature, T_C.

Although the piezoelectric coefficients of the (1-n)PMN-n(0.60PT-0.40BZT) ceramics are lower than that of ceramics of the PMN-PT binary system, the significantly high coercive field and the tetragonal symmetry of these materials help address the issue of over poling, which is the electric field induced phase transformation into a lower performing monoclinic state that degrades the properties of the (1-x)PMN-xPT ceramics and single crystals [11, 25, 26]. A high coercive field is expected to prevent the over poling effect. The second issue that the large coercive field addresses is the need to operate piezoelectrics in a bias mode to avoid switching the polarization of piezoelectric elements. By increasing the coercive field, it is possible to use high driving fields without the need of a bias to avoid depoling the sample, allowing for higher acoustic

power and larger mechanical displacement. Compositions in the range of n = 0.60 - 0.70 posseses adequately high phase transition temperatures and high coercive fields providing stable and well defined bipolar states for memory in the form of thin films, which would allow for high fields to be applied on these materials without breakdown.

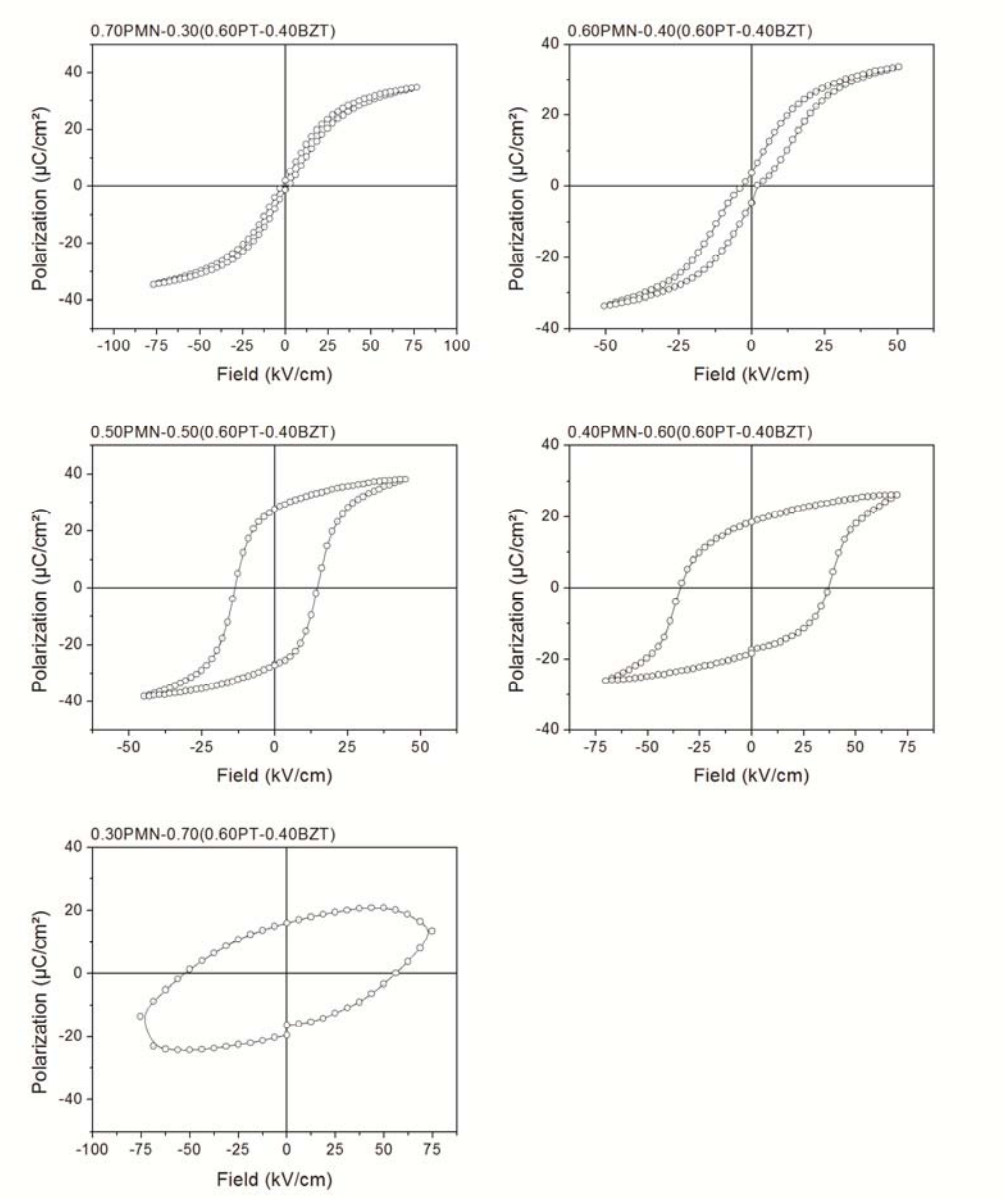

Figure 6.14: Polarization versus electric field ($P(E)$) hysteresis loops of the (1-n)PMN-n(0.60PT-0.40BZT) ceramics with n = 0.30-0.70 measured at room temperature.

Table 6.2: Piezoelectric and Ferroelectric properties of (1-*n*)PMN-*n*(0.60PT-0.40BZT) *n* = 0.50-0.70. Ceramics of *n* = 0.70 exhibitted coercived fields larger than 100 kV/cm and could not be poled without dielectric breakdown.

Composition	E_C (kV/cm)	T_C (°C)	ε' (RT)	d_{33} (pC/N)
n = 0.50	35	50	1500	266
n = 0.60	55	115	1000	150
n = 0.70	> 90	200	700	90

6.7 The (1-*p*)(0.65PMN-0.35PT)-*p*BZT Pseudobinary System

The pseudobinary system studied here is represented by (1-*p*)(0.65PMN-0.35PT)-*p*BZT, which is on the tetragonal side of the MPB. Since some of the best piezoelectric properties are found in the vicinity of the MPB in the (1-*x*)PMN-*x*PT system which is located at $x \sim 0.30$ - 0.35, the effect of BZT addition to the MPB compositions of the PMN-PT binary system is investigated in order to assess its effect on the structure, and ferroelectric properties.

6.7.1 Structure, Symmetry and Phase Components in the Vicinity of the Morphotropic Phase Boundary (MPB).

Figure 6.14 shows the X-ray diffraction patterns for the (1-*p*)(0.65PMN-0.35PT)-*p*BZT ceramics with $p = 0$ - 0.20, showing a tetragonal symmetry for the $p = 0$ to 0.15. The absence of splitting in the 001 peak in $p = 0.20$ indicates a cubic or rhombohedral structure. Figure 6.15 presents the variation of the *a* and *c* lattice constants as a function of BZT concentration. It can be seen that the *a* and *c* lattice parameters converge at 0.20, indicating the transformation from tetragonal to cubic structure.

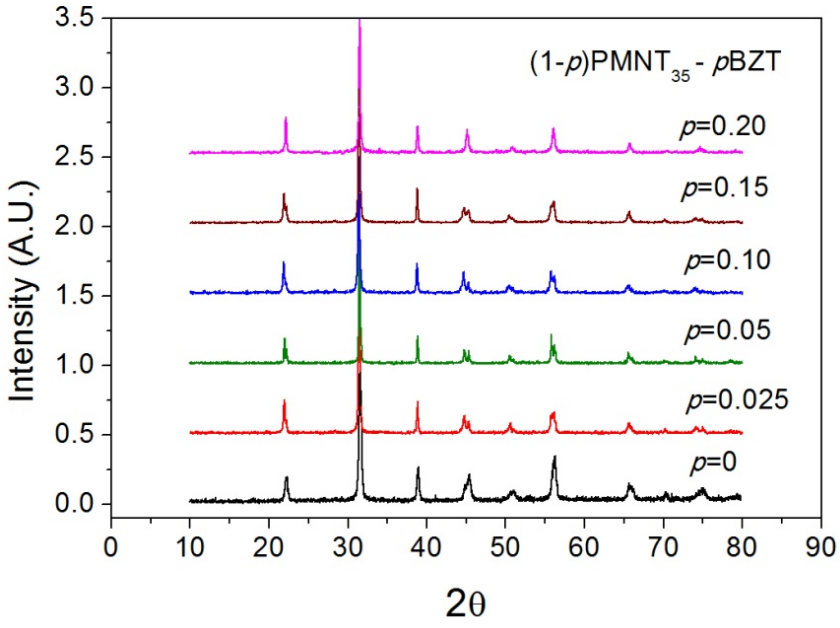

Figure 6.15: X-ray diffraction patterns of the (1-*p*)[0.65PMN-0.35PT]-*p*BZT ceramics with *p* = 0 - 0.20.

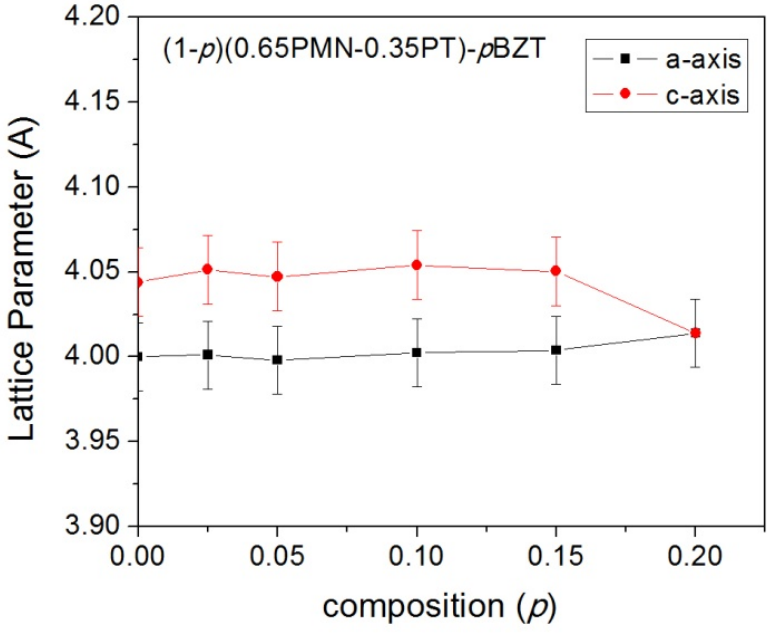

Figure 6.16: The variation of the pseudo-cubic lattice parameters *a* and *c* as a function of BZT content for the (1-*p*)[0.65PMN0.35PT]-*p*BZT ceramics.

6.7.2 Dielectric Properties and Phase Transition Behaviour

Figure 6.16 shows the temperature dependence of the real permitivity measured at various frequencies for the (1-*p*)(0.65PMN-0.35PT)-*p*BZT ceramics. The dielectric behaviour for the p = 0 sample shows typical ferroelectric behaviour with a sharp peak in the permittivity and no frequency dispersion corresponding to the T_C. The Curie temperature decreases and the degree of frequency and temperature dispersion of T_{max} increases with BZT content, which is characteristic of relaxor behaviour. The T_C decreases with increasing BZT content from 180 °C for $p = 0$, to 85 °C for $p = 0.15$. The low temperature slope of the $\varepsilon'(T)$ curve shows the typical shoulder for 0.65PMN-0.35PT[9, 13], corresponding to the tetragonal to monoclinic phase transition, T_{MPB} upon cooling. The shoulder appears at decreasing temperatures with incresing BZT content starting at 70 °C for $p = 0$, to -25 °C for p =0.15, suggesting a reduction in the polar order with the addition of the BZT content. A similar trend has been observed in the PMN-BZT system in which the addition of the polar BZT does not induce a long range ferroelectric phase in the solid solution system (see Chapter 5). Figure 6.17 shows the partial ferroelectric phase diagram of the pseudobinary system of (1-*p*)(0.65PMN-0.35PT)-*p*BZT which displays the cubic phase at high temperature (above T_C) , a tetragonal phase below T_C, and a low tempereature monoclinic phase below T_{MPB}. Increasing BZT content leads to a decrease in both the T_C and the morphotropic phase transition temperature T_{MPB}.

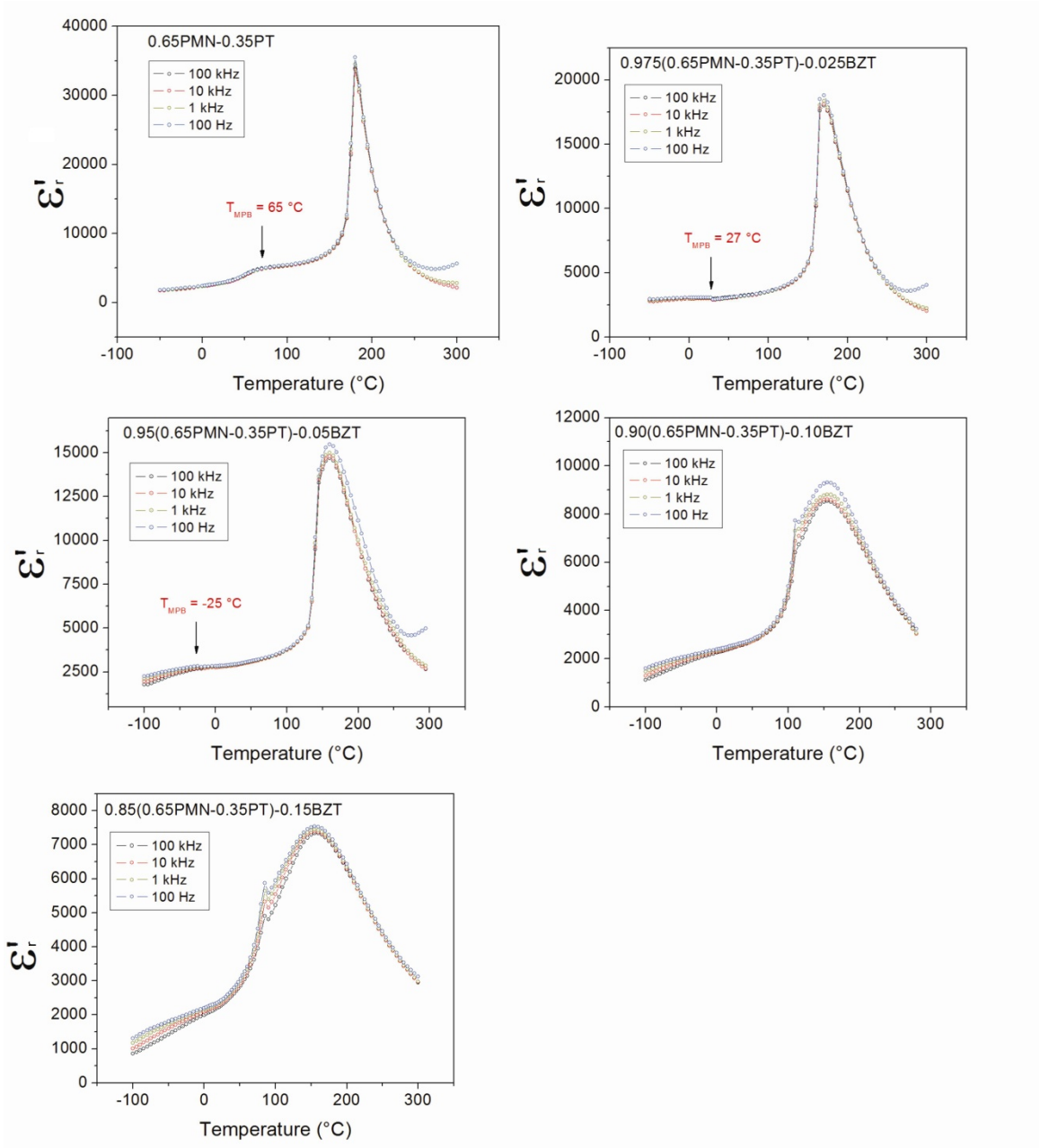

Figure 6.17: Temperature dependence of the real part of the permittivity measured at various frequencies for the (1-*p*)(0.65PMN-0.35PT)-*p*BZT ceramics.

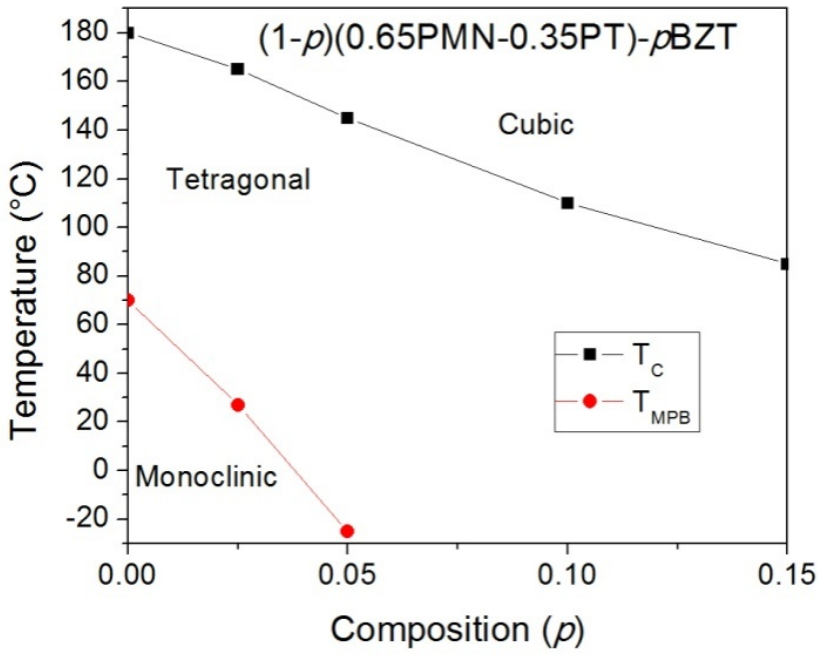

Figure 6.18: Ferroelectric phase diagram of the (1-*p*)(0.65PMN-0.35PT)-*p*BZT pseudobinary solid solution. Black squares indicate the T_C and the red circles indicate the rhombohedral to tetragonal phase transition temperature.

6.7.3 Ferroelectric properties

Figure 6.19 shows the polarization versus electric field hysteresis loops of the (1-*p*)(0.65PMN-0.35PT)-*p*BZT ceramics. The coercive field increases with increasing BZT content, which is the opposite trend seen in most systems where the coercive field decreases with phase transition temperature.

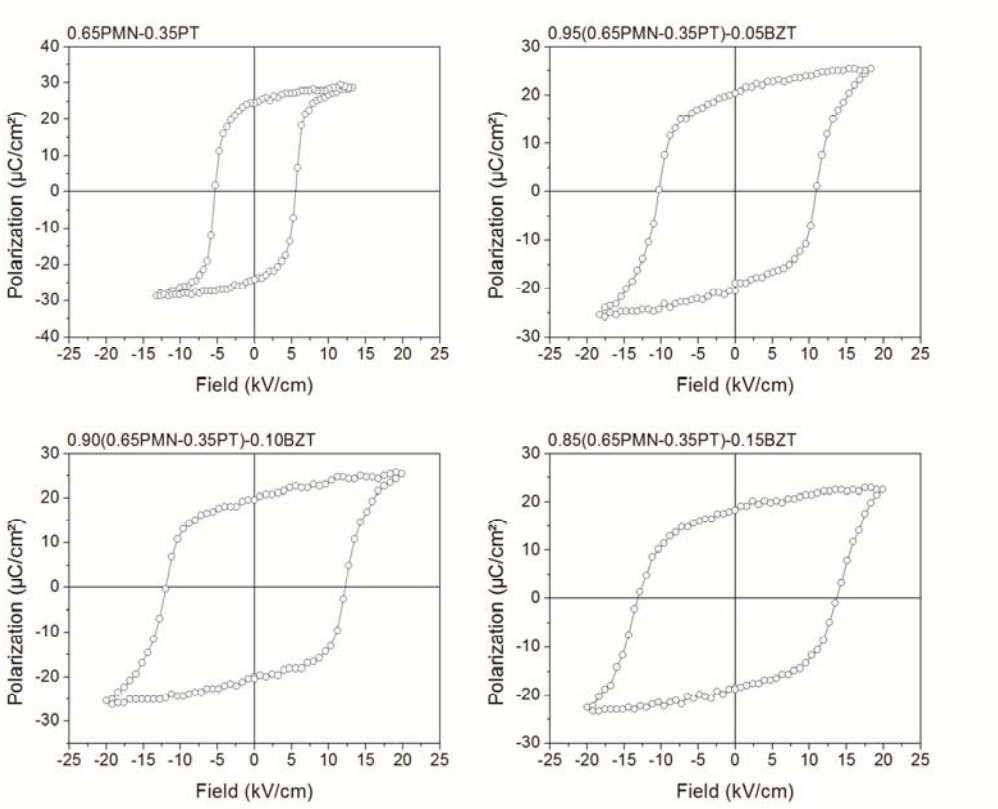

Figure 6.19: Polarization versus electric field measurements for the (1-*p*)(0.65PMN-0.35PT)-*p*BZT ceramics measured at room temperature.

6.8 Ternary Phase Diagram of the *x*PMN-*y*PT-*z*BZT system

6.8.1 Structure

The data presented above on the pseudo-binary systems studied are combined to establish the ternary phase diagrams for the PMN-PT-BZT system in terms of structure phase components, dielectric, piezoelectric and ferroelectric and properties. Along with the data presented the previous sections, data from the line of 0.20PMN-0.64PT-0.16BZT which were investigated by Michael Leung, a an undergraduate reseach student working in our lab and under my supervision, were included in the ternary figures to provide further data to complete the phase diagram. Figure 6.20 shows the structural

phase diagram for the *x*PMN-*y*PT-*z*BZT system. The red lines indicate the solubility limit for the complex perovskite structure, outside which a secondary pyrochlore phase of the $PbNb_2O_7$-type forms. The system contains two major phase components, a rhombohedral and a tetragonal phase, as well which are separated by a ternary morphotropic phase boundary (MPB) region, in which another phase of lower symmetry is found to exist. Figure 6.21 shows the ferroelectric phase transition, which indicates that the T_C increases along the PT-BZT side, with the maximum T_C = 700 °C at the composition of 0.60PT-0.40BZT.

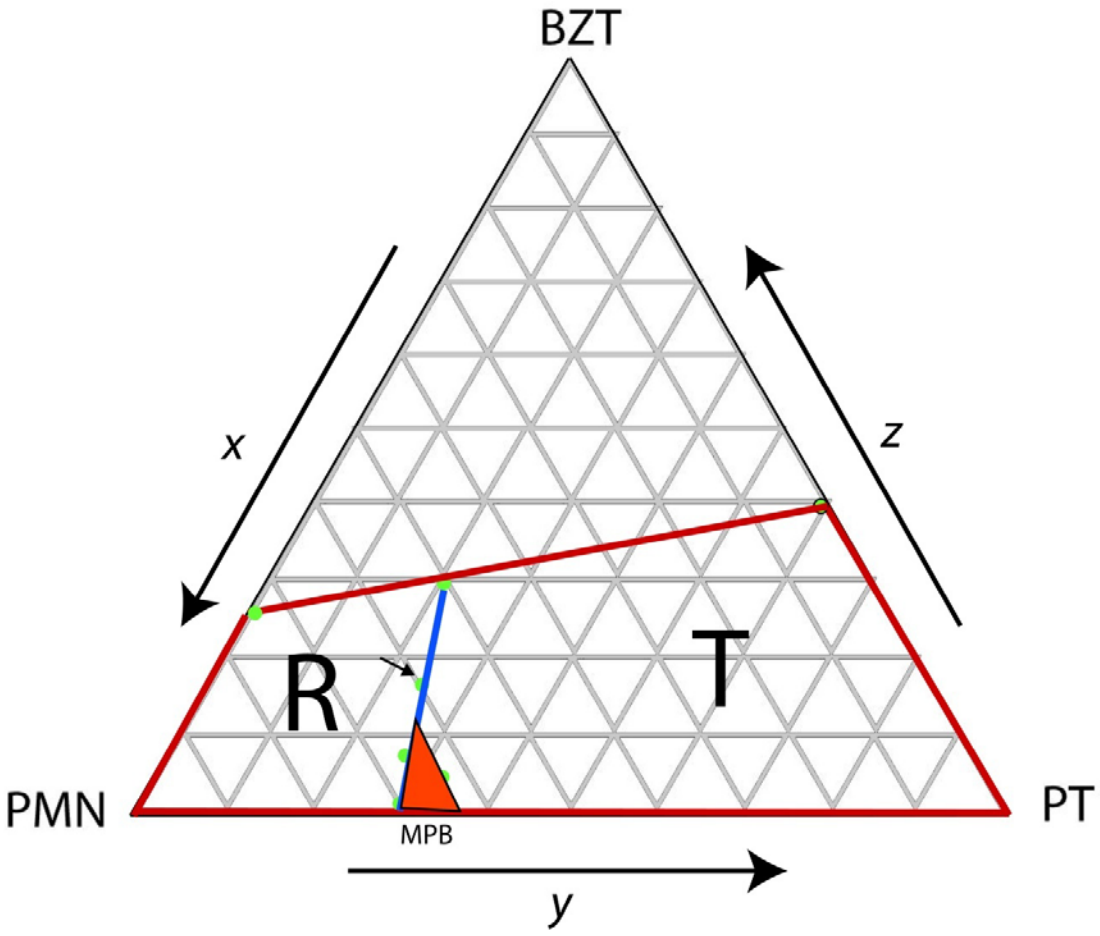

Figure 6.20: Room temperature structural phase diagram of the *x*PMN-*y*PT-*z*BZT ternary solid solution system, which indicates the R and T phases and the MPB. The red lines indicate the limits of solubility for the perovskite phase, the blue line delimits the phases.

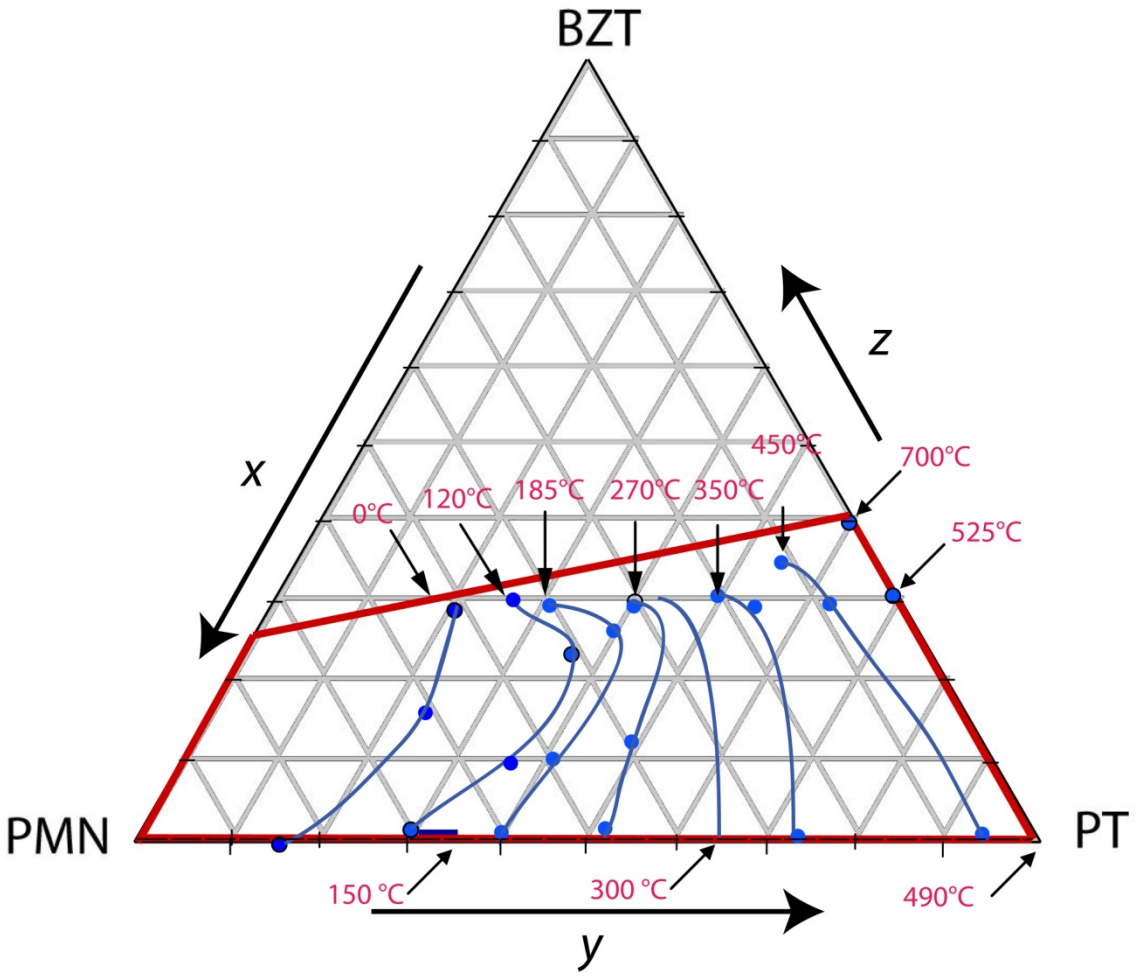

Figure 6.21: Phase diagram showing Curie temperature, T_C, as a function of composition for the *x*PMN-*y*PT-*z*BZT ternary solid solution system. Solid blue lines indicate compositions with the same T_C.

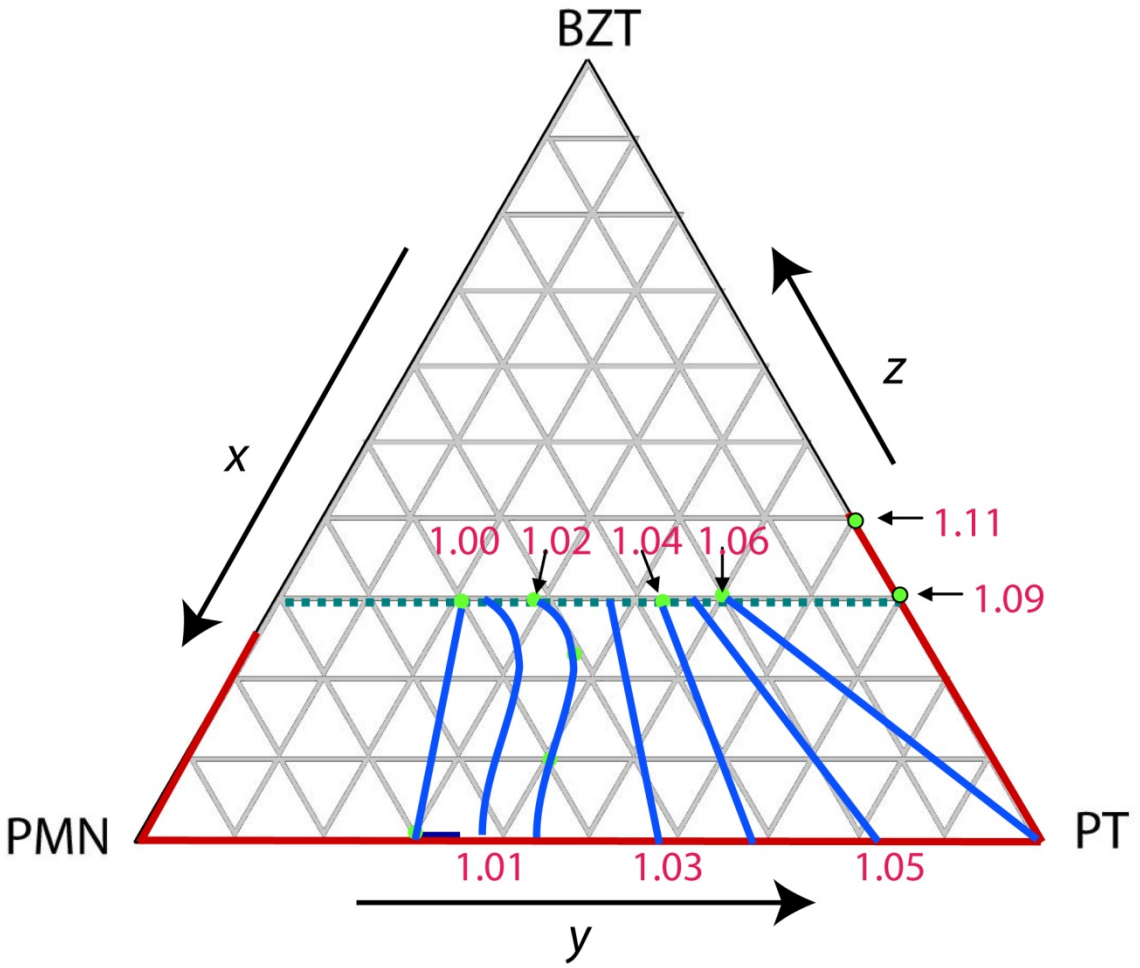

Figure 6.22: Room temperature tetragonality (*c/a*) of the *x*PMN-*y*PT-*z*BZT ternary system; the blue lines indicate equivalent values. The tetragonality increases towards the PT-BZT pseudo binary line, with the highest value of 1.11 at 0.60PT-0.4BZT.

6.8.2 Dielectric Properties:

Figure 6.23 shows the variation in the real part of permittivity measured at room temperature as a function of composition. It can be seen that the highest value is at 0.90PMN-0.10PT and it decreases when moving radially away from that composition. The room temperature permittivity decreases with increasing T_C, which is consistent with the permittivity peak corresponding to the phase transition moving away from room temperature. The room temperature permittivity also decreases with increasing BZT

content, which is the same as the behaviour discussed in Chapter 5. This may be due to the Pb^{2+} being replaced by the Bi^{3+}, which is isoelectronic, but has a larger charge making it is less polarizable.

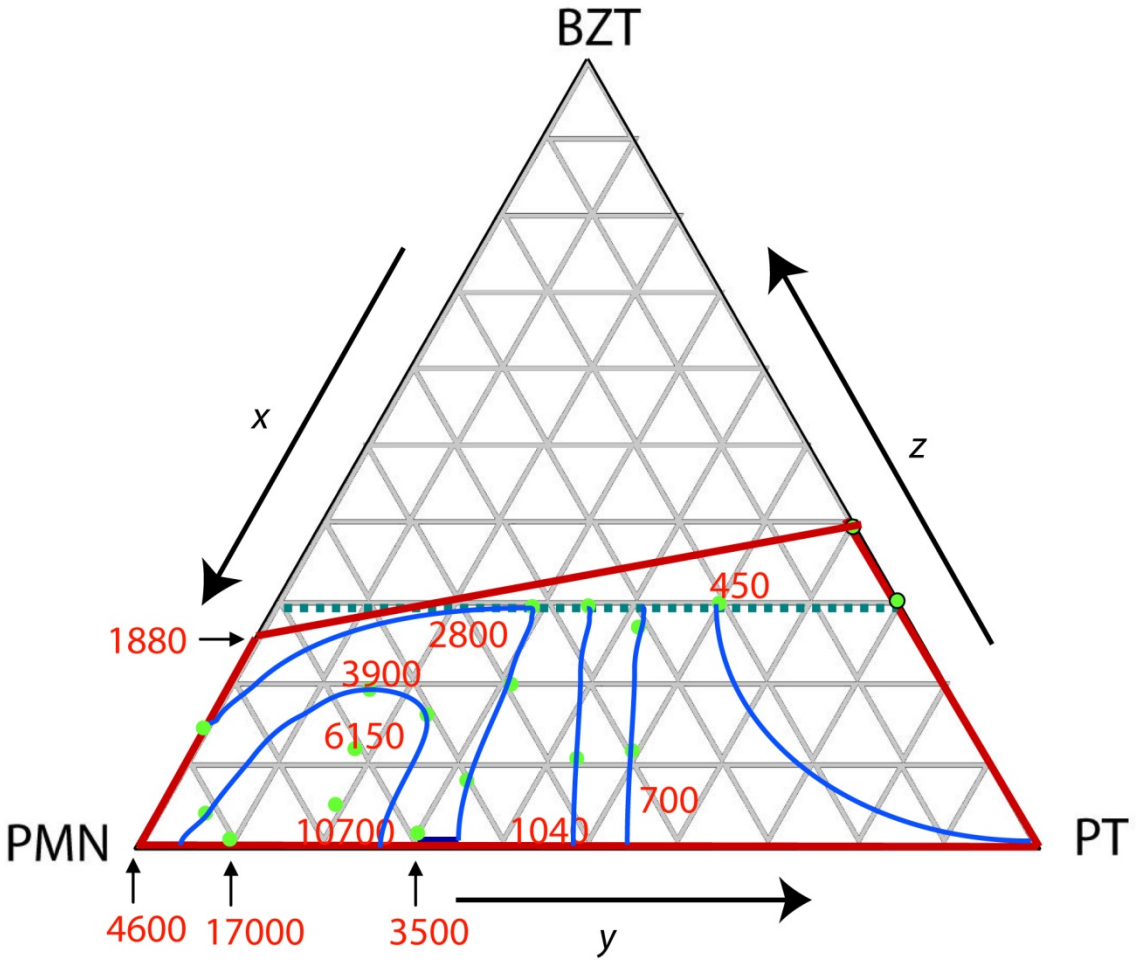

Figure 6.23: Real permittivity measured at 1 kHz and room temperature of the *x*PMN-*y*PT-*z*BZT ternary system. The blue lines indicate isovalue lines of room temperature permittivity.

6.8.3 Ferroelectric and Piezoelectric Characterization

Figure 6.24 presents the room temperature coercive field as a function of composition for the *x*PMN-*y*PT-*z*BZT ternary system. The PMN-BZT side of the ternary system exhibited relaxor behaviour, as discussed in Chapter 5, and did not exhibit

any macroscopic spontaneous polarization. However, with the increase in PT, long range polar order was formed, leading to macroscopic ferroelectricity in the tetragonal phase as discussed in Section 6.5. The spontaneous polarization and coercive fields increase with tetragonality, becoming largest towards the 0.60PT-0.40BZT composition. It was not possible to obtain the coercive fields and ferroelectric properties of all the compositions prepared, as the coercive fields for some compositions are larger than the dielectric breakdown fields for the ceramics. For compositions with T_C > 350 °C, fields as large as 200 kV/cm were applied to the ceramics, but it was still not possible to switch the polarization or to measure any remnant polarization, as no hysteresis loops can be displayed to characterize their ferroelectric properties.

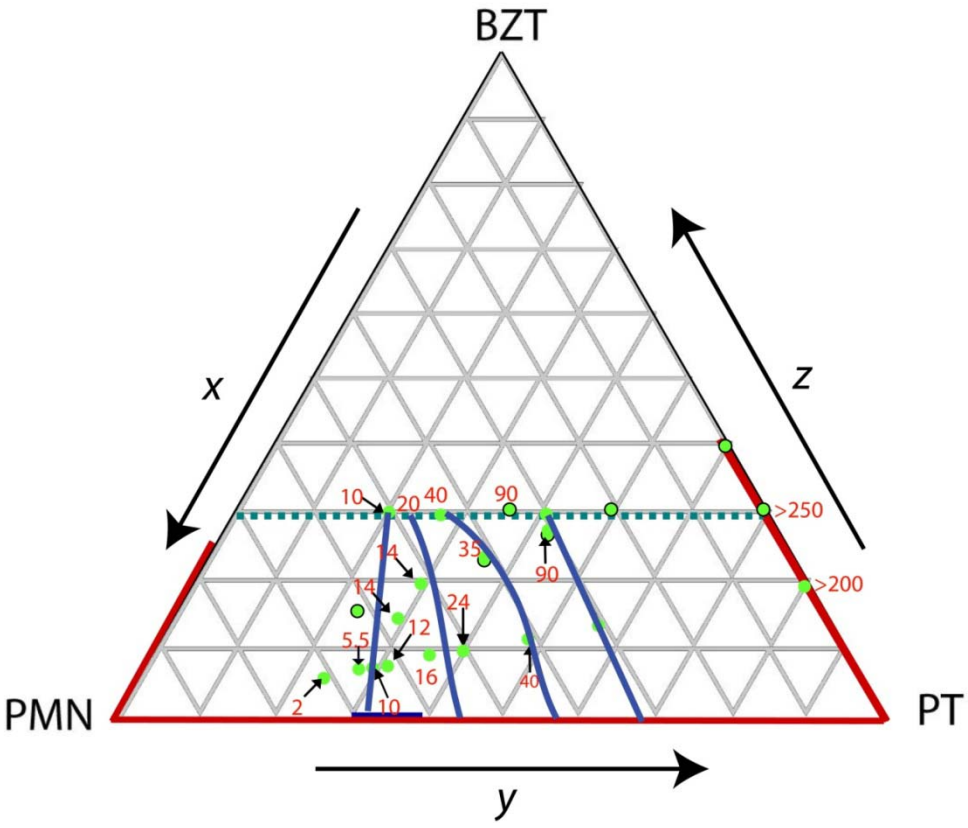

Figure 6.24: Room temperature coercive fields of the *x*PMN-*y*PT-*z*BZT ternary system. The coercive field increases with phase transition temperature and tetragonality.

For the ceramics that could be poled fully, the room temperature piezoelectric charge coefficient as a function of composition within the ternary system is presented in Figure 6.25. The piezoelectric properties in the tetragonal region varies in the same way as the room temperature dielectric constant, so that the piezoelectric constants generally increases with decreasing T_C. Relatively good piezoelectric properties were measured in along the line investigated by Michael Leung, in the range of (1-p)PMN-p(0.80PT-0.20BZT) with p = 0.38- 0.42, with a piezoelectric charge constant of 450 pC/N and a coercive field larger than 10 kV/cm. Furthermore, these compositions are of tetragonal symmetry and are not prone to over poling as in the case of rhombohedral ceramics of the PMN-PT system, which posses a lower coercive field (2-3 kV/cm) and a low T_{MPB}, and are susceptible to being over poled into a field induced monoclinic state, which has poorer piezoelectric response. By using compositions in this vicinity of the ternary system, which posses a high E_C, a comparable d_{33}, and a relatively high T_C with no other isomorphic transitions below T_C, it is possible to overcome the drawbacks of the PMN-PT ceramic system for use in high T_C and high power applications.

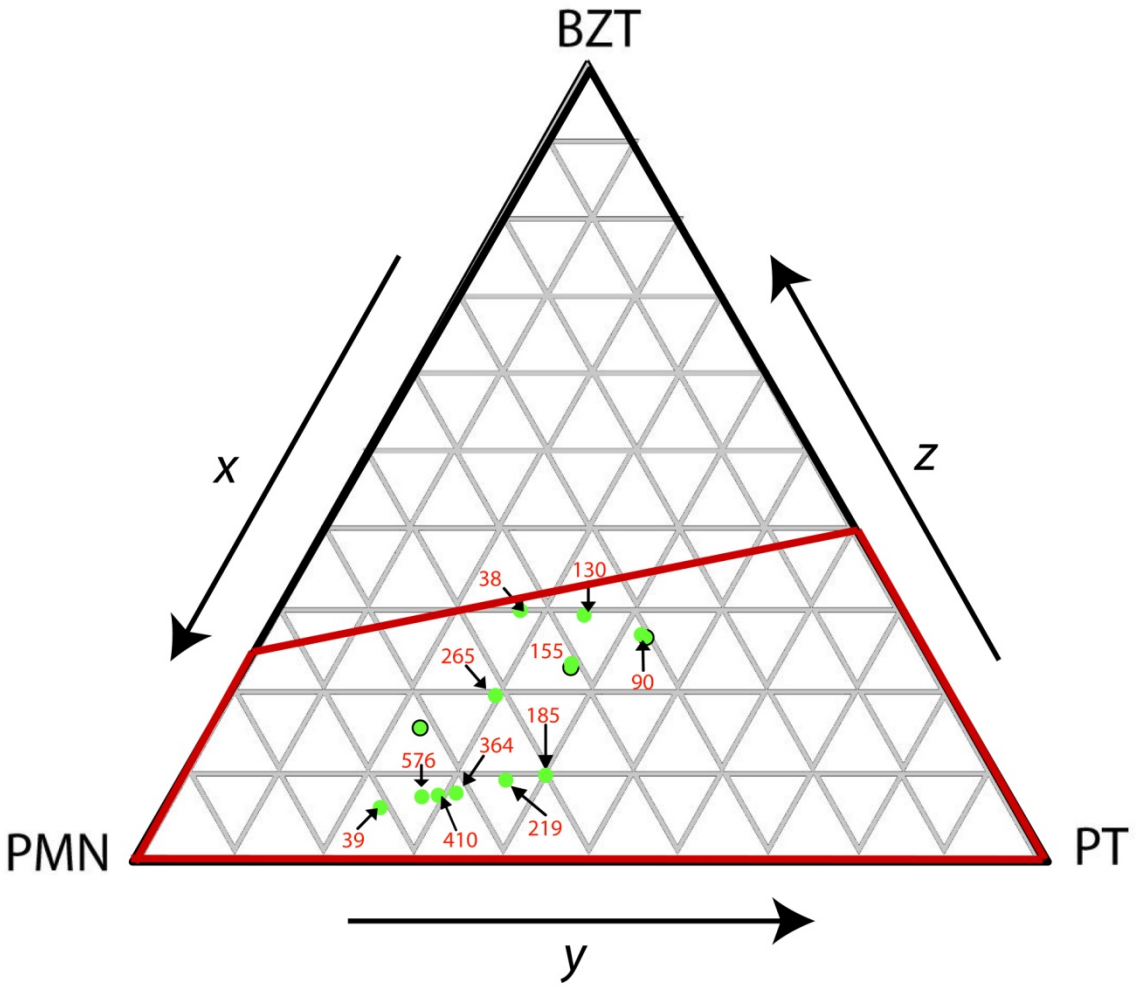

Figure 6.25: Room temperature piezoelectric charge constant d_{33} (pC/N) of the *x*PMN-*y*PT-*z*BZT ternary system. The highest values are found in the vicinity of the PMN-PT binary morphotropic phase boundary. Relatively high values of piezoelectric charge constants are also found in the tetragonal region, which is less susceptible to over poling and possess a reasonably high T_C as to expand the operating temperature range of piezoelectric devices.

6.9 Conclusions

The PMN-PT-BZT ternary system has been prepared by solid state reaction and systematically characterized in terms of structure, phase components, dielectric piezoelectric and ferroelectric properties. It shows many interesting features within the limit of solubility for the perovskite structure. The ternary phase diagram of the structure

and properties have been established along the PMN-BZT side of the phase diagram. The system exhibits high and broad permittivity, which is typical of classical relaxor behaviour. Normal ferroelectric behaviour begins to appear in the compositions toward the PT-BZT side of the ternary system, so that the pseudo-binary lines of (1-*y*)[(1-*m*)PMN-*m*PT]-*y*BZT with constant *y* have their highest phase transition temperatures on the PT-BZT line, with the Curie temperatures of the (1-*x*)PT-*x*BZT line increasing with BZT concentration. The upper limit of chemical thermal stability also decreases with the addition of the BZT end member so that the sintering temperatures required to produce ceramics needed to be decreased in order to produce pure perovskite phase. The coercive field and the tetragonality, *c/a*, increases in the same manner as the phase transition temperature.

It was found that the addition of BZT to the compositions in the vicinity of the PMN-PT binary system of MPB composition decreases the T_{MPB} and T_C. The most promising piezoelectric properties were found near 0.60PMN-0.32PT-0.08BZT, in the tetragonal phase region of the system, which provided comparable piezoelectric performance to the PMN-PT system, but with a larger coercive field. The increased coercive field and tetragonal symmetry make materials of these compositions suitable for high power electromechanical applications because this composition is not easily depoled, nor does it suffer from the possibility of over poling which is known to degrade the piezoelectric performance of the PMN-PT ceramics as discussed in Chapter 3. In addition, the compositions towards the PT-BZT pseudobinary line provide very high phase transition temperatures, which permits a very large temperature operating range. Future work in softening these materials in order to lower the coercive fields for poling should be

undertaken to fully realize the piezoelectric and ferroelectric potential of the high T_C compositions of this system.

References

[1] A. A. Bokov and Z. G. Ye, "Recent progress in relaxor ferroelectrics with perovskite structure," *Journal of Materials Science,* vol. 41, pp. 31-52 (2006).

[2] G. A. Samara and E. L. Venturini. "Ferroelectric to relaxor crossover in compositionally disordered perovskites". *Phase Transit.* vol. 79*,* pp. 21-40 (2006)

[3] X. Zhao, W. Qu, X. Tan, A. A. Bokov and Z-. G. Ye, "Influence of long-range cation order on relaxor properties of doped $Pb(Mg_{1/3}Nb_{2/3})O_3$ ceramics," *Physical Review B,* vol. 79, pp. 144101:1-12 (2009).

[4] Z-. G. Ye and A. A. Bokov, "Dielectric and structural properties of relaxor ferroelectrics," *Ferroelectrics,* vol. 302, pp. 473-477, (2004).

[5] A. A. Bokov and Z-. G. Ye, "Universal relaxor polarization in $Pb(Mg_{1/3}Nb_{2/3})O_3$ and related materials," *Physical Review B,* vol. 66, 064103:1-10 (2002).

[6] Z-. G. Ye, "Relaxor ferroelectric complex perovskites: Structure, properties and phase transitions," *Key. Engineerinng Materials,* vol. 155-1, pp. 81-122 (1998).

[7] Z-. G. Ye., "Relaxor ferroelectric complex perovskites: Structure, properties and phase transitions" *Oxides 155-1* pp. 81-122 (1998).

[8] L. E. Cross., "Relaxor ferroelectrics," *Ferroelectrics* vol. *76(3-4),* pp. 241-267 (1987).

[9] B. Noheda, D. E. Cox, G. Shirane, J. Gao and Z-. G. Ye, "Phase diagram of the ferroelectric relaxor (1-x) $Pb(Mg_{1/3}Nb_{2/3})O_3$-$xPbTiO_3$," *Physical Review B,* vol. 66, pp 054104:1-10 Aug. 2002.

[10] S. E. E. Park and W. Hackenberger, "High performance single crystal piezoelectrics: applications and issues," *Current Opinion in Solid State and Materials Science,* vol. 6, pp. 11-18, (2002).

[11] A. A. Bokov and Z-. G. Ye, "Field-induced shift of morphotropic phase boundary and effect of overpoling in (1-x) $Pb(Mg_{1/3}Nb_{2/3})O_3$-$xPbTiO_3$ piezocrystals," *Applied Physics Letters,* vol. 92, pp 082901:1-3 (2008).

[12] M. Dong and Z-. G. Ye, "High-temperature solution growth and characterization of the piezo-/ferroelectric (1-x) $Pb(Mg_{1/3}Nb_{2/3})O_3$-$xPbTiO_3$ [PMNT] single crystals," *Journal of Crystal Growth,* vol. 209, pp. 81-90, (2000).

[13] S. W. Choi, T. R. Shrout, S. J. Jang and A. S. Bhalla, "Dielectric and Pyroelectric Properties in the (1-x) $Pb(Mg_{1/3}Nb_{2/3})O_3$-$xPbTiO_3$ System," *Ferroelectrics,* vol. 100, pp. 29-38 (1989).

[14] R. E. Eitel, C. A. Randall, T. R. Shrout, P. W. Rehrig, W. Hackenberger and S. E. Park, "New high temperature morphotropic phase boundary piezoelectrics based on $Bi(Me)O_3$-$PbTiO_3$ ceramics," *Japanese Journal of Applied Physics,* vol. 40, pp. 5999-6002 (2001).

[15] C. J. Stringer, T. R. Shrout, C. A. Randall and I. M. Reaney, "Classification of transition temperature behavior in ferroelectric $PbTiO_3$-Bi(Me ' Me ")O_3 solid solutions," *Journal of Applied Physics,* vol. 99, pp 024106:1-4 (2006).

[16] I. Grinberg, M. R. Suchomel, W. Dmowski, S. E. Mason, H. Wu, P. K. Davies and A. M. Rappe.. Structure and polarization in the high T_C ferroelectric $Bi(Zn_{1/2}Ti_{1/2})O_3$-$PbTiO_3$ solid solutions. *Physical Review Letters,* vol. 98, pp. 107601:1-7 (2007).

[17] M. R. Suchomel and P. K. Davies, "Enhanced tetragonality in $(x)PbTiO_3$-$(1-x)Bi(Zn_{1/2}Ti_{1/2})O_3$ and related solid solution systems," *Applied Physics Letters,* vol. 86, pp. 262905:1-7, Jun. 2005.

[18] S. L. Swartz and T. R. Shrout, "Fabrication of Perovskite Lead Magnesium Niobate," *Materials Research Bulletin,* vol. 17, pp. 1245-1250 (1982).

[19] S. E. Park and T. R. Shrout, "Ultrahigh strain and piezoelectric behavior in relaxor based ferroelectric single crystals," *Journal of Applied Physics,* vol. 82, pp. 1804-1811 (1997).

[20] A. A. Bokov and Z-. G. Ye, "Freezing of dipole dynamics in relaxor ferroelectric (1-x) $Pb(Mg_{1/3}Nb_{2/3})O_3$-$xPbTiO_3$ as evidenced by dielectric spectroscopy," *Journal of Physics-Condensed Matter,* vol. 12, pp. L541-L548, (2000).

[21] Z. Ye and H. Schmid, "Optical, Dielectric and Polarization Studies of the Electectric Field Induced Phase Transitions in PMN," *Ferroelectrics,* vol. 145, pp. 83-108 (1993).

[22] B. Noheda, D. E. Cox, G. Shirane, S. E. Park, L. E. Cross and Z. Zhong, "Polarization rotation via a monoclinic phase in the piezoelectric 92% $PbZn_{1/3}Nb_{2/3}O_3$-8% $PbTiO_3$," *Physical Review Letters,* vol. 86, pp. 3891-3894, (2001).

[23] R. E. Cohen."Origin of ferroelectricity in perovskite oxides". *Nature vol 358,* pp. 136-138 (1992).

[24] D. M. Stein, M. R. Suchomel and P. K. Davies, "Enhanced tetragonality in (x)$PbTiO_3$-(1-x)Bi(B ' B ")O_3 systems: $Bi(Zn_{3/4}W_{1/4})O_3$," *Applied Physics Letters,* vol. 89, (2006).

[25] T. Q. Liu, C. S. Lynch and E. A. McLaughlin, "Thermodynamics of stress and electric field induced phase transition in relaxor ferroelectric crystals," *J. Intell. Material Systems and Structures.,* vol. 18, pp. 409-415 (2007).

[26] E. A. McLaughlin, T. Liu and C. S. Lynch, "Relaxor ferroelectric PMN-32%PT crystals under stress, electric field and temperature loading: II-33-mode measurements," *Acta Materialia,* vol. 53, pp. 4001-4008 (2005).

CHAPTER 7:
General Conclusions and Future Directions

7.1 General Conclusions

Development of materials preparation techniques and understanding of the structure and physical properties of the functional materials constitute an important part of materials science, which in turn plays a very important role in modern technology and society. Materials science can be approached in many ways, but two of the most important avenues, which are the focus of this thesis, are in the preparation of existing material systems and the synthesis of new compounds. Novel synthetic techniques allow for optimization of established material systems, which improves the properties of the materials and thereby the performance of the devices fabricated. Synthesis of new material systems (through chemical modification of existing systems or through the formation of new solid solutions) offers another means of addressing the drawbacks of existing materials systems and potentially allows for the discovery of new, interesting and hopefully useful physical properties. It is for these reasons that investment into materials science is worthwhile for both academic curiosity and practical applications.

This thesis work deals with an important class of functional materials, the dielectric, piezoelectric and ferroelectric materials, which have found applications in many electronic applications. Most of the piezo-/ferroelectric materials studied so far are based on the perovskite compounds and their binary solid solutions, for instance, $PbTiO_3$, $Pb(Zr_{1-x}Ti_x)O_3$, and $Pb(Mg_{1/3}Nb_{2/3})O_3$. Very few ternary systems have been investigated. The ternary solid solution between $Pb(Mg_{1/3}Nb_{2/3})O_3$-$PbTiO_3$-$Bi(Zn_{1/2}Ti_{1/2})O_3$ (PMN-PT-BZT) displays a wide range of interesting dielectric properties. The pseudo-binary solid

solution between PMN and PT exhibits a transition from relaxor behaviour on the PMN side to long range ferroelectric order on the PT side, resulting from an increase in polar order from chemical substitution. Accordingly, with the change in composition, the solid solution system undergoes a change from rhombohedral symmetry to tetragonal symmetry at the morphotropic phase boundary where some of the best electromechanical properties are found.

In the first part of this work, a novel solution chemical fabrication technique was developed in order to produce high quality ceramics of the (1-*x*)PMN-*x*PT solid solution system. Investigation was carried out to find the best composition of precursor solution and the optimal sintering conditions to produce high-density and high-quality ceramics in pure phase. The technique allows for one step sintering to produce high quality ceramics with high density (97 % d_{rel}) and to optimize the performance of the PMN-PT system.

The PMN-PT ceramics with compositions near the MPB (x = 0.28 - 0.32) were chosen for study because of their excellent electromechanical properties in the form of single crystals and ceramics. These compositions show the largest electromechanical coupling efficiency (k_P = 0.73) and large strain as a function of electric field (d_{33} = 815 pm/V) in the composition of 0.70PMN-0.30PT ceramics. These values are higher compared to ceramics prepared by conventional solid state technique, which typically have a $d_{33} \sim 700$ pm/V. To fully optimize the ceramic properties, the effect of high temperature poling was investigated, and it was found that poling at high temperature degraded the piezoelectric response of the ceramics. The effect is analogous to that of over-poling at high fields in crystals, which results in a field-induced shift of the morphotropic phase boundary. This produces an induced monoclinic phase with poorer piezoelectric

performance at compositions with lower PT content. This behaviour shows an interesting trend with respect to its compositional dependence on the degradation. It was found that the properties of the (1-*x*)PMN-*x*PT ceramics of compositions that lay on the boundary or inside the MPB (x = 0.30, 0.32) were more susceptible to over poling than the ceramics of x = 0.28 which is in the rhombohedral side of the phase diagram. This is significant, because although the 0.72PMN-0.28 ceramics show the lowest piezoelectric properties, its relative composition away from the MPB makes them less prone to over-poling.

Following the successful preparation of (1-x)PMN-xPT ceramics in the MPB region, the solid solution compounds of (1-x)PMN-xPT with x = 0.07 and 0.10 were prepared and characterized for their dielectric properties as a function of sintering conditions, measurement temperature and frequency. These compositions of x were chosen because they exhibit their frequency dependent maximum of permittivity (at 100 kHz and 1 Hz, respectively) near room temperature. The ceramics made by this method could be produced in pure phase at 950 °C/4 hrs, but a higher sintering temperature of 1100 °C/4 hours was required in order to obtain higher density which is necessary to reduce dielectric losses and increase the dielectric permittivity. The high dielectric constants (~ 22 000) are valuable for use in applications such as frequency filters and high density charge storage capacitors. The relaxor properties were characterized by a quadratic law that describes the high temperature slope of the permittivity. The addition of the polar PT to PMN, was found to decrease the diffuseness of the permittivity peak, which is consistent with the transition to a long-range ferroelectric state with sharp phase transition. Furthermore, the dynamics of the polar nanoregions in the 0.90PMN-0.10 PT ceramics was investigated by fitting the temperature of maximum of permittivity as a

function of frequency to the Vogel-Fulcher law which describes the critical slowing down and freezing of the dipole moments of PNR's at a freezing temperature, T_f. It was found that the freezing temperature was very close to the depolarization temperature, which is the temperature above which no macroscopic polarization can form even upon application of an electric field.

The solid solution between BZT and PMN was investigated for its structure, chemical stability, and dielectric behaviour. The system showed some unique trends the structure and electrical properties. In contrast to the PT-BZT system which exhibits an increase in the tetragonality, c/a, and the Curie temperature, T_C, which reaches as high as 700 °C, with increasing BZT content, the PMN-BZT system shows a very different properties. The solid solution between PMN and BZT does not change the structure significantly and remains cubic up to the solubility limit of 0.625PMN-0.275BZT. The PMN-BZT solid solution exhibits an increase in frequency and temperature dispersion along with an increase in diffuseness of the permittivity peak with increasing BZT content. From fitting the dielectric properties as a function of composition and temperature, it was found that the PMN-BZT solid solution showed the same number and types of polarization contributions to its permittivity as PMN-PT. However, the new binary system showed different behaviour in that the depolarization temperature, T_d for the PMN-BZT system was lower than that of pure PMN itself, whereas in the (1-*x*)PMN-*x*PT, the T_d increases with increasing PT content. This makes the compound BZT unique in that by forming a solid solution with one end member (PT), it can increase the ferroelectric ordering in one compound but can also decrease the degree of polar order in another (PMN).

The ternary solid solution between all three end members was investigated in order to explore its structure, crystal chemistry, ferroelectric and piezoelectric properties as a function of composition in order to fully link the structures and properties of the three different pseudo-binary systems discussed above. As can be expected, the behaviour of the ternary system shows a very wide range of behaviour in terms of structure and properties, depending on the different constituent end members and their binary solid solutions. The ternary system exhibits a very large tetragonality on the PT-BZT side of the phase diagram and correspondingly high phase transition temperatures reaches 700 °C at the composition of 0.60PT-0.40BZT. The system exhibits an increase in tetragonality and coercive field towards the composition of 0.60PT-0.40BZT. The coercive fields increase to the limit where they become larger than the dielectric breakdown field of the ceramics and cannot be measured easily.

The addition of BZT to the PMN-PT compositions near the MPB was performed in order to find the limits of the ternary morphotropic phase region and investigate the structure and ferroelectric properties. For compositions with very large BZT content, it was found that the morphotropic phase transition occurs at a temperature below room temperature, as described in Section 6.3. The addition of BZT results in a decrease in phase transition temperature and increases the coercive field. This is different from the trend seen in the PMN-PT system, where the coercive fields generally increase with phase transition temperature.

Although the best electromechanical properties in terms of the piezoelectric charge constant, d_{33}, were found in the PMN-PT system, this work shows that the performance of existing systems can still be enhanced through proper fabrication techniques, such as

the solution chemical techniques discussed in Chapters 3 and 4. Furthermore, the ternary system provides some advantages to overcome the inherent drawbacks of the binary PMN-PT system, such as such as the high lead content, low transition temperatures and low coercive fields, which cannot be addresses by fabrication methods. By choosing the appropriate ratio of the three end members in the system, it becomes possible to choose compositions that balance the phase transition temperatures and the coercive fields for particular applications. A useful case would be in applications that require high acoustic power at high temperature. Low coercive fields at room temperature become problematic because the coercive field decreases as the material is heated towards the Curie temperature. The tetragonal symmetry, high transition temperatures and large coercive fields prevent over-poling and allow for the application of large fields at high temperatures without the risk of depoling the ferroelectric elements. These feature would be very useful in such applications as fuel injection systems and detection and cancellation of vibration in machinery.

7.2 Future Directions:

The PMN-BZT system raises many questions about the difference in its behaviour compared to the PT-BZT system. More focus should be put into understanding the difference in the chemical ordering and crystal structure in order to shed light on what differences the addition of BZT to PMN has on the dielectric behaviour of this system compared to its addition to PT. Compositions along the whole solubility limit should be investigated for its dielectric behaviour, as described in the end of Section 5.5, to fully understand the compositional dependence of the dielectric parameters that describe the relaxor behaviour in the PMN-BZT system. Furthermore, the results of this analysis can

be compared to the measurement protocol of zero-field-cooling after poling to see if the depolarization temperatures coincide with the freezing temperatures found from fitting the dielectric properties as a function of frequency and temperature to the quadratic function and Vogel-Fulcher law described in Chapters 4 and 5. A more thorough investigation of this binary system would provide a better understanding of the trends seen in the ternary system.

The ternary solid solution system between PMN-PT-BZT has helped address some of the drawbacks of PMN-PT solid solution system, however, the extremely large coercive fields on the PT-BZT end of the system present an issue in its own right. The inability to pole these materials at room temperature becomes problematic in that their piezoelectric and ferroelectric potential cannot be fully explored. Future efforts must be made in addressing the high coercive field, either by poling at high temperature, or by chemical modification to "soften" or reduce the coercive field of these materials. Previous work in PZT ceramics has shown that the heterovalent substitutions of higher valence cations, such as La^{3+} for Pb^{2+} or Nb^{5+} for Ti^{4+}, which serve as "donor" cations, can decrease the coercive field in PZT and related materials. The same approach is expected to be effective in lowering the coercive field of the PMN-PT-BZT ceramics.

Finally, single crystal growth of the PMN-PT-BZT system is worth investigating for several reasons. The low melting PbO and Bi_2O_3 constituents of the solid solution could be used as flux in a high temperature solution growth of the crystals at lower temperatures than from pure melt. Furthermore, because the flux would consist of ions that are already in the structure of the solid solution, the possibility of undesired inclusions would be greatly reduced. Single crystal growth of compositions along the

PMN-BZT line would help better understand the structure and dielectric behaviour of the system. Furthermore, although ceramics are easy to prepare in short time and high yield, the best piezoelectric and ferroelectric properties are found in the form of single crystals in PMN-PT and other perovskite solid solutions. Therefore, single crystal growth of the compositions approaching the PT-BZT side of the phase diagram would be valuable for investigating the structure and crystallographic dependences of the piezoelectric and ferroelectric properties. These crystals would be useful for high field and high temperature applications. The availability of single crystals will allow us to use polarized light microscopy to study domain structure and birefringence and their temperature and electric field dependences, which would provide a better understanding of the phase transitions and structure – property relation of the this complex system.